Microphysical Control of Marine Stratocumulus Radiative Properties

by Robert Pincus

A dissertation submitted in partial fulfillment
of the requirements for the degree of

Doctor of Philosophy

University of Washington

1994

Chair of the Supervisory Committee:
Marcia Baker

First Printing 1994

96 95 94 3 2 1

Copies of this dissertation are available from the author, in care of

Geophysics Program AK-50
University of Washington
Seattle WA 91895

Printed in the United States of America.
Set in Perpetua and Gill Sans.

University of Washington

Abstract

Microphysical Control of Marine Stratocumulus Radiative Properties

by

ROBERT PINCUS

Chair of the Supervisory Committee: Marcia Baker
Professor, Geophysics Program

Marine stratocumulus clouds cover large regions of the earth's subtropical oceans and strongly modify the top-of-the-atmosphere radiation budget. Models of the cloud-topped marine boundary layer have suggested that the number concentration of cloud droplets may play an important role in modifying both cloud fraction (through the role of precipitation) and cloud albedo, but these predictions have been difficult to test observationally because of the Lagrangian nature of cloud evolution.

A technique is developed for the Lagrangian observation of cloud evolution from space. The technique combines information from operational weather analyses and visible and infrared imagery from geostationary satellites. Temporally and spatially varying winds from the synoptic analyses are used to compute the trajectories of boundary layer air parcels as they are advected from their initial positions. Mesoscale sized regions centered on the parcel position are periodically extracted from the satellite images, from which cloud characteristics are then derived. This process provides a time history of both cloud properties and environmental conditions along the parcel trajectory.

The technique is used to asses the importance of precipitation in determining the evolution of cloud fraction in the marine boundary layer off the coast of California. Three main conclusions are reached: (a) the presence or absence of precipitation appears to be unimportant in controlling cloud fraction, (b) the diurnal cycle of solar insolation is the most important determinant of cloud fraction, but that (c) parcels travelling over rapidly warming ocean surfaces may maintain high cloud fraction in the face of solar insolation. Detailed numerical simulations of cloud evolution with a sophisticated cloud model confirm these conclusions.

A simple equilibrium mixed-layer model is used to link cloud albedo and droplet number concentration through the process of precipitation. The model predicts that the albedo susceptibility (the differential sensitivity of cloud albedo to droplet number concentrations) of stratiform clouds is underpredicted by 50–200% if the effects of precipitation on cloud thickness are ignored.

Contents

Figures

Introduction

The Lagrangian Observational Technique

Observations of Stratocumulus Evolution

Simulations of Stratocumulus Evolution

A Simple Model Linking Cloud Albedo and Droplet Number Concentration

Tables

Acknowledgments

I owe uncountable debts of gratitude to an enormous number of people who have helped me during the six years leading to this dissertation. It has been an honor and a pleasure to be associated with Professor Marcia Baker, who has worked tirelessly, patiently, and with great creativity to inspire me. Each member of my Supervisory Committee (Philip Austin, Chris Bretherton, Conway Leovy, Steve Warren, and Larry Sorensen) has provided valuable insight and feedback at numerous points along the way. I have benefited tremendously from wide-ranging discussions and intellectual ping-pong with Stephen Klein. Matt Wyant performed the simulations described in Chapter 4 and generously helped me understand the mechanics and meaning of detailed numerical models. Jennifer Eden and Raif Majeed performed onerous data processing tasks on my behalf.

I am grateful for financial support of this work from the Office of Naval Research through grant number N00014-90-J-1136 and from NASA through Graduate Fellowship in Global Change Research NGT-30047. Computational facilities were generously provided by Dennis Hartmann under NASA Grant NAGW-2633. Scott Katz wrote and supported the invaluable Satview program for the analysis of satellite images. Marc Michelsen managed the best-run computing environment I could imagine and helped time and again with the nit-picky details.

I obtained data sets from the Data Support Section of the National Center for Atmospheric Research (operational weather analyses), the National Climate Data System at NASA Goddard Space Flight Center (satellite imagery) and the National Ocean Data System at the Jet Propulsion Laboratory (sea surface temperatures).

Both of my families cheered me on and pushed me forward at difficult junctures. The care and feeding of my soul I entrusted to an extraordinary group of friends, including Paul Green, Adam Frank, Margaret Rozendaal, and Paquita Zuidema. Their love and support illuminate my life and work. Finally, and most importantly, I am eternally grateful to my wife Cristina Herdman, who has kept the faith, sustained me, and inspired me at every stage for as long as I have known her.

Dedication

For

Frank Oppenheimer,

who started the ball rolling,

and

Cristina Kenney Herdman,

who knew it would be fun.

1 Introduction

The photographs of the Earth taken during the trips to the Moon in the late 1960s and early 1970s remain some of the most emotionally powerful images of the twentieth century. The vivid realization brought home by those pictures was the profound isolation of our fragile home in the midst of a vast void. When we look back from space, it also becomes clear that our planet is misnamed, since what is visible from afar is not earth but water—oceans and clouds.

Though many people are fascinated by clouds for purely emotional or aesthetic reasons, an understanding of clouds is also an essential precursor to an understanding of the Earth's atmosphere and hydrologic cycle, since clouds play an enormous role in the horizontal and vertical transport of both energy and moisture. As attention has recently focussed on understanding the processes determining terrestrial climate, it has become clear that our limited understanding of clouds, and our lack of ability to accurately represent them in climate models, is the single biggest stumbling block in climate predictions (Cess et al., 1989, 1990).

Climate is, to a large degree, determined by the radiation budget at the top of the atmosphere, which clouds affect in two ways. Because clouds are almost always brighter than the surface underlying them, their presence increases the amount of sunlight reflected back to space, cooling the earth-atmosphere system. On the other hand, clouds intercept and absorb the longwave (infrared) radiation emitted by the surface, re-radiating some fraction of it at a colder temperature. The net effect on the radiation budget depends on the balance of these two factors. Bright low clouds such as stratus and stratocumulus tend to cool the planet; thin high clouds such as cirrus tend to heat it.

1.1 *Why Study Marine Stratocumulus Clouds?*

Figure 1-1 shows the impact of clouds on the top-of-the-atmosphere radiation budget (the "cloud forcing") as determined from two years of data collected by the Earth Radiation Budget Experiment (ERBE, see Barkstrom, 1984). A major result of this experiment was the finding that clouds act to cool the Earth-atmosphere system in the global average by about 20 W m^{-2} (Hartmann, 1993). Regions in which clouds act in aggregate to cool the earth

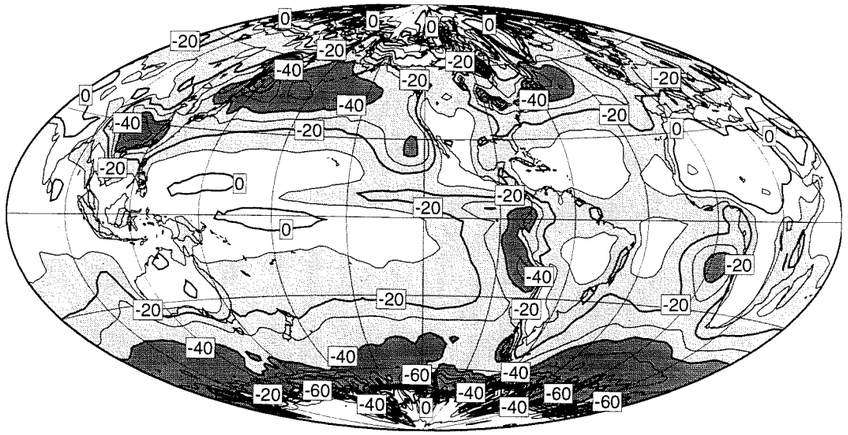

FIG 1-1. Net top-of-the-atmosphere cloud radiative forcing, 1987-1988. Cloud forcing is measured in W m^{-2}. Negative forcing signifies that clouds cool the earth-atmosphere system. The data come from the ERBE project Barkstrom (1984); the figure from Klein and Hartmann (1993).

appear in Figure 1-1 as regions of negative cloud forcing. The cooling occurs primarily over the mid- to high-latitude oceans and over the eastern portions of the subtropical ocean basins, off the coasts of California, Chile, and Namibia.

One might expect that low clouds, because of their high albedo and high radiating temperature, would be prevalent in the regions in Figure 1-1 where cloud forcing is negative. This is indeed the case. Figure 1-2 shows the global distribution of low cloud amount as determined from surface observations (Warren et al., 1986, 1988). The distributions obtained using satellite observations from the International Satellite Cloud Climatology Project (ISCCP, see Rossow and Schiffer, 1991) agree well with the surface observations (Rozendaal et al., 1994).

The subtropical oceanic regions in which large amounts of cloud-induced cooling are evident contain marine stratocumulus clouds. These extensive cloud decks form at the top of the atmospheric boundary layer over the relatively cool water at the eastern edges of the

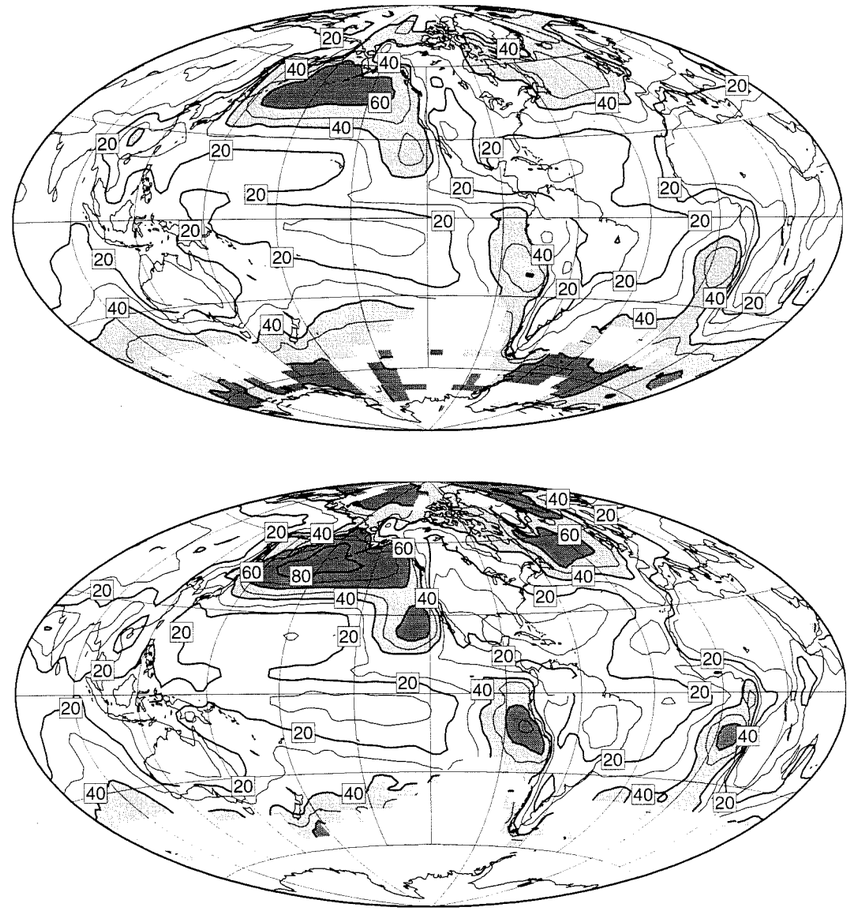

FIG 1-2. Low cloud amount (percent) determined from surface observations. The upper panel shows annually averaged results; the lower results from June, July, and August. Low clouds include cumulus, stratocumulus, and sky-obscuring fog. The regions of subtropical stratocumulus can be seen off the coasts of California, Chile, and Namibia, as well as in the eastern Atlantic. Similar distributions are obtained from analysis of satellite observations. Ships do not visit the Southern Ocean frequently, so observations are missing there. From Klein and Hartmann (1993).

subtropical high pressure region occupying the ocean basins. The boundary layer in these regions is capped beneath a strong inversion which is maintained in part by large scale subsidence caused by a stable high pressure system.

The major processes determining stratocumulus cloud properties are shown schematically in Figure 1-3. Since liquid water is opaque to infrared radiation in very small amounts, the top of the cloud layer experiences strong *longwave radiative cooling*, which causes cloud top parcels to cool and sink through the boundary layer. The sinking parcels generate turbulence, which causes the boundary layer to *entrain* some of the warm, dry air overlying it. Countering the upward motion of the cloud top due to entrainment is the large scale *subsidence*, which is also responsible for the divergence of the horizontal wind fields. The water lost though entrainment and energy lost through cloud-top cooling may be partially replaced by *surface fluxes* of heat and moisture. The entire system undergoes a diurnal cycle driven by the *solar radiation*. If the cloud becomes thick enough or the cloud droplets large enough the cloud may produce *drizzle*. In deeper boundary layers, underlying *cumulus clouds* may form, affecting the layer dynamics.

1.2 *Microphysics, Macrophysics, and Radiation*

One of the astonishing things about clouds is the vast range of spatial and temporal scales over which physical phenomena interact. Cloud microphysical processes (those determining the nucleation or formation of individual drops and their subsequent growth) operate over four or five orders of magnitude, from the size of cloud condensation nuclei (fractions of a micrometer) to scales representative of precipitation particles (millimeters). These processes, in turn, interact with macrophysical (bulk) cloud thermodynamic properties on scales of meters to hundreds of kilometers by modulating the distribution of liquid water and the atmospheric dynamics which give rise to the cloud. Macro- and microphysical processes at all scales are also linked to the longwave and shortwave radiative environment. As a result, changes in any realm—bulk cloud properties, cloud microphysical processes, or cloud radiative environment—necessarily influence the others.

Both longwave and shortwave radiation play central roles in determining marine stratocumulus properties on a wide range of scales. The most important radiative effect is the long-

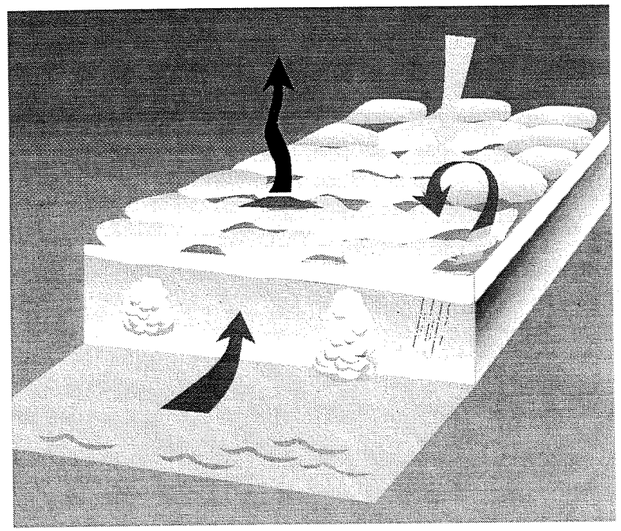

FIG 1-3. Major physical processes determining stratocumulus cloud properties. Arrows indicate the processes of cloud top radiative cooling, turbulent entrainment, absorption of solar radiation and surface fluxes of heat and moisture described in the text. Cumulus clouds and drizzle underneath the stratocumulus are also shown.

wave cooling at cloud top, which is primarily responsible for driving the turbulent convection which sustains the cloud layers. The amount of longwave cooling helps determine both the entrainment rate and the strength of the inversion (Siems et al., 1993), as well as directly modifying the cloud microphysical properties by affecting the supersaturation to which growing and colliding cloud droplets are exposed (Roach, 1976; Austin et al., 1994a). Absorption of solar radiation during the day is responsible for the diurnal cycle in cloud amount (Minnis et al., 1992; Rozendaal et al., 1994) and cloud thickness (Betts, 1990; Hignett, 1991) as the induced heating acts to reduce turbulence levels by partially offsetting the longwave cooling. Since absorption of solar radiation occurs lower in the cloud than does longwave cooling, shortwave heating may also tend to decouple the cloud from its surface moisture supply while promoting entrainment (Rogers and Koracin, 1992).

Cloud microphysical processes, including precipitation, are thought to influence the radiative properties of marine stratocumulus clouds in two ways: by affecting the cloud albedo directly by moderating cloud optical depth, and by affecting the cloud fraction, which in turn affects albedo. The effects are about equally important in their impact on the shortwave radiation budget. Consider the relative impacts of a 10% change in each quantity on the albedo of a typical stratocumulus cloud with optical depth 13 and albedo of 0.5 overlying a non-reflecting surface. If cloud fraction is reduced by 10% the average albedo becomes 0.45, while if optical depth is reduced by 10% with no change in cloud fraction the cloud albedo becomes 0.47. Changes in either cloud fraction or cloud optical depth, therefore, can significantly moderate the cloud radiative forcing.

In this dissertation I assess the degree to which microphysical processes in marine stratocumulus help to determine both cloud albedo and cloud fraction. I focus on the shortwave radiative properties because marine stratocumulus emit longwave radiation at almost the same rate as the ocean beneath them, and hence have small impact on the longwave budget. I describe the specific mechanisms through which cloud microphysics is thought to affect cloud albedo and cloud fraction, then develop an observational tool to test these hypotheses. I complement the observational study with a simple analytic model linking cloud microphysical and macrophysical properties and examine the results of detailed numerical simulations the evolution of precipitating stratocumulus.

1.2.1 LINKING CLOUD OPTICAL AND THERMODYNAMIC PROPERTIES

Cloud albedo increases with cloud optical depth, which is a dimensionless path coordinate describing the average number of extinction (scattering or absorption) events experienced by photons traversing a given distance of material. In a cloud layer, optical depth is formally related to cloud microphysical properties at a single wavelength λ by (Stephens, 1978):

$$\tau_\lambda = \int_0^h \int_0^\infty n(r) Q_{ext}\left(\frac{2\pi r}{\lambda}\right) \pi r^2 dr dz \qquad (1\text{-}1)$$

where $n(r)$ ($m^{-3}\ \mu m^{-1}$) represents the droplet size distribution in a cloud of thickness h (m), and the droplet radius r (μm) is understood to be a function of height z (m). The dimensionless extinction efficiency $Q_{ext}(2\pi r/\lambda)$, which describes the effectiveness with which collisions remove photons from the incident radiation, can be computed from Mie theory (van de Hulst, 1957). For solar radiation impinging on droplets of the size typically found in stratocumulus $2\pi r/\lambda \gg 1$, in which case Q_{ext} approaches 2. Optical depth may therefore be simply represented in terms of two radiatively important parameters. The effective radius r_{eff} is defined as the average surface area weighted radius of the droplet distribution (Hansen and Travis, 1974):

$$r_{eff} = \frac{\int_0^\infty n(r)\, r^3 dr}{\int_0^\infty n(r)\, r^2 dr} \qquad (1\text{-}2)$$

while the liquid water path LWP represents the vertically integrated liquid water content (q_l, kg-water m^{-3}) of the cloud layer:

$$\begin{aligned} LWP &= \int_0^z q_l dz \\ &= \int_0^z \int_0^\infty \frac{4\pi}{3} r^3 n(r) \rho_l dr dz \end{aligned} \qquad (1\text{-}3)$$

Substitution of (1-2) and (1-3) into (1-1) using the asymptotic value of Q_{ext} shows that optical depth may be approximated as

$$\tau_\lambda \approx \frac{3}{2} \frac{LWP}{r_{eff}} \frac{1}{\rho_l} \qquad (1\text{-}4)$$

where ρ_l (kg-water m^{-3}) is the density of liquid water. Optical depth includes both scattering and absorption, and the relative proportion of scattered to absorbed photons, though always quite high in liquid water clouds, is a function of r_{eff}. It is (1-4) which links the thermodynamic, microphysical, and optical properties of clouds.

1.2.2 MICROPHYSICAL CONTROL OF CLOUD OPTICAL PROPERTIES

Nearly two decades ago, Sean Twomey proposed a link between cloud microphysical properties and cloud albedo (Twomey, 1977a, 1977b). He imagined a cloud containing a fixed

amount of liquid water and a specified number of droplets per unit volume, and considered the effects of changes in droplet number concentration. As Twomey showed, increases in droplet number concentration with liquid water content fixed cause the average radius of the cloud droplets to decrease and the total surface area of the droplets to increase, which has the effect of increasing cloud optical depth and hence cloud albedo.

The differential change of albedo with droplet number concentration holding cloud liquid water fixed is termed the albedo *susceptibility* (Twomey, 1991):

$$S_0 \equiv \left.\frac{\partial A}{\partial N}\right|_{q_l} \tag{1-5}$$

Susceptibility as defined in (1-5) reaches a maximum value of 0.01 per cloud drop per cubic centimeter when albedo is 0.5. The number concentration of cloud droplets is proportional to the number of cloud condensation nuclei (Twomey and Warner, 1967), and an increase of 1 CCN cm^{-3} in the lowest kilometer of the global atmosphere requires only 50 tons of material, or a modest injection rate of 1-10 kilotons per year, assuming a CCN residence time of 2 days (Twomey, 1991). Charlson et al. (1987), in proposing a role for marine phytoplankton in controlling cloud albedo, computed the effects of finite changes in droplet concentration on cloud albedo. Their results, shown in Figure 1-4, indicate that significant changes in albedo may be realized by moderate change in droplet concentration, since a change of an order of magnitude in droplet number concentration can induce relative changes in cloud albedo as large as 30%.

Measurements made from satellites (Platnick and Twomey, 1994) and aircraft (Taylor and McHaffie, 1994) in various parts of the world show that marine stratocumulus clouds have a wide range of natural susceptibility, and that clouds in regions of lower CCN (and hence droplet) concentration have albedos which are more sensitive to change than "polluted" clouds with high natural levels of CCN concentration. Since anthropogenic CCN are emitted by many of the same combustion processes as CO_2, Charlson et al. (1992) suggested that the radiative effects of aerosols (including changes in cloud albedo caused by variations in CCN concentration) might mask the warming expect due to increased in CO_2 concentrations in some region of the globe. Furthermore, observations over the Atlantic indicate that

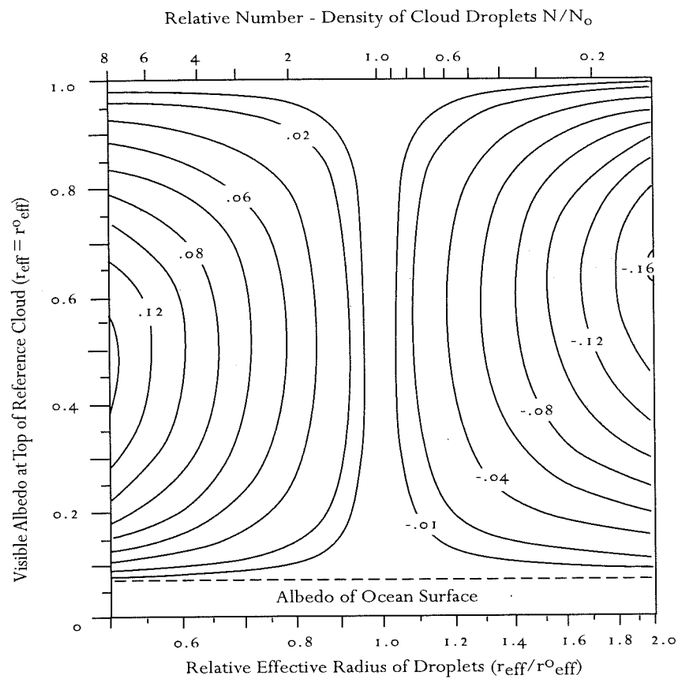

FIG 1-4. Change in cloud albedo due to changes in droplet number concentration. This computation is made assuming that cloud liquid water path remains fixed as number concentration changes. The range of variation in number concentration is well within the bounds of observations, and the relative effect on albedo can be substantial. From Charlson et al. (1987)

anthropogenic CCN may modify cloud albedo at great distance from their source (Taylor and McHaffie, 1994).

The definition of cloud susceptibility in (1-5) assumes that cloud liquid water remain fixed as number concentration varies. Though this may be a reasonable approximation for small changes in droplet concentration, larger variations in droplet concentration such as those shown in Figure 1-4 are likely to be accompanied by changes in boundary layer energetics

and hence bulk cloud properties. One possible linkage was investigated by Boers and Mitchell (1994), who examined the connection between changes in droplet size and solar absorption in marine boundary layer clouds. They noted that an increase in droplet concentration (or a decrease in droplet size) acts to increase cloud optical depth (as (1-4) shows) and hence solar absorption, but that this effect is opposed by the decrease in solar absorption with decreasing droplet size. Both analytic and numerical calculations indicated that, for thin clouds, the latter effect dominates, while the first effect is more important in thick clouds. Since increases in solar absorption should decrease cloud liquid water by affecting the thoroughness of vertical mixing in the boundary layer, Boers and Mitchell suggested that changes in droplet concentration should act to stabilize cloud thickness at either extreme.

1.2.3 MICROPHYSICAL CONTROL OF CLOUD FRACTION

Although changes in cloud fraction and cloud optical depth can affect the radiation budget in similar ways, the changes may be driven by fundamentally different physical processes. Cloud optical depth may change due to changes in cloud thickness or droplet number concentration, but changes in cloud fraction are possible only if dynamics causes a departure of the boundary layer from a well-mixed state. Cloud microphysical processes are thought to act on cloud fraction through the production of precipitation in the form of drizzle.

Drizzle is produced in marine stratocumulus through a complex interplay between boundary layer dynamics and cloud microphysical processes. Precipitation sized droplets are initially formed through collisions between similarly sized droplets, a process known as autoconversion. This process is relatively slow, since similarly sized drops fall at nearly the same speed and because the collection efficiency for droplet sizes typically found in stratocumulus are modest. It takes roughly 45 minutes for a cloud droplet to grow to a drizzle sized droplet (Austin et al., 1994b), which is long compared to the typical residence time of a cloud droplet. The drizzle drops produced, then, are those "lucky few" drops which have remained in the cloud through turbulent mixing.

Precipitation may affect cloud fraction in two ways: by directly removing water from the boundary layer as drizzle at the surface, and by moistening and cooling the layer below the cloud as falling precipitation evaporates. The second effect can inhibit the transport of warm, moist parcels from the ocean surface to the cloud, and may lead to a situation known

as *decoupling* (Nicholls, 1984) in which mixing between the subcloud and cloud layers is suppressed or nonexistent. The evaporation of precipitation in the subcloud layer may also lead to conditional instability and to the presence of cumulus clouds (Nicholls, 1984) which have larger updraft velocities than are typical in stratocumulus. Cumulus clouds arising beneath stratocumulus may penetrate into the overlying stratocumulus deck, enhancing entrainment and leading to a rapid reduction in cloud fraction.

Albrecht (1989) proposed a quantitative link between drizzle and cloud fraction. In his model of the trade-wind boundary layer, drizzle acts through the direct removal of cloud water, which causes the cloud layer to dry (Albrecht, 1993) and the diagnosed cloud fraction to decrease. Albrecht's model predicts a strong dependence of cloud fraction on the efficiency of precipitation, which may be construed as inversely proportional to the number of cloud droplets. Wang et al. (1993) applied a modified version of Albrecht's model to regional simulations of subtropical stratocumulus clouds off the coast of California and found that eliminating drizzle from their model increased cloud fraction by 34% over most of the region.

Model predictions of a strong dependence of cloud fraction on drizzle rate are not necessarily borne out by the observational record. Austin et al. (1994b), for example, discussed aircraft observations in stratocumulus from three days off the coast of California. On each day, precipitation was observed beneath cloud and at the surface, yet satellite imagery showed the cloud decks to be solid and continuous for hundreds of kilometers around the aircraft flight tracks. Austin et al. (1994b) showed that, even in the presence of drizzle, transport of moisture from the surface into the mixed layer by small scale (< 2 km) eddies was able to replenish the water loss at the surface by precipitation. These results agree with those of Paluch and Lenschow (1991), who demonstrated that, although evaporating precipitation did suppress transport by eddies bigger than about 10 km, heat and moisture were still efficiently transported away from the surface by small scale eddies.

An understanding of the processes controlling cloud fraction in the marine boundary layer has been sought for some time, and cloud microphysical processes and precipitation are of course only one candidate. Large regions may be temporarily cleared of boundary layer clouds by synoptic scale processes such as off-shore flow (Kloesel, 1992) or enhanced sub-

sidence (Weaver and Pearson, 1990). Of more climatological relevance are mechanisms such as cloud top entrainment instability (CTEI, see Deardorff, 1980; Randall, 1980) in which evaporative cooling of mixtures of entrained and cloudy air is thought to lead to increased turbulence levels and runaway entrainment. The CTEI criterion has not proved a good predictor of cloud fraction, however (Kuo and Schubert, 1988). Physical and numerical models (Siems et al., 1990; Siems and Bretherton, 1992) indicate that this is because very few parcel mixtures become dense enough to significantly increase entrainment. An alternative view was offered by Bretherton (1992) who, in attempting to explain the observed downwind evolution of stratocumulus to trade cumulus, suggested that cloud fraction should tend to decrease as boundary layer depth increases because deeper boundary layers are more likely to be decoupled. He also noted that boundary layer deepening might be caused by an increase in sea surface temperature relative to the free tropospheric temperature.

1.2.4 SHIP TRACKS

Ship tracks provide a vivid illustration of the interplay between microphysics and bulk cloud properties. First noted by Conover (1966), ship tracks are visible from space as curvilinear regions of enhanced brightness in low cloud decks associated with the passage of ships in the ocean underneath. The features can be hundreds of kilometers in length and can persist for several days.

More recent investigations have identified two classes of ship tracks. One class, as observed by Conover, shows a large contrast in albedo compared to the surrounding environment. Radke et al. (1989) investigated ship tracks of this type off the coast of California using coordinated in situ and remote sensing measurements. They found that, relative to the surrounding clouds, these tracks contained more and smaller droplets and higher liquid water content. They surmised that the increased liquid water content was due to suppression of drizzle through reduction of autoconversion. A second type of ship track has been investigated primarily from space. Coakley et al. (1987) used observations of droplet size made using near-infrared (3.7 μm) radiances to identify ship tracks in which the droplet size had changed significantly relative to the surrounding environment. They noted that, although

the tracks were clearly identifiable by the changes in droplet size, the tracks showed no significant increase in their already high albedo.

Ship tracks exist as isolated small-scale features in an otherwise relatively homogeneous marine environment. Although ships do inject heat and water vapor into the atmospheric boundary layer, the largest differences measured by aircraft between tracks and the ambient environment are typically in the number concentration of cloud droplets and CCN. The dramatic and persistent modification of cloud albedo and cloud liquid water in response to this injection shows that, at least under some circumstances, cloud microphysics can strongly modulate cloud radiative properties.

1.3 *The Lagrangian Evolution of Stratocumulus*

I have described two possible links between cloud microphysics and cloud bulk properties: the modulation of albedo by changes in droplet number concentration, and the control of cloud fraction by drizzle. The former hypothesis is based primarily on theoretical arguments which have assumed, perhaps naively, that liquid water content is unaffected by changes in droplet concentration, while the latter is based on relatively simple models of the marine boundary layer. Both arguments could stand a bit of rigorous observational testing. Observations of marine stratocumulus, however, must first contend with the Lagrangian nature of cloud evolution.

Marine stratocumulus differ from most other types of clouds in their large areal extent and very long lifetime. The regions covered by stratocumulus shown in Figure 1-2 are many hundreds of kilometers in extent. An air parcel advected by the climatological winds in, for example, the eastern Pacific, takes about a week to cross the region. This means that, in a frame of reference moving with the mean wind, a column of boundary layer air can remain capped by stratocumulus for several days. Along this trajectory the column is subject to a constantly changing large scale environment. In particular, the parameters which control boundary layer evolution (sea surface temperature, mean wind, divergence, upper air conditions) all change with time, some at appreciable rates. In the meantime, the cloud need not be in equilibrium with its local environment. Observations of stratocumulus evolution,

therefore, should be made in a *Lagrangian* frame of reference following the motion of the boundary layer air.

The rationale underlying a Lagrangian observational strategy is discussed in detail in Bretherton and Pincus (1994). Essentially, a Lagrangian approach is most appropriate when (as is the case for marine stratocumulus topped boundary layers) boundary layer structure is dominated by vertical rather than horizontal mixing, so that it makes sense to observe the temporal evolution of a column of boundary layer air. Interactions with neighboring columns through horizontal mixing are considered unimportant, so flow across the column boundaries is ignored. In the absence of wind shear in the boundary layer the column motion is deduced from the wind velocity; if shear exists, the mass-weighted average wind speed is used.

The importance of temporal changes in large scale environmental parameters in determining marine stratocumulus evolution is strikingly clear in modelling studies. Figure 1-5 shows simulations of the diurnal cycle of the marine boundary layer (C. Bretherton, personal communication) using a one-dimensional third order turbulence closure model (Bretherton, 1994). The upper panels, which were performed with fixed boundary conditions representing climatological conditions at 27 N, 132 W, show the evolution over 24 hours of liquid and total water mixing ratios. There is a large diurnal variation in cloud amount, and the boundary layer becomes decoupled during the day, as evidenced by the vertical gradient in total water. The simulations do not reproduce the observations well, since low cloud fraction is at a maximum at this location, and the observed diurnal variability is much smaller than the model predicts (Rozendaal et al., 1994). The observations are more closely matched by the lower panels, which show simulations in which the boundary conditions (sea surface temperature, wind speed, etc.) are changing along a climatological trajectory running from 40 N, 130 W.

The large effect of temporally evolving boundary conditions on cloud properties is not dependent on the type of model used to simulate the stratocumulus. Wyant and Bretherton (1992), for example, noted substantial differences between Lagrangian and steady state solutions in a mixed layer model. Wang et al. (1993) incorporated advective tendencies into a two layer, one-dimensional mean-gradient model of the boundary layer, and found that

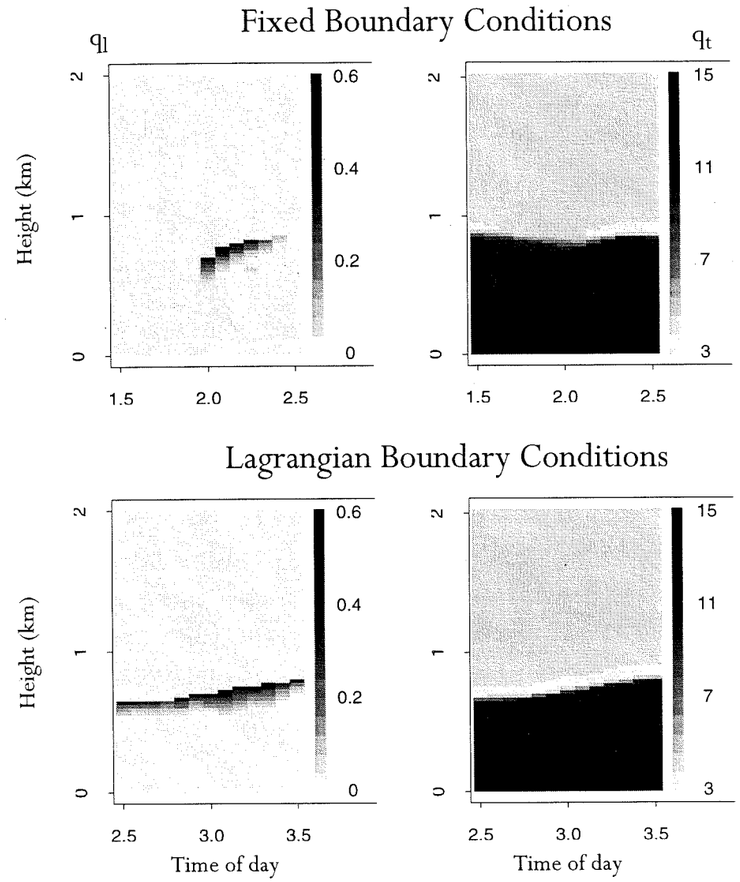

FIG 1-5. Simulations of the diurnal cycle of marine boundary layer cloudiness with fixed and changing boundary conditions. The upper pair of panels shows liquid water content (left) and total water content (right) over the course of one day beginning at local noon. Daytime clearing and decoupling are evident when boundary conditions are fixed. Simulations in a moving frame of reference (lower panels) more accurately reproduce the high cloud fraction and boundary layer structure observed at this location. Simulations courtesy C. Bretherton.

the advective components in both the inversion height and water budget equations were significant.

The Lagrangian nature of stratocumulus evolution also appears vividly in the observational record. Klein et al. (1994) examined a twenty-five year times series of observations at Ocean Weathership N, located at 30 N, 140 W, and found that changes in cloud amount at Ship N were better correlated with sea surface temperatures 24 to 30 hours upstream from the ship than with the local sea surface temperature.

1.4 *Observing Lagrangian Evolution*

Both observations and models suggest that marine stratocumulus evolution is most appropriately studied in a Lagrangian frame of reference which moves with the mass-weighted wind speed in the boundary layer. This poses a difficult task for traditional cloud physics observational platforms: ground- or ship-based remote sensing platforms can move slowly if at all, while instrumented aircraft have flight durations much shorter than the time scales over which cloud evolution occurs. Despite these obstacles, two Lagrangian experiments were performed during the Atlantic Stratocumulus Transition Experiment (ASTEX, see Albrecht et al., 1994). During these experiments (Bretherton and Pincus, 1994), constant-pressure balloons equipped with position transponders were released into the marine boundary layer from ships. Three aircraft then flew a series of tag-team missions from an island airfield to the vicinity of the balloons. The aircraft were, in principle, able to document the evolution of the boundary layer over the course of a day and a half.

The ASTEX Lagrangian experiments highlighted the difficulties inherent in making measurements in a moving frame of reference. During the first experiment, for example, all the tracking balloons sank in the ocean within the first few hours after launch, necessitating the computation of airmass trajectories from operational weather analyses. Bad weather grounded all aircraft for fourteen hours during the first experiment. Though the experiments proved fruitful, they were difficult and expensive to perform, and provided detailed information about cloud evolution in only two circumstances.

We have arrived at a dilemma. Models predict that cloud microphysical processes and precipitation may play a substantial role in controlling the radiative properties of clouds in the

marine boundary layer by modifying both cloud albedo and cloud fraction. Observational tests of these and other model predictions have not been forthcoming, however, in large part because the evolution of the system takes place in a moving frame of reference, which has made in situ observations impractical. It is this conundrum which motivates the work described in the rest of this dissertation. In the next chapter I develop an observational tool for the Lagrangian observation of marine stratocumulus evolution from space, and in Chapter 3 use this tool to assess the relative importance of microphysical variability and the rate of change of sea surface temperature in controlling cloud fraction in the marine boundary layer. Chapter 4 uses detailed simulations of marine stratocumulus evolution to confirm and begin to explicate the observational results. In Chapter 5 I develop a simple model to explore the role of precipitation induced changes in cloud thickness in the modification of cloud albedo.

2 The Lagrangian Observational Technique

I have developed a technique for observing the Lagrangian evolution of clouds from space which can serve as a complement to in situ measurements in process studies of marine boundary layer clouds. The technique uses a combination of operational weather analyses and visible and infrared imagery from geostationary satellites. Temporally and spatially varying winds from the synoptic analyses are used to compute the trajectories of boundary layer air parcels as they are advected by the mean wind from their initial positions. At regular time intervals, I extract mesoscale sized regions from the satellite image centered on the parcel position, then estimate cloud characteristics from the image. This process provides a time history of cloud properties and environmental conditions along the parcel trajectory. A schematic sketch of the technique is shown in Figure 2-1.

2.1 *Computing Parcel Trajectories*

The Lagrangian technique requires environmental information and satellite images covering the geographical region and time period of interest. The studies described in Chapter 3 use observations obtained during the marine stratocumulus component of the First ISCCP Regional Experiment (FIRE, see Albrecht et al., 1988 for an overview) which took place off the coast of California from 29 June to 17 July 1987. In this section I detail both the computational methods on which the technique is based and the data sets I use for the FIRE investigations. The technique itself, however, is entirely general, and could be applied to any region in which satellite imagery and environmental information are available.

2.1.1 ENVIRONMENTAL DATA SETS

As part of its routine weather forecasting activities, the National Meteorological Center prepares gridded synoptic analyses for the NGM (Nested Grid Model) weather prediction model. These "0 hour forecasts" are synthesized from a combination of radio- and dropsonde profiles, satellite temperature profiles, cloud track winds, and single level station data using the Regional Optimum Interpolation method (DiMego, 1988), which attempts to provide a dynamically consistent analysis. The analyses are archived on a 2.5 degree latitude-longitude grid every 12 hours, and are available from the NCAR Data Support Section

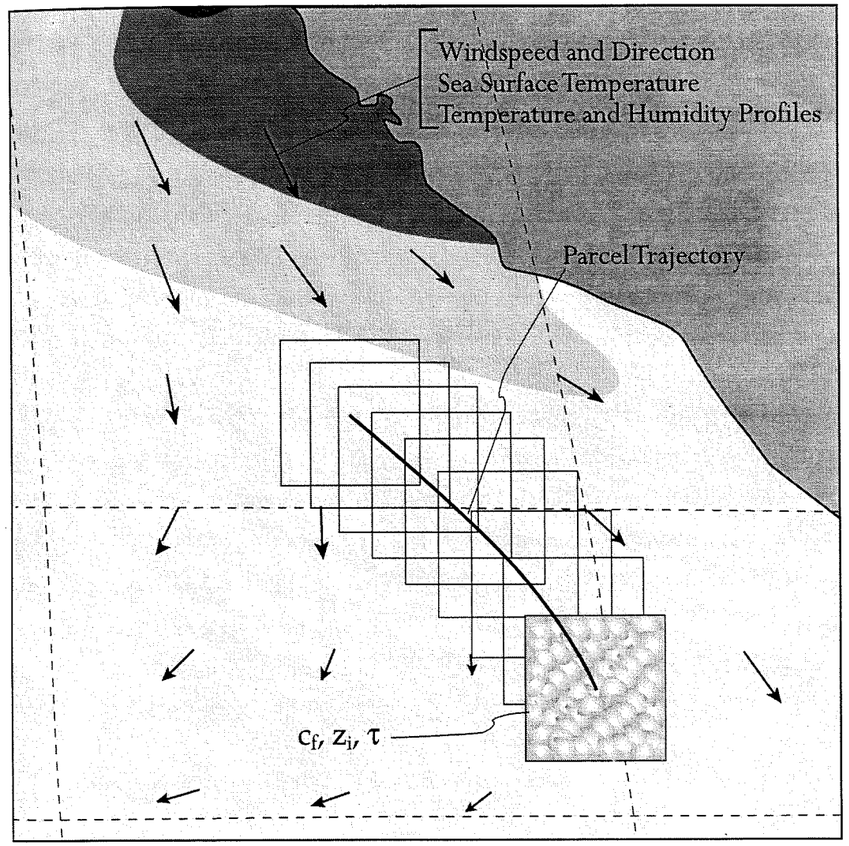

FIG 2-1. The Lagrangian observational technique. Environmental analyses provide spatially and temporally varying wind, temperature, and moisture fields. Parcel trajectories and the history of the environment along them are computed from the wind fields. At regular intervals, visible and infrared images centered on the instantaneous parcel position are extracted from the large scale images obtained by geostationary satellites. Each image is analyzed to determine cloud properties such as cloud fraction, cloud optical thickness, and boundary layer depth.

as dataset 84. For this study I have extracted a subset of the analyzed parameters: the winds, temperature, and relative humidity fields at the 1000, 850, and 700 mb levels.

The sea surface temperature (SST) varies more slowly and has steeper gradients in the FIRE region than do the atmospheric parameters cited above. SST has historically been measured using ship engine intake temperatures (Woodruff et al., 1986) but the advent of satellites has allowed for more spatially uniform coverage. The Multi-Channel Sea Surface Temperature algorithm (MCSST, see McClain et al., 1985) uses infrared radiance observations in several wavelength bands from the AVHRR sensor aboard the NOAA polar orbiting satellites to estimate sea surface temperature. The technique uses a variety of tests to detect and remove observations containing clouds, and corrects for atmospheric attenuation by examining the difference in brightness temperature between each pair of bands. The operational version of this dataset reports sea surface temperatures weekly on an 18 km grid. In those locations covered by cloud during every satellite observation the value of SST is interpolated from available observations using a relaxation procedure.

2.1.2 SATELLITE DATA SET

The Lagrangian technique derives the time history of cloud properties from sequences of satellite images. Temporal continuity of the image series requires the use satellites placed in geostationary orbits 35,800 km above the Equator in which the platform remains above a fixed longitude. Satellites have been placed in these orbits since 1966, beginning with the Applications Technology Satellites (ATS). The ATS series was intended primarily for communications, although Spin-Scan Cloud Cameras were included in the payload.

The first of the Geostationary Operational Environmental Satellite (GOES) series was launched in 1974. These platforms originally carried the Visible and Infrared Spin Scan Radiometer (VISSR), which was superceded by the VAS (VISSR Atmospheric Sounder) instrument with the deployment of GOES-4 in 1980. The GOES platforms have traditionally been operated in pairs, one at the GOES-East position (75° West longitude), the other at GOES-West (135° West).

Both VISSR and VAS obtain narrow band images of the Earth in the visible (0.55 μm to 0.70 μm) and infrared (10.5 μm to 12.6 μm, in the water vapor window) portions of the

electromagnetic spectrum. Images of the Earth's disk are constructed by stepping a mirror from north to south while the satellite spins on its axis at 100 RPM. At full spatial resolution, each pixel nominally covers 1 km in the visible imagery and 4 × 8 km in the infrared imagery. The visible images are not radiometrically calibrated, so the conversion of instrument brightness levels to a physical quantity such as radiance is accomplished through various *a posteriori* methods. Infrared radiances are converted to brightness temperatures (assuming an emissivity of 1) during routine data processing. VAS images are available every 30 minutes.

During the FIRE period, the GOES-6 spacecraft was stationed at the GOES-West position. Full resolution VAS images extending northeast from 23° N, 135° W were archived by the FIRE Project Office and are available in GOES AAA format (Dean and Campbell, 1988). With the exception of the period from 1600 GMT on 9 July to 1400 GMT on 10 July, most images were received and processed normally. The National Climate Data System graciously provided a copy of this data set, which is enormous by today's computational standards. One pair of VIS and IR images, packed in AAA format, occupies roughly 17 megabytes (Mb). An unpacked VIS image of the FIRE region (23° N to 50° N, 135° W to 115° W) with its earth-location information is about 104 Mb, which can be reduced to about 59 Mb by replacing the floating point representation of visible wavelength reflectance with an 8-bit lookup table. The dataset comprises observations every half hour for 20 days, for a total of more than 28 Gb of visible data and another 14 Gb of infrared imagery. By way of comparison, the current edition of Oxford English Dictionary, containing meaning and etymology for every word in the English language, contains about 6 billon printed characters (6 Gb).

One note of caution about this dataset is in order. During the FIRE project, images from the water vapor absorption channel (channel 10, centered at 6.7 μm) were transmitted by the satellite four times a day (at 0515, 1115, 1715, and 2315 Z) in lieu of the normal window channel (channel 8). These images are incorrectly coded in the AAA format as channel 8. It is difficult to confuse the two types of images, however, since the radiance received by the channel 10 sensor comes from much higher in the atmosphere, so the temperatures are much colder than are ever seen in channel 8.

2.1.3 COMPUTATION OF TRAJECTORIES AND ENVIRONMENTAL PARAMETERS

To compute an air parcel trajectory, I choose an initial position and starting time, then integrate the two-dimensional equations of motion on the spherical Earth's surface:

$$\frac{d\theta}{dt} = v_y(\theta, \phi, t) \times \frac{360}{2\pi R_E}$$
$$\frac{d\phi}{dt} = \frac{v_x(\theta, \phi, t)}{\cos\theta} \times \frac{360}{2\pi R_E} \qquad (2\text{-}1)$$

where the coordinates of instantaneous position latitude θ and longitude ϕ (degrees) are modified by the meridional (north-south) and zonal (east-west) winds v_y and v_x (m s^{-1}), and R_E the radius of the Earth. I use a fifth-order adaptive time step Runge-Kutta integrator adapted from the routine ODEINT of Press et al. (1986). Since the gridded environmental information described in §2.1.1, including the wind fields needed to integrate the equations of motion, is available only at discrete times (the analysis times) and places (the grid points), parameter values at arbitrary locations and times are linearly interpolated in space and time from the gridded values. Periodically (usually every half hour), I report the parcel position and the interpolated values of the environmental parameters at that position, then extract from the large scale visible and infrared satellite images a mesoscale-sized region (roughly 250 km on a side) centered on the parcel position. From this sequence of images I determine the cloud properties as function of time using the techniques described in §2.2.

Since my studies focus on boundary layer clouds, I ignore vertical motion and shear in (2-1), and use the wind fields at 1000 mb to determine the isobaric trajectory of boundary layer parcels. Equation (2-1) may be used only in the boundary layer and I can say nothing about, for example, the history of parcels above the boundary layer inversion. A more general solution would be to incorporate a third equation in the set and solve for the three dimensional position as a function of time. This would require analyzed fields of vertical velocity as a function of height, which is notoriously difficult to determine. As an alternative, one could compute three dimensional isentropic trajectories above the inversion.

2.2 *Computing Cloud Parameters*

The use of satellite observations in studies of cloud evolution is an exercise in compromise. Compared to more traditional observational platforms (aircraft, balloon-borne sensors, and ground based radiometers), geostationary satellites have the distinct advantages of uniform and larger scale spatial and temporal coverage. On the other hand, operational satellite instruments can measure only a finite number of radiances (typically two) at the top of the atmosphere. To place the remote sensing observations in the context of more traditional observations I develop techniques to interpret the top-of-the-atmosphere radiances in terms of cloud properties, focussing on the retrieval of three parameters (cloud fraction c_f, cloud optical depth τ, and boundary layer depth z_i) and on the interpretation of cloud optical depth in terms of liquid water path.

2.2.1 CLOUD DETECTION AND CLOUD FRACTION

Cloud detection plays two roles in the retrieval of cloud properties. Cloud fraction, typically defined as the cloudy area in a scene divided by the total area, is a quantity of interest in itself since cloud and general circulation models predict this parameter. Cloud detection is also the necessary precursor to the determination of cloud properties, since these properties are defined only for those segments of an image which do in fact contain cloud. Unfortunately, there exists no unambiguous way to divide satellite images into clear and cloudy segments. This is not a result of limitations in technology or conceptual understanding, but a reflection of the fact that cloud radiative and microphysical properties may vary enormously on a wide range of spatial and temporal scales.

Cloud detection algorithms attempt to classify each pixel or group of pixels in a scene as clear or as one of a finite number of types of cloud, each of which is assumed to be well represented by a single set of parameters. Cloud properties, however, may not be homogeneous within a scene or even within a pixel, and some properties (such as visible wavelength reflectance) can vary enormously over relatively small spatial scales. The selection of a cloud detection algorithm, therefore, represents a fundamental choice, and is essentially equivalent to deciding what defines a cloud. For a thoughtful discussion of this subject see Rossow et al. (1985) and Rossow (1989).

Cloud detection schemes fall broadly into two classes: those based on the application of thresholds to one or more radiances on a pixel-by-pixel basis, and those based on the properties of small groups of pixels. The choice depends somewhat on the application, with the former techniques being more useful when further analysis is to be done on the cloudy pixels. Every cloud detection algorithm, however, requires that some parameter exceed a threshold value, and the primary distinctions between algorithms center on what quantity is being tested and on how the thresholds are determined. Rossow et al. (1989) provides a comprehensive survey of cloud detection methods, several of which are discussed in detail in Rossow et al. (1985).

Pixel-by-pixel methods compare the visible and/or infrared radiance for each pixel in turn with radiance values thought to represent clear sky or cloud free conditions. If the observed radiance differs in the correct direction from the clear sky value (i.e. colder in the infrared and brighter in the visible) by an amount exceeding some threshold, the pixel is labeled cloudy; if not, it is labelled clear. The major differences between techniques of this type center on how clear sky visible and infrared radiance values are determined, the amount by which a pixel must exceed these clear sky values to be considered cloudy, and on the decision logic used when the tests in the two channels don't agree. The clear sky radiance values may be set by examining the variability of visible or infrared radiance in time (Rossow et al., 1985) or space (Coakley and Bretherton, 1982), and may determine clear sky radiances for each channel separately (Rossow et al., 1985) or both in tandem (Minnis and Harrison, 1984).

A great deal of attention has been paid to the determination of clear sky radiances and the selection of radiance thresholds because a general cloud detection algorithm such as the one developed for ISCCP must detect clouds (which may vary enormously in visible reflectance and infrared emissivity) over many types of surfaces (with different spectral reflectances and temperatures) under a wide range of viewing conditions. Fortunately, I can rely on much simpler techniques, since the detection of boundary layer cloud over the ocean, though it presents some unique difficulties, is by and large a much more tractable problem. The ocean albedo is low and does not vary significantly with time. Spatial and temporal changes in sea surface temperature over synoptic scale regions are also small compared to the difference

between the ocean and cloud temperatures. This means that the clear sky values of both infrared and visible radiance are fairly well constrained and need not be determined from the image itself. On the other hand, any given mesoscale-sized image may not contain clear sky, or even broken clouds through which the ocean can be seen, which implies that individual images cannot be relied upon to provide clear sky radiance values.

The Lagrangian technique uses a cloud detection algorithm both to compute cloud fraction and to identify cloud pixels for which cloud optical depth (§2.2.2) may be retrieved. Unfortunately, the differing resolutions of the visible and IR pixels from the VAS sensor make it difficult to relate decisions based on IR images to the VIS images. This difficulty arises in part because it is somewhat problematic to determine exactly which 32 visible pixels correspond to each IR pixel. Several bispectral algorithms (Minnis and Harrison, 1984; Rossow et al., 1985) avoid this problem by reducing the spatial resolution of the visible data to match that of the IR, but this is a poor choice in light of the already small number of pixels in the mesoscale images. Additionally, it is not clear how cloudiness decisions made using a single IR radiance ought to be applied to a group of pixels in which the visible radiances vary.

In light of these difficulties I choose two simple cloud detection algorithms. The VIS technique, available only during daylight hours, is based on a visible reflectance threshold. In the spirit of the ISCCP cloud detection algorithm (Rossow et al., 1991) I construct minimum reflectance maps for the FIRE region at three times of day (1615, 2015, and 0015 GMT) by determining the minimum reflectance observed in each pixel in the region during the FIRE period. From these maps I determine a regional average sea surface reflectance of 0.05. The VIS cloud detection algorithm simply requires that the visible radiance in the pixel exceed a minimum value, typically 0.08, corresponding to the observed minimum reflectance plus the calibration uncertainty of 0.03 (Han et al., 1994). This threshold is conservative, in the sense that any pixel containing even a small amount of cloud is likely to be flagged as cloudy. An alternative approach might choose a larger threshold such that the satellite-derived cloud fractions agreed with some ground based estimate. I will return to this point in §2.3.5. The VIS algorithm provides an estimate of cloud fraction during the day, and is used to segregate visible pixels into clear and cloudy populations prior to the retrieval of optical depth (§2.2.2).

A second cloud detection algorithm (IR) compares the VAS-measured infrared temperature with the MCSST estimates of sea surface temperature (§2.1.1). Infrared pixels are flagged as cloudy if the VAS-measured temperature for the pixel is colder than the MCSST temperature at the center of the image by some threshold. In practice, the threshold is typically set at 4 K, which is the sum of the 1 K MCSST-VAS bias (see Table 3 in McClain et al., 1985) and an average of the temperature thresholds used in the ISCCP algorithm over coastal waters and the open ocean (Rossow et al., 1991). The IR cloud fraction estimate is available both day and night.

2.2.2 OPTICAL DEPTH

The VIS cloud detection scheme described in §2.2.1 uses the visible wavelength radiance of each pixel in the simplest possible way, comparing the measured value to a predetermined threshold in order to make a binary decision about whether or not the pixel is cloudy or clear. A more complicated analysis allows the radiance information to be used to estimate cloud optical depth, which I introduced in §1.2.1. Because top-of-the-atmosphere radiance is a strong function of optical depth, cloud optical properties may be inferred by comparing the *predictions* made by radiative transfer models of outgoing radiance as a function of cloud optical properties with *observations* of the radiance made by satellites. The models used for the comparison must be sophisticated enough to fully resolve the angular distribution of the reflected solar radiation, since this distribution shows strong anisotropy as a function of the viewing and illumination geometry, as well as the optical properties of both atmosphere and cloud (see, for example, Figure 3 of Minnis et al., 1992).

Several variations of the comparison technique have been employed. Kriebel et al. (1989) converted radiance measurements to albedo estimates using empirical bidirectional reflectance models developed from many observations of cloudy scenes for ERBE (Taylor and Stowe, 1984; Suttles et al., 1988), then inferred cloud optical depth from albedo using the parameterization of Stephens (1978). This technique, though somewhat inaccurate, has the advantage of being computationally very efficient. Michael King and his collaborators have focussed on analytic asymptotic methods (King, 1987; Nakajima and King, 1990; Nakajima et al., 1991), which compare the cloud reflection to that predicted for an optically semi-infinite cloud. This method works well at optical depths larger than about 7, and has been

extensively applied to measurements made from aircraft, in which corrections for the atmospheric layer between the sensor and cloud are unimportant. The most common scheme, however, is the so-called "look-up table" approach used by ISCCP (Rossow et al., 1991) and other investigators (Minnis et al., 1992). I have implemented a retrieval scheme of this type which I outline here, deferring a detailed treatment of the radiative transfer modelling and optical depth retrieval technique to Appendix A.

Because the ISCCP radiance calibrations I use (Desormeaux et al., 1993) standardized to on the AVHRR sensor aboard NOAA-7, I initially employ an angularly resolved radiative transfer model to predict the reflected radiance observed by this instrument at the top of the atmosphere as a function of cloud optical depth τ, solar zenith angle cosine μ_0, viewing zenith angle cosine μ, and relative azimuth ϕ. The radiative transfer model incorporates scattering by cloud droplets, aerosols, and molecules (Rayleigh scattering), absorption by gasses and aerosols, and reflection by the ocean surface underlying the cloudy atmosphere. The results are weighted by the solar spectrum and the response curve of the satellite radiometer. I make calculations for a variety of optical depths, and store the results as a four-dimensional array describing the model predictions of radiance $L(\mu_0, \mu, \phi, \tau)$.

To retrieve cloud optical depth for a pixel labelled as cloudy by the cloud detection algorithm, the VAS instrument brightness levels are converted to a radiance value L_{obs} as measured by the standard instrument using the ISCCP calibration algorithm (Desormeaux et al., 1993). The latitude and longitude of the sub-solar point are computed from the time and day of year. Using this information, as well as the latitude and longitude of the sub-satellite point and the pixel in question, I compute the viewing and illumination geometry (μ_0, μ, ϕ). With these angles fixed, I linearly interpolate the lookup tables to get a prediction which depends only on τ, then vary τ until the linearly interpolated prediction $L(\tau) = L_{obs}$.

2.2.3 BOUNDARY LAYER DEPTH

Minnis et al. (1992) introduced a technique which I have adopted for estimating boundary layer depth (defined here as cloud top height) from estimates of SST and cloud top temperature. The VAS IR images provide the effective blackbody emission temperature of each 4 km pixel. Boundary layer depth z_i (km) is computed by assuming a fixed temperature lapse rate (based on an average of many aircraft soundings) in the boundary layer and computing the

difference between the median cloud top temperature T_c (K) reported by the satellite sensor and the sea surface temperature SST interpolated from the environmental fields

$$z_i = \frac{SST - T_c}{7.1} \tag{2-2}$$

2.2.4 LIQUID WATER PATH

Cloud optical depth (§2.2.2) is an appealing quantity because it can be retrieved directly from visible radiance observations. However, it is not a particularly useful variable for process (as opposed to radiative) studies of clouds since optical depth is sensitive to changes in both liquid water path and droplet radius, both of which may be affected by bulk cloud processes. Additionally, optical depth is predicted only indirectly by most cloud models. I therefore employ the simplest possible model of cloud microphysics to indirectly estimate cloud geometrical thickness and liquid water path (the vertically integrated cloud liquid water content; see §1.2.1) from optical depth measurements. I assume that the liquid water content (g m^{-3}) in the cloud increases linearly with cloud thickness h at some fraction c of the adiabatic lapse rate, so that liquid water path LWP obeys

$$LWP = \frac{c\beta_m h^2}{2} \tag{2-3}$$

where β_m is the lapse rate of saturation mixing ratio during saturated (moist) adiabatic ascent, and is a weak function of temperature.

If the number concentration of cloud droplets N (m^{-3}) is known and the cloud water at cloud top is divided equally among these drops, then:

$$\frac{4\pi}{3}\frac{\rho_l}{\rho_a} N r^3 = c\beta_m h \tag{2-4}$$

where ρ_a and ρ_l are the densities of air and liquid water, respectively. Equation (2-4) can be solved for the cloud top droplet radius r, and substituted along with (2-3) into (1-4) to yield an estimate of geometric cloud thickness in terms of cloud optical depth

$$h = \left[\frac{16}{9\pi}\left(\frac{\rho_l}{\rho_a}\right)^2 \frac{\tau^3}{c^3 N \beta_m^2}\right]^{1/5} \tag{2-5}$$

Liquid water path may then be estimated from (2-3) and (2-5), and varies as $N^{-2/5}$.

2.3 *Uncertainties in Trajectory and Cloud Parameters*

In this section I discuss the uncertainties in the computation of the air parcel trajectories and in the environmental and cloud parameters derived along the trajectories. In the absence of other, independent, measurements of the derived quantities, it is impossible to assess the uncertainty in individual parameter estimates. Instead, I focus here on understanding the average uncertainty to be expected in each parameter.

2.3.1 SPATIAL TRAJECTORY

The Lagrangian observational technique has at its heart the trajectories computed using the methods described in §2.1.3. Since the numerical method used to integrate the trajectories is far more precise than the wind data available, the uncertainty in the calculated parcel trajectories stems from uncertainties in the wind velocity fields provided by the NMC analyses, and interpolated in space and time. Two questions arise: to what extent are the 1000 mb winds representative of the boundary layer winds, and how accurately do the NMC analyses depict the true 1000 mb winds?

The winds at 1000 mb cease to represent the mass-weighted boundary layer wind velocity in the presence of vertical shear in either wind speed or direction. In general, the amount of wind shear in the subtropical marine boundary layer varies in time and space, and no data source exists which allows me to assess the magnitude of the wind shear at any particular location and time. However, observations in the FIRE region made from aircraft (Brost et al., 1982; Austin et al., 1994b), and balloons (Hignett, 1991) consistently show little evidence of wind shear, so I assume that the 1000 mb winds are in fact representative of the boundary layer flow.

The accuracy of the analyzed wind fields is a thornier question. Over the ocean, the analyzed fields are synthesized from sparse ship and buoy reports and from cloud track winds, which are derived by following cloud features observed by satellites. A quantitative estimate

of the uncertainty in the wind fields is difficult to determine, however, because there are no independent estimates of wind speed and direction in the FIRE region to compare to the NMC analyses.

Kahl and Samson (1986) examined the uncertainty of trajectory calculations made over the central and eastern United States. By comparing the interpolated predictions from the standard National Weather Service analyses with high spatial- and temporal-resolution measurements made during a field project, they determined that winds interpolated from the standard analyses had randomly distributed errors of 2–4 m/s. They then used these error distributions to estimate the total error in the trajectory as a function of transport time. Their figure 12 is shown as Figure 2-2. After 24 hours, they indicate an uncertainty in position of about 200 km, which increases after 36 hours to about 250 km.

The applicability of Figure 2-2 and the results of Kahl and Samson (1986) in the FIRE region are somewhat unclear. Summertime winds in the FIRE region are quite steady and easy to predict, but the measurement network is extremely sparse. It is therefore likely that sys-

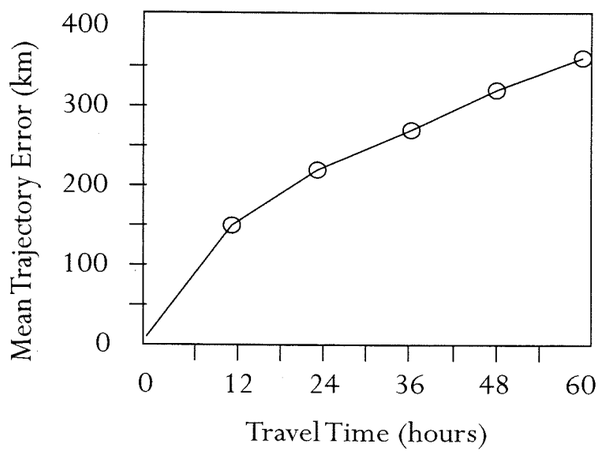

FIG 2-2. Estimated error in final trajectory position assuming random errors in wind speed. The random errors are drawn from a measured distribution with an average value of 2 m/s. After Kahl and Samson (1986).

tematic (rather than random) errors will dominate the uncertainty in computed trajectories. In Chapter 3, therefore, I assess the robustness of my results by perturbing the wind fields by fixed constants and recomputing both the trajectories and the cloud properties along them.

2.3.2 TEMPERATURE AND HUMIDITY

The NMC analyses also provide a history of temperature and humidity above the inversion along the trajectory. In contrast to the wind fields, independent measurements of these quantities were made during FIRE by approximately 70 radiosondes launched from San Nicholas Island during FIRE by the Colorado State University CLASS system (Schubert et al., 1987). These soundings were not incorporated into the NMC operational analyses. The comparison is an optimistic one, since San Nicholas Island is quite close to the California coast and errors in lower tropospheric temperature and humidity are likely to increase with distance away from the land based sounding network.

Figure 2-3 shows a comparison between 850 mb temperature and water mixing ratio as measured during the CLASS soundings and as interpolated from the NMC analyses. I compute the average temperature and water vapor mixing ratio from the CLASS soundings in the 10 mb layer around 850 mb, and compare the CLASS values to the NMC analyses interpolated to the location of San Nicholas Island at the time of the rawinsonde launch. This approach neglects the time it takes the balloon to rise to 850 mb, and the amount the balloon will drift away from the island during that time. At a balloon ascent rate of 5 m/s and a wind speed of 10 m/s, the balloon will reach 850 mb roughly 5 minutes after the launch time, and will have drifted about 3 km in that time.

Figure 2-3 suggests that, at least near the coast, 850 mb temperature estimates from the NMC analyses are quite reasonable, but that the moisture estimates show too little variability and, in general, overestimate the actual water mixing ratio. This is in agreement with Betts et al. (1992), who noted that the 850 mb level is often considered part the boundary layer by the NMC analyses.

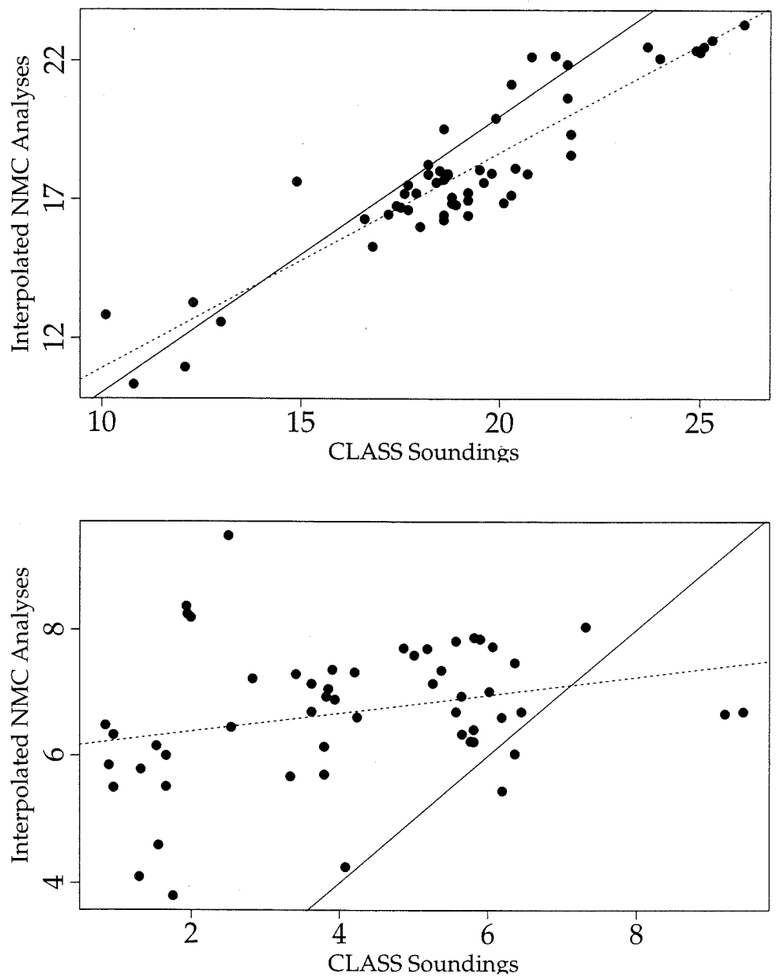

FIG 2-3. Comparison of temperatures and mixing ratios as interpolated from NMC analyses and measured by radiosonde soundings made from San Nicholas Island during FIRE. Solid lines indicate equality, dashed lines a linear least squares fit through the data.

2.3.3 SEA SURFACE TEMPERATURE

In investigating the accuracy of the MCSST sea surface temperature algorithm, McClain et al. (1985) compared the satellite derived SSTs with those measured by buoys, ships, and other satellite radiometers. They report in their Table 4 a bias of about 0.2 K and an uncertainty of about 0.5 K in the MCSST measurements, as deduced from the standard deviation of collocated ship and satellite observations. Also of note is the 1–1.25 K bias reported between collocated MCSST and VAS derived temperatures which has been incorporated into the IR cloud detection algorithm (§2.2.1).

As an alternative assessment, Figure 2-4 shows a comparison of sea surface temperature as interpolated from the MCSST grids and as measured from the NCAR Electra. The Electra measurements (J. Eden, personal communication) are taken from downward looking infrared pyronometer measurements made during every straight and level run made below 100 m during FIRE. The Electra measurements are averaged across the run, and compared to the interpolated MCSST value at the midpoint of the run. The agreement is reasonable in the limited range of measurements available, though the interpolated MCSST values tend to be higher than the Electra-measured values.

2.3.4 BOUNDARY LAYER DEPTH

The estimate of boundary layer depth described in §2.2.3 depends on three quantities: the VAS-measured cloud top temperature, the MCSST-estimated sea surface temperature, and the assumed lapse rate. In the absence of alternative temperature measurements it is difficult to assess the absolute uncertainty in VAS-measured temperatures. The effect of discretization, however, is quite noticeable. In the temperature range typical of stratocumulus cloud-top temperatures the VAS sensor has a resolution of about 0.5 K, which is roughly the same as the uncertainty in MCSST estimates described in the previous section. The gridded sea surface temperatures vary smoothly, though, while the median cloud top temperature takes on discrete values. At the standard lapse rate described in §2.2.3, discretization and SST errors combine to yield an uncertainty of 100 m in boundary layer depth. The lapse rate is also subject to uncertainty. Betts et al. (1992) compared the fixed lapse rate of 7.1 K/km to the lapse rate derived from NMC analysis and COADS SSTs using a mixing-line model. Their results indicate that, in the FIRE region, the fixed lapse rate is accurate to within 10–15%.

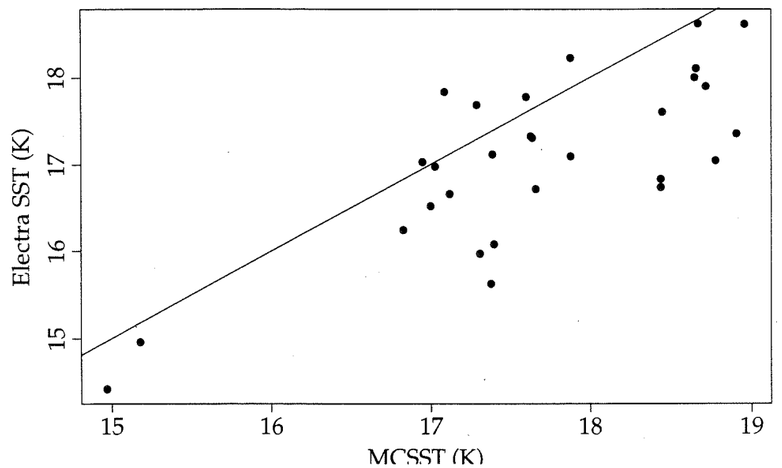

FIG 2-4. Comparison of sea surface temperatures interpolated from MCSST grids and measured by the NCAR Electra. The solid line indicates equality.

2.3.5 CLOUD FRACTION

As I described in §2.2.1, choosing an algorithm to determine cloud fraction amounts to defining a cloud as viewed from space. Quantifying the uncertainty in cloud fraction is difficult, then, because there is in general no objective "truth". One promising alternative was developed by Wielicki and Parker (1992), who used Landsat Thematic Mapper data with 30 m spatial resolution as cloud "truth", and examined the effects of spatial resolution on cloud fraction estimation. They showed that the ISCCP visible wavelength cloud detection algorithm, on which the VIS technique described in §2.2.2 is modelled, overestimates stratocumulus cloud fraction by about 8% at 1 km spatial resolution. Wielicki and Parker attribute this to the conservative radiance threshold used in the ISCCP algorithm (c.f. §2.2.1) which counts any pixel not entirely clear as fully cloudy, and note that the bias is a smooth function of the radiance threshold used.

In the absence of an unambiguous measure of cloud fraction to compare with the satellite-based estimates, I adopt the same philosophical approach to estimating the uncertainty in cloud fraction as described in §2.3.1: I compute cloud fraction using the conservative

threshold described in §2.2.1, then examine the robustness of the results as the radiance threshold is increased.

2.3.6 CLOUD OPTICAL DEPTH

Even given a perfect cloud detection algorithm, evaluating the uncertainty in cloud optical depth is a difficult task. Uncertainty in cloud optical depth arises from two sources: errors in the *model* used to represent the clouds, and errors in the *retrieval*. Only the errors arising from the latter source may be quantified.

All optical depth retrieval algorithms, including the method described in §2.2.2, rely on radiative transfer models which assume that each pixel is completely covered with a homogeneous cloud layer. The quantitative value of optical depth retrieved, therefore, applies exactly only to clouds which meet this criterion, but in general clouds within a pixel may exhibit both horizontal variability in optical depth and a more complicated geometric structure. Either of these departures from the conceptual model can affect the top-of-the atmosphere (TOA) radiance.

Consider first the effects of sub-pixel scale variability. Imagine a retrieval made for a single heterogeneous pixel, and define the area averaged optical depth as

$$\langle \tau \rangle = \frac{\int_0^\infty \tau' A(\tau') d\tau'}{\int_0^\infty A(\tau') d\tau'} \qquad (2\text{-}6)$$

where $A(\tau')$ is the fractional area covered by cloud of optical depth τ'. (Note that (2-6) is based on the independent pixel approximation, and holds only if each area considered does not, on average, exchange photons with any other area.) In this general representation broken clouds are those for which $A(0) > 0$ (Han et al., 1994), and the usual division of pixels into clear and cloudy fractions (e.g. Coakley and Bretherton, 1982) follows from considering only the two discrete values $\tau' = (0,\tau)$ in the optical depth distribution. Since finite changes in optical depth cause smaller changes in reflected radiance as optical depth increases (Pincus et al., 1994), the average radiance reflected from a heterogeneous pixel is always less than the radiance which corresponds to the average optical depth, even if the clouds remain perfectly plane parallel (Cahalan et al., 1994):

$$\langle L(\tau)\rangle < L(\langle\tau\rangle) \qquad (2\text{-}7)$$

The optical depth retrieved from an observed radiance, therefore, will be less than the area averaged optical depth if the cloud within a pixel is not completely uniform. In theory, this bias can be quite large. Kriebel et al. (1989) estimated errors in liquid water path of 25% due to relatively small amounts of horizontal variability, and Cahalan et al. (1994) found biases in optical depth as large as 30% using a multifractal model of cloud inhomogeneity.

Recognizing that clouds in the atmosphere are rarely the uniform sheets assumed by plane parallel radiative transfer models, many investigators have assessed the effects of cloud geometric shape and spatial distribution on the reflectance of broken cloud fields (McKee and Cox, 1974; Davies, 1984; Kobayashi, 1988, 1989 , 1993). Each simulation has shown that the reflectance can be substantially modified by effects related to the three-dimensional structure of the clouds such as shadowing and the lateral escape of photons from the cloud edges, and that the effects can be quite sensitive to the geometrical arrangement of the cloud and to the viewing and illumination angles. Though most studies assume a two-point distribution of cloud properties (i.e. a volume is either "clear" or "cloudy"), the same conclusions can be drawn from studies considering the effects of geometry alone (Kobayashi, 1993).

In the absence of any additional constraints, both horizontal cloud inhomogeneity and geometrical effects might introduce biases and uncertainties in retrieved optical depth large enough to render the retrieval of optical depth meaningless. There are several aspects of remote sensing, however, which make the situation much less dire than it may appear. Weak or moderate variability in cloud optical depth affects pixel scale radiance and retrieved optical depth only if the inhomogeneity exists on scales between the pixel size (about one kilometer for VAS) and the photon mean free path, roughly 100 meters in stratocumulus clouds (Cahalan et al., 1994). Observational evidence for significant variability on these scales is inconclusive. Korolev and Mazin (1993), for example, found that regions of decreased droplet concentration in stratiform clouds were typically tens of meters in diameter, substantially smaller than the photon mean free path. The effects of cloud edges and cloud geometry, though no doubt important under some circumstances, have typically been calculated for extreme situations, most commonly a checkerboard pattern of clear and cloudy cubic volumes. Kobayashi (1993), for example, considered vertical excursions in

cloud top height of 1 km, which are much larger than the sub-pixel scale cloud height variations typically seen in stratiform clouds. Wetzel and Vonder Haar (1991), on the other hand, showed that reflectance biases at nadir viewing for typical stratocumulus geometries were no greater than 0.02, implying a radiance bias of $0.02/\mu_0$. Thus, although the uncertainties introduced in optical depth retrievals by nonuniform clouds may in principle be large, exhaustive simulations of retrievals from realistically shaped clouds are still outstanding. In fact, some observational evidence suggests that the effects may in practice be unimportant. Rossow (1989), for example, examined simultaneous, collocated radiance observations from two satellites with different viewing geometries, and found that the retrieved optical depths were consistent, indicating that the clouds were well represented by the plane parallel model used in his analysis.

Even if cloud internal variability and cloud geometry do not affect average retrieved optical depth significantly, uncertainties still arise in the estimates due to uncertainties in the measurement of radiance by the satellite sensor, and due to assumptions made in the radiative transfer model used to predict TOA radiance. Here I summarize the main results of Pincus et al. (1994) in which the subject is treated in detail. There are two relevant questions: to what accuracy can the average (or median) optical depth be determined in an individual scene, and to what extent can changes in average optical depth between scenes be determined?

Uncertainties in retrieved optical depth for individual pixels can be traced to uncertainties introduced by satellite radiometer discretization, by uncertainty in radiometer calibration, and by differences between the atmosphere in which the cloud finds itself and the atmosphere in my radiative transfer model. For the retrieval scheme described in §2.2.2, the absolute uncertainty in scene-averaged cloud optical depth is determined primarily by the absolute uncertainty in radiometer calibration (Pincus et al., 1994), which for the ISCCP calibrations is about 5–10% (Han et al., 1994). Figure 2-5 shows the relative uncertainty in cloud optical depth due to a 5% calibration uncertainty as a function of solar zenith angle and cloud optical depth, averaged over all azimuthal angles and over satellite viewing angles greater than 60°. As is true in general (Pincus et al., 1994), optical depth estimates are more uncertain at larger optical depths and larger solar zenith angles.

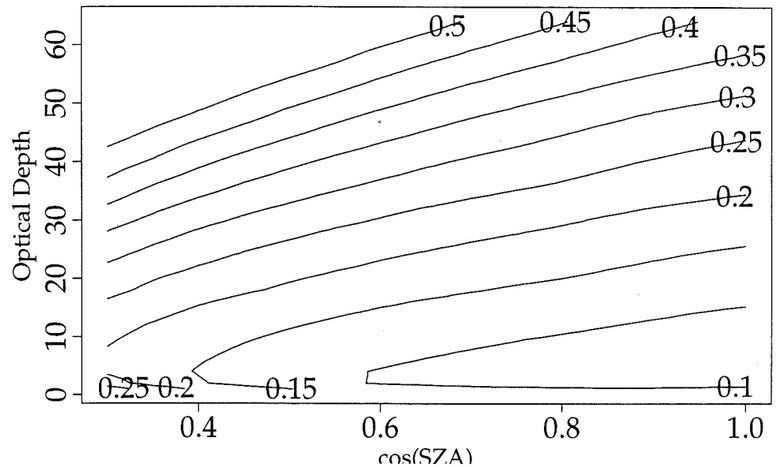

FIG 2-5. Relative uncertainty in retrieved cloud optical depth due to uncertainties in radiometer calibration. The uncertainty is averaged over all azimuthal angles and all satellite zenith angles less than 60°. This source of uncertainty dominates other sources, including uncertainties in the specification of the atmosphere used in the radiative transfer model used in the retrieval algorithm. From Pincus et al. (1994)

Despite the substantial uncertainty in the mean or median optical depth computed for a particular scene, short term temporal changes in optical depth may be detected reasonably well using the Lagrangian technique. Most error sources in the retrieval (misspecification of the forward model and absolute calibration uncertainty) affect the uncertainty in optical depth by uniformly increasing or decreasing the retrieved optical depth at all values of satellite-measured radiance. When comparing a series of measurements made using the Lagrangian technique, these errors contribute equally to every measurement in the time series, without affecting the *change* in optical depth. The only significant uncertainty remaining stems from the nonlinear mapping of radiance to optical depth caused by the absolute uncertainty in radiometer calibration. The exact value of this uncertainty depends on the distribution of radiances in the original scenes. Pincus et al. (1994) showed an example in which this uncertainty introduced an uncertainty in the change in mean optical depth between a morning and

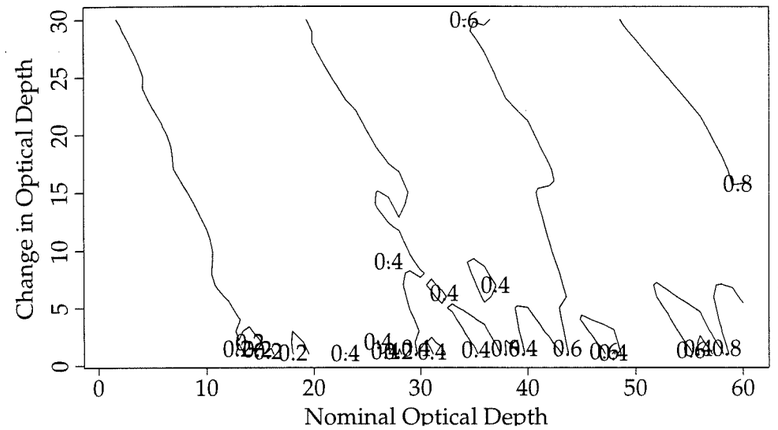

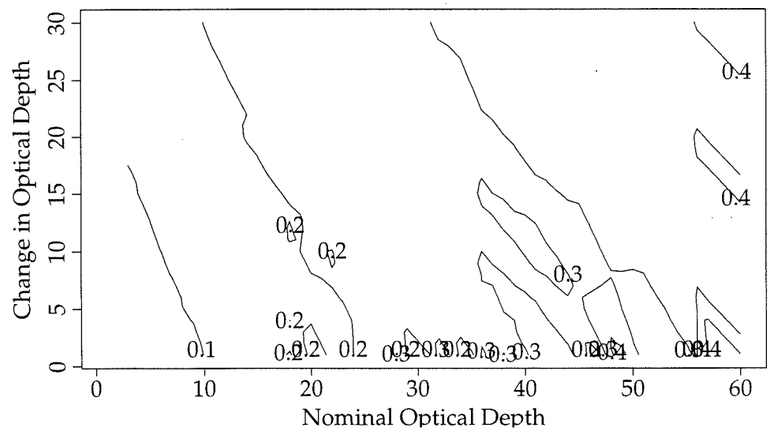

FIG 2-6. Relative uncertainty in the difference between two optical depth measurements. The optical depths are computed assuming a 5% absolute uncertainty in radiometer calibration and a perfect radiative transfer model. The upper panel assumes that all radiances have been overestimated by 5%; the lower that the radiances have been underestimated by the same amount.

afternoon scene of 15–20%. Figure 2-6 shows an another view of this result: the relative uncertainty in the difference between two optical depths retrieved with a perfect radiative transfer model and the sun and satellite directly over the cloud layer. The upper panel shows contours of the relative uncertainty as a function of the difference between two optical depth estimates and the nominal value of the lesser optical depth and computed by assuming that TOA radiance is uniformly overestimated by 5%, the lower panel assumes a uniform underestimate. It is this error which applies to measurements made with the Lagrangian technique, and for optical depths typical of marine stratocumulus clouds the uncertainty is modest. Note that the actual uncertainty in the difference between the means of two populations will differ from the uncertainty shown in Figure 2-6, since the uncertainty for a statistic derived from a population will differ from those of the derived value alone.

2.4 *Discussion*

In this chapter I have introduced a technique for observing the Lagrangian evolution of clouds in the marine boundary layer. The technique is necessarily inferential, attempting to squeeze the maximum amount of information about cloud processes from relatively few measurements. On the other hand, it allows for inexpensive, systematic studies in remote regions using existing data sets.

The technique is general, and might be applied to any problem involving stratocumulus evolution. In the next chapter, however, I will return to the questions posed in Chapter 1: to what degree do cloud microphysical processes control the evolution of cloud fraction and albedo in the marine boundary layer?

3 Observations of Stratocumulus Evolution

Chapter 1 described the physical basis for coupling between cloud microphysics and such large scale properties of stratocumulus cloud layers as cloud fraction through the mechanism of precipitation. In particular, the model of Albrecht (1989) and others related to it predict significant sensitivity of cloud fraction to the amount of drizzle produced in the boundary layer. The Lagrangian nature of marine stratocumulus evolution, however, has made this idea difficult to test observationally, and competing hypotheses suggest that the roles of various factors such as large scale subsidence, off-shore flow, increasing sea surface temperature, or thermodynamic instability may play more important roles in determining cloud fraction.

In this chapter I use the Lagrangian technique developed in Chapter 2 to test Albrecht's hypothesis, and more generally to investigate the degree to which precipitation controls cloud fraction in the FIRE region. The results indicate that the presence or absence of precipitation is by itself a poor predictor of the evolution of cloud fraction in the FIRE region. Based on an analysis of the trajectories in the initial group, I also examine the importance of the rate of change of sea surface temperature along the trajectory, and conclude that parcels moving over a rapidly increasing SST are more likely to maintain a high cloud fraction throughout the day than are parcels experiencing a slow rise in SST.

3.1 *Assessing the Role of Precipitation*

3.1.1 EXPERIMENTAL DESIGN

I investigate the role of precipitation in controlling the evolution of cloud fraction by comparing the evolution of cloud layers in the presence and absence of precipitation. Because the VIS and IR radiances reported by the VAS sensor cannot be used to assess the amount of precipitation, I use observations from other platforms to provide initial conditions (trajectory starting time and position, and a determination of presence or absence of precipitation at the starting point), then use the Lagrangian technique to observe the evolution of the parcels for some period of time. Two issues must be resolved: for how long should the evolution of the parcels be observed, and how can the initial conditions be obtained?

The time scale over which precipitation may affect cloud fraction depends on the mechanism through which the precipitation acts. Drizzle has two effects (see §1.2): (a) the direct removal of water from the boundary layer due to precipitation at the surface, and (b) the inhibition of vertical mixing due to condensation in the cloud layer and subsequent evaporation of precipitation in the subcloud layer. Direct removal can act very quickly. A drizzle rate typical of stratocumulus in the FIRE region of 1 mm day^{-1} (Austin et al., 1994b) corresponds to a change in liquid water path of 45 g m^{-2} hr^{-1}. The water lost in a single hour at these rates corresponds to a large change in typical stratocumulus liquid water paths (typically 100–150 g m^{-2}; see, for example, Cahalan et al., 1994). This implies that if the water lost due to drizzle at the surface is not replaced by fluxes of vapor from the sea surface, drizzle may cause cloud layers to thin and dissipate in a matter of a few hours. The time scale on which the inhibition of mixing acts is a more difficult question, and depends on the boundary layer dynamics. Observations and simulations of the diurnal cycle of stratocumulus (Bougeault, 1985; Turton and Nicholls, 1987; Bretherton, 1994) suggest that cloud layers which become uncoupled from the surface layer during the day often recouple during the night, allowing fluxes of water from the ocean to replenish and thicken the cloud. The evaporation of drizzle in the subcloud layer on one day might inhibit this overnight reconnection and cause the cloud to be thinner and more susceptible to patchiness and a reduction of cloud fraction on the next day.

More prosaic concerns place an upper bound on the length of time for which cloud evolution may be observed. Lengthy trajectories may leave the area for which the satellite or environmental data is available. In addition, the uncertainty in parcel position and the total amount of lateral mixing increases with time (§2.3.1). Therefore, I use the Lagrangian technique to observe cloud evolution for a day and a half, from sunrise on one day to sunset the next. After 36 hours Figure 2-2 suggests that the uncertainty in parcel position is about 250 km; this figure determines the size of the mesoscale sized regions extracted from the satellite imagery. The trajectories may be divided into three time periods: the day on which the initial conditions are obtained (day 1), the following day (day 2), and the intervening nighttime hours.

A systematic study of the role of precipitation in controlling cloud fraction requires knowledge of the microphysical state of a large number of cloud layers for use as initial conditions for the Lagrangian observational method. Space-based observations of microphysics would be ideal, since the technique allows the observation of cloud evolution from arbitrary places and times, and because the initial conditions would be derived from measurements on a similar spatial scale to the Lagrangian technique. Several kinds of measurements made from satellites seem attractive. Passive microwave sensors such as the Special Sensor Microwave Imager (SSMI) can be used to estimate precipitation based on the relative amounts of depolarization in a pair of microwave channels (Petty, 1994). These instruments, however, are not sensitive to the very small amounts of drizzle that typically fall from subtropical stratocumulus layers (J. Miletta, personal communication). Simultaneous remote sensing estimates of effective radius and cloud optical depth such as can be made with the near-infrared channels from AVHRR sensors (Han et al., 1994; Platnick and Twomey, 1994) might appear to be an appealing alternative since, in general, precipitation rate increases with drop size. Nakajima et al. (1991), however, showed that the relationship between remotely-sensed effective radius and optical depth and in situ measurements of precipitation is quite complicated, with effective radius tending to decrease with optical depth in precipitating stratocumulus. A robust, straightforward technique for diagnosing precipitation from droplet size and optical depth measurements is still outstanding.

In the absence of reliable satellite-based precipitation measurements, I use in situ aircraft measurements of cloud droplet size and concentration to determine the presence or absence of precipitation during several days during FIRE. The temporal and spatial scales of the satellite and aircraft measurements are wildly incommensurate, since the sample volume of the aircraft sensors, although integrating over large spatial scales as the aircraft flies, is minute. By using aircraft measurements to characterize precipitation, I assume that observations of precipitation by the aircraft are representative of precipitation on the spatial and temporal scales observed by the satellite (i.e. that precipitation is occurring throughout much of the mesoscale-seized image). To the extent that drizzle production is governed by the number concentration of drizzle drops this is reasonable: although Austin et al. (1994b) observed local precipitation scavenging of both cloud liquid water and droplet number, the model of

Ackerman et al. (1994) showed that relaxation times for CCN and droplet concentrations are on the order of 2-3 days to reach equilibrium.

3.1.2 AIRCRAFT OBSERVATIONS

Observations describing the presence or absence of drizzle on a number of days during FIRE come from three published accounts of in situ aircraft measurements (Albrecht, 1989; Nakajima et al., 1991; Austin et al., 1994b) and from the NCAR Electra observer notes as reported in Kloesel et al. (1988). Table 1 of Albrecht (1989) enumerated 9 soundings from 6 days during FIRE for which Albrecht had precipitation data available; he kindly communicated to me the time of each sounding. The location of each sounding is described in the aircraft flight plans detailed in Kloesel et al. (1988). I choose the earliest sounding from each day (since subsequent soundings took place within the mesoscale-sized images used by the Lagrangian technique), neglecting July 3, because the aircraft observations were made at night, and July 16, because the trajectory on this day was close to the coast and the flow onshore. One of the four remaining soundings showed no evidence of drizzle.

Nakajima et al. (1991) described contemporaneous remote sensing and in situ observations of stratocumulus cloud layers on four days during FIRE, two of which were observed by the University of Washington C-131 to be drizzling. One precipitating and one non-precipitating day overlap with Albrecht's observations. I use as the starting point for my trajectory on the two remaining days the position of the remote sensing platform (the NASA ER-2) midway through the flight leg as reported in their Table 1.

Austin et al. (1994b) described aircraft measurements of cloud microphysics and precipitation for three days during FIRE, and used the Lagrangian observational technique to examine cloud evolution during the day of the aircraft observations. Two of the days considered overlap with Albrecht (1989); I include the third day (July 14) on which precipitation was observed in and below cloud.

Summaries of the observer notes from the NCAR Electra are reported in Kloesel et al. (1988). The entries for July 5 indicate that the aircraft encountered solid but non-precipitating stratocumulus. I verified the observer notes by examining the aircraft data for the two hour time period following the first sounding (about 1753 GMT). Albrecht (1989) defined a

cloud to be precipitating if the average drizzle droplet concentration as measured by the 260X probe in a 20 second interval exceeded 10 cm^{-3} while the mean radius exceed 40 μm; during this time period the drizzle drop concentration was several orders of magnitude lower than Albrecht's threshold.

Table 3-1 summarizes the aircraft observations. The numbers in parenthesis in the first column are the sounding numbers from Table 1 of Albrecht (1989); the annotations describing "significant" precipitation, which are based on the number concentration and mean radius of drizzle-sized drops, are also Albrecht's. I refer to the trajectories starting from the observations in this table as the "drizzle trajectories". The characterization of the trajectories in terms of the presence or absence of precipitation is somewhat ambiguous, since there is no

TABLE 3-1: Trajectory Parameters for the Drizzle Study

Case	Start Date	Time (GMT)	Position	Drizzle	Source
1 (1)	June 29	1945	30.5 N 124.5 W	No	Albrecht (1989)
2 (2)	June 30	1915	31.0 N 122.0 W	Yes	Albrecht (1989)
3	July 5	1745	32.5 N 121.5 W	No	Kloesel (1988)
4 (5)	July 7	1915	31.75 N 121.5 W	Yes[a]	Albrecht (1989)
5 (7)	July 10	1615	31.5 N 120.75 W	Yes	Nakajima et. al. (1991)
6	July 11	1745	31.0 N 123.75 W	Yes[b]	Albrecht (1989)
7	July 13	1745	31.70 N 120.64 W	No	Nakajima et. al. (1991)
8	July 14	1815	31.5 N 124.2 W	Yes	Austin et. al. (1994)

a. Significant precipitation was observed 3 hours later.
b. Significant precipitation was observed during this sounding.

guarantee that precipitation was not produced at some other time along the non-precipitating trajectories. Since all the aircraft observations were made in morning, however, when the cloud are thickest and hence likeliest to produce drizzle, this possibility is minimized.

3.1.3 LAGRANGIAN TRAJECTORIES

As Table 3-1 shows, the aircraft observations characterizing precipitation in the cloud layers were made at a variety of times during the morning, ranging from 1615 to 1945 GMT (815 to 1145 local solar time). To remove the effects of the strong diurnal modulation of cloud properties, I compute the trajectory backwards in time from the time and place of each aircraft observation to a uniform time in the morning (815 PST, or 1615 GMT), then compute

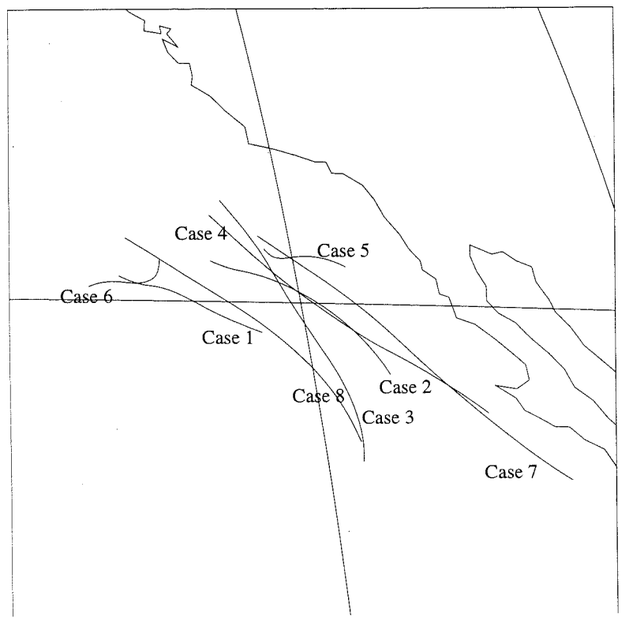

FIG 3-1. Trajectories used in the drizzle study. The map grid shows longitude 120 W and latitude 30 N; the California coastline runs diagonally across the upper-right corner of the map. All trajectories run from north to south and, with the exception of case 6, from west to east.

the parcel trajectory forward in time for 33 hours, until late afternoon (1615 PST) the next day. Environmental information and cloud parameters are reported at half-hourly intervals along each trajectory. Figure 3-1 shows the location of the air parcel trajectories used in the drizzle study.

In two instances (cases 4 and 7, beginning on July 7 and 13), the trajectory travels near Pta. Eugenia on the Baja California coast during the second day, and the clouds over land disappear. Portions of each image after 1945 GMT are affected by land in case 4, although the trajectory itself never runs onto land, so that sea surface temperature is reported for the entire period. In case 7, the images include some amount of land starting at 1515 GMT, and the trajectory runs aground at 2115 GMT. I exclude from further analysis the portion of case 4 after 1945 GMT and the portion of case 7 after 1515 GMT on the second day of evolution.

3.1.4 ENVIRONMENTAL EVOLUTION

Figure 3-2 shows the temporal evolution of wind speed and sea surface temperature for the 8 trajectories listed in Table 3-1. On the basis of their environmental histories, the trajectories may be roughly segregated into two groups: cases 1, 5, and 6, which exhibit wind speeds less than 4 m s^{-1} and changes in sea surface temperatures less than about 0.5 K over the 33 hour period, and the other five cases, which exhibit higher wind speeds and larger sea surface temperature changes. Two exceptions to this grouping are evident. Along trajectory 2, the total sea surface temperature change is only slightly greater than 0. However, Figure 3-2 shows that the parcel travelled slowly over water which initially cooled, then warmed by almost 1 K as the wind speed increased during the last 26 hours of the trajectory. The total temperature change during trajectory 4 is also small because the parcel moved during the second day into the region of upwelling cold water along the coast, but during the portion of the trajectory before the parcel passed close to the coast SST increased by about 1 K.

3.1.5 CLOUD EVOLUTION

Figure 3-3 shows the evolution of cloud fraction along each of the microphysical trajectories. Cloud fraction is determined in three ways (see §2.2.1): using the IR technique with a temperature increment of 4 K (the lines labeled 1 in Figure 3-3), and using the VIS technique

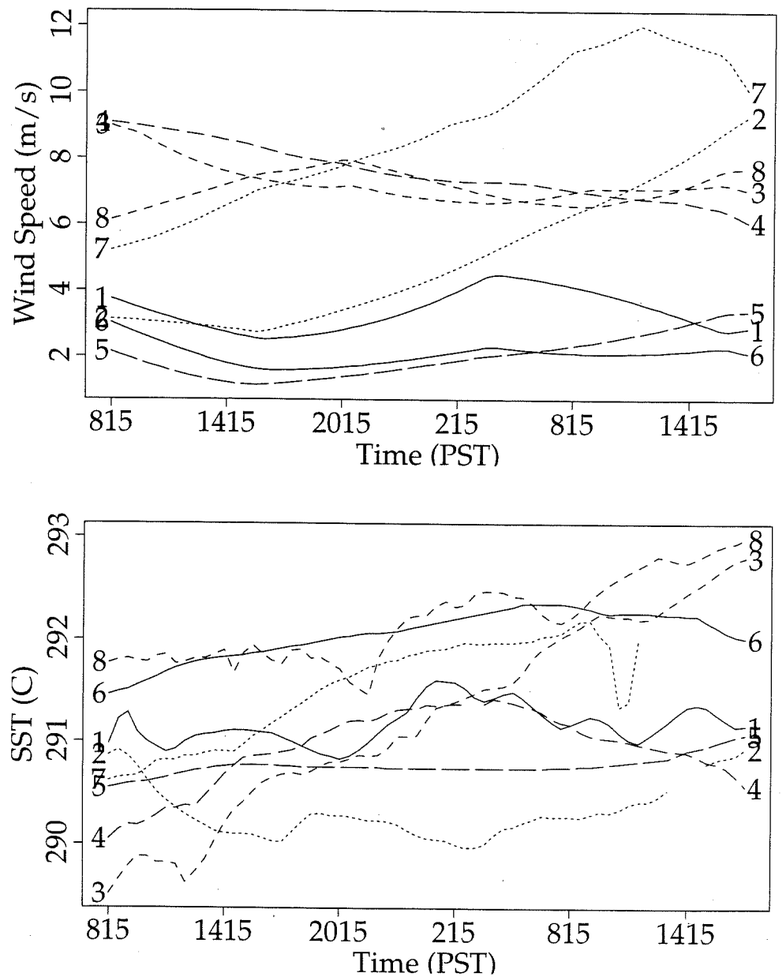

FIG 3-2. Wind speed and sea surface temperature histories for the drizzle trajectories. Each number refers to a trajectory described in Table 3-1. SST is not reported for case 7 after the trajectory nears land. Cases 1, 5, and 6 experience significantly lower wind speeds and smaller changes in sea surface temperature than do the other cases.

once with a liberal reflectance threshold of 0.08 and again with a more conservative reflectance threshold of 0.15 (the lines labelled 2 and 3, respectively). The time of the in situ observation for each trajectory is shown on the upper axis. A "P" indicates that precipitation was observed during the aircraft flight leg; an "N" indicates that no precipitation was observed.

Along all 8 trajectories, the nighttime cloud fraction is nearly 1. Observations of the diurnal cycle of stratocumulus cloud amount (Minnis et al., 1992; Rozendaal et al., 1994) consistently show that cloud fraction reaches a maximum at night. This nighttime increase in cloud fraction is a result of the key role of solar radiation in reducing cloud fraction during the day. In this set of observations even the precipitating trajectories show cloud fraction near unity at night. This implies that precipitation alone is not sufficient to cause a decrease in cloud fraction, but that it may at most act to modify the extent of daytime clearing caused by solar absorption.

During the first day of evolution, only cases 1 and 4 show cloud fractions significantly less than 1, while case 6 shows cloud fractions of around 0.8 when using the conservative VIS threshold. The low cloud fraction for case 4, however, is spurious. On this day, the aircraft flights were centered on a sharp transition between solid stratocumulus and entirely clear air (Betts and Boers, 1990). The image series includes this edge, which gradually moves out of the field of view as the clear air fills with clouds. The most significant clearing on the first day of evolution, therefore, occurs for an example in which precipitation was not observed (case 1). Only one of the five precipitating layers (case 6) becomes patchy, and the reduction in cloud fraction is small.

The evolution of cloudiness on the day following the in situ observations is more complicated. Two of the trajectories (cases 4 and 7, one of which was precipitating the day before) are strongly influenced by their proximity to the coast, and must be excluded from the analysis. In none of the remaining cases does the cloud fraction fall below 0.75. During the second day of evolution of case 5, the IR and conservative-threshold VIS cloud fractions decreased to about 0.8 during most of the afternoon, while on the second day of case 6 the cloud fraction reaches about 0.75 using the conservative VIS threshold, with both the liberal and IR cloud fractions somewhat higher. Both cases 5 and 6 were observed by aircraft to be

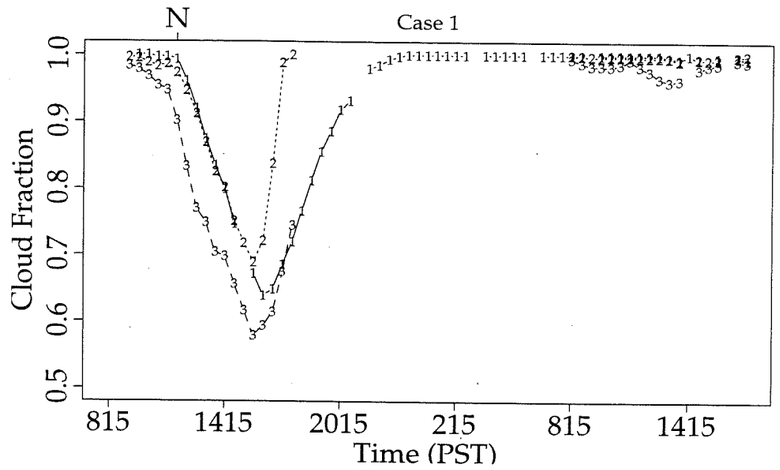

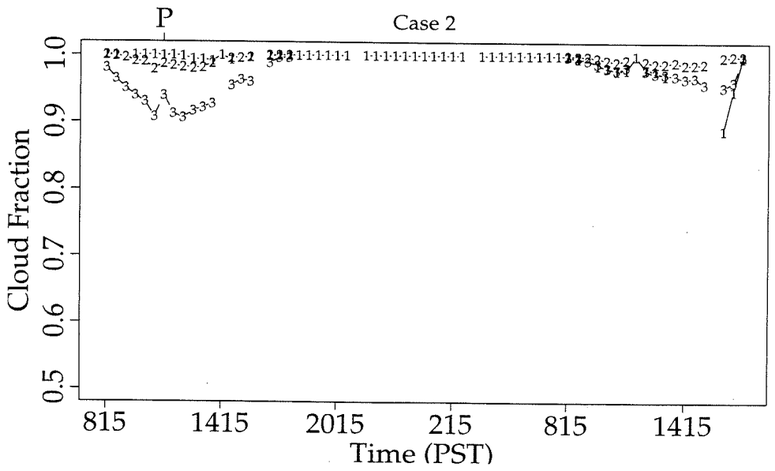

FIG 3-3. Evolution of cloud fraction along the drizzle trajectories. The lines labelled 1 denote cloud fraction computed using the IR method (see §2.2.1), lines numbered 2 and show the VIS technique with a reflectance threshold of 0.08 and 0.15 respectively. The upper and lower panels show results for 29 and 30 June.

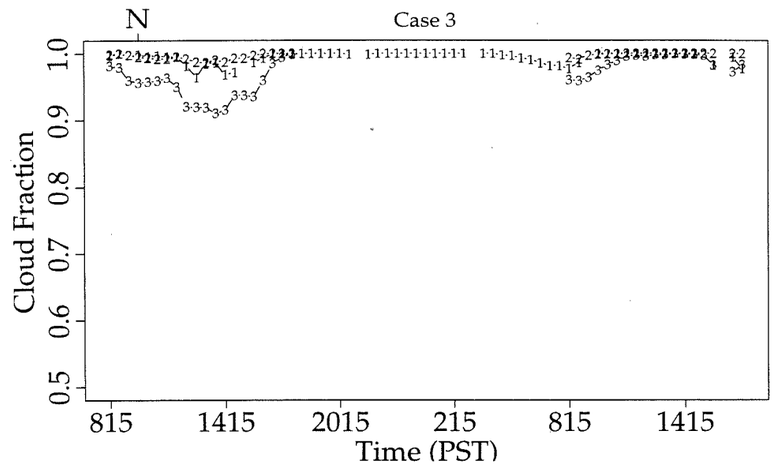

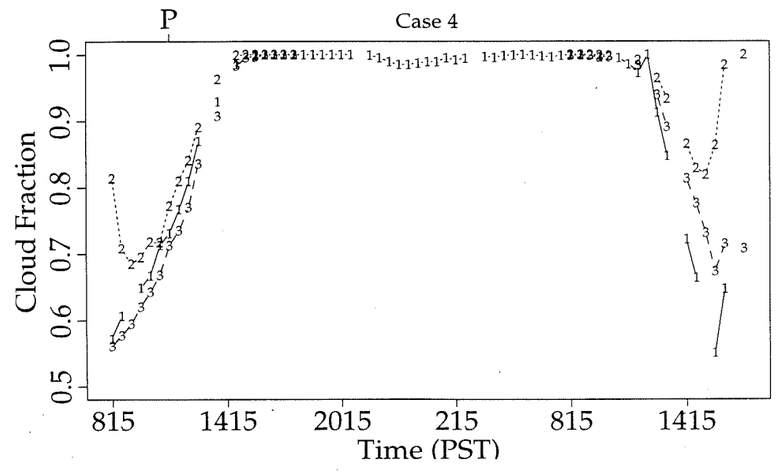

FIG 3-3, CONTINUED. The upper and lower panels show results for 5 and 7 July, respectively. On 8 July the trajectory for case 4 passed near the coast of Baja California, inducing clearing after 1145 PST.

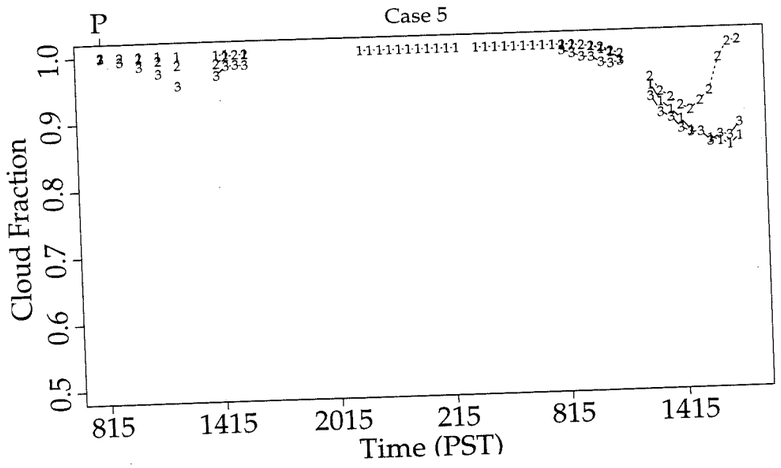

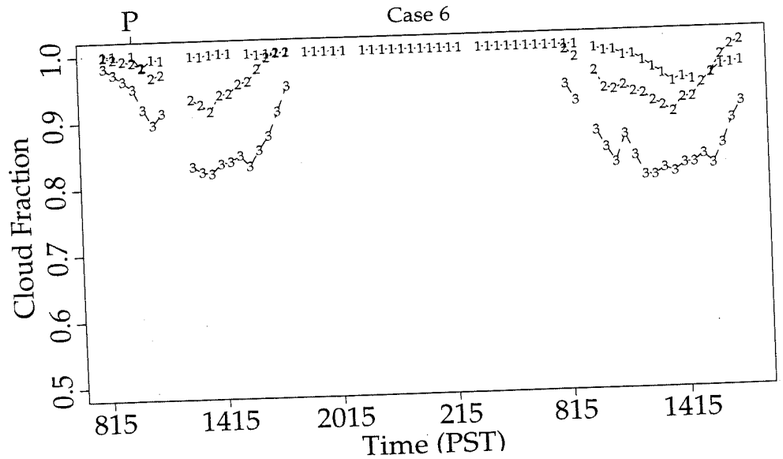

FIG 3-3, CONTINUED. Temporal evolution of cloud fraction for drizzle trajectories starting on 10 and 11 July.

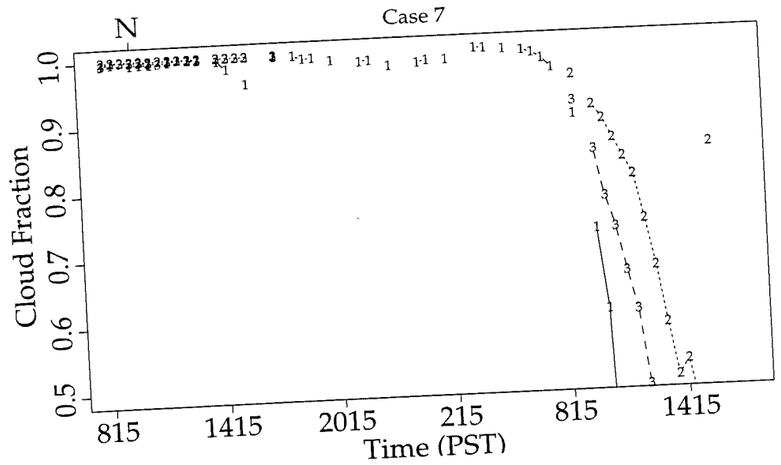

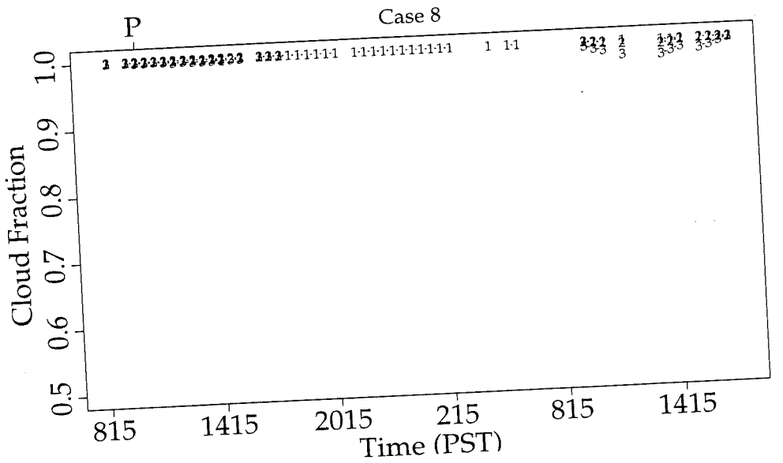

FIG 3-3, CONTINUED. Temporal evolution of cloud fraction for the microphysical trajectories starting on 13 and 14 July. The cloud fraction decreases along case 7 as the trajectory runs onshore after 715 PST on 14 July.

precipitating the day 1, as were cases 2 and 8, neither of which showed signs of decreasing cloud fraction. Neither of the nonprecipitating trajectories for which observations are available on the second day (cases 1 and 7) show a decrease in cloud fraction.

Figure 3-4 shows the temporal evolution of cloud optical depth along the drizzle trajectories. Precipitation in stratocumulus clouds is generally observed to increase with cloud geometric thickness (Nicholls and Leighton, 1986), although this dependence may be modified by changes in droplet concentration (Austin et al., 1994b). For the 8 trajectories in this study, however, optical depth is a poor predictor of the presence of precipitation: although the two optically thickest clouds on the first morning (cases 8 and 5) are indeed precipitating, the third and fourth thickest (cases 1 and 7) are not.

Of particular note is (non-precipitating) case 1, which begins on the morning of the first day of evolution relatively thick (optical depth about 13, ranked fourth of eight), but which thins dramatically and shows a marked decreases in cloud fraction by the middle of the first afternoon. The average boundary layer depth (determined using the technique described in §2.2.3, but not shown) is 1.4 km, about 200 m greater than the second deepest boundary layer and 300-400 m deeper than the depth of the majority of layers in the drizzle study. Deeper boundary layers are, in general, more likely to be decoupled than shallower layers (Wyant and Bretherton, 1992). It is therefore likely that the clearing on day 1 along this trajectory was due to solar absorption in a decoupled layer. It is unclear, however, why cloud fraction remained high during the second day of evolution.

3.1.6 SENSITIVITY OF RESULTS TO TRAJECTORY COMPUTATION

Any conclusions drawn from the observations rest on the assumption that the parcel trajectory has been computed correctly. This is unlikely to be exactly true, since the measurement network over the ocean is sparse and the analyzed wind fields are subject to some degree of uncertainty. As described in §2.3.1, however, the steadiness of the wind fields in the FIRE region make it likely that systematic rather than random errors will dominate the uncertainty in the computed trajectories. To assess the robustness of the computed cloud parameters to the computation of the parcel trajectory I perform a sensitivity test by increasing both the zonal and meridional wind components by 20%, then recomputing each trajectory and the cloud parameters derived along it.

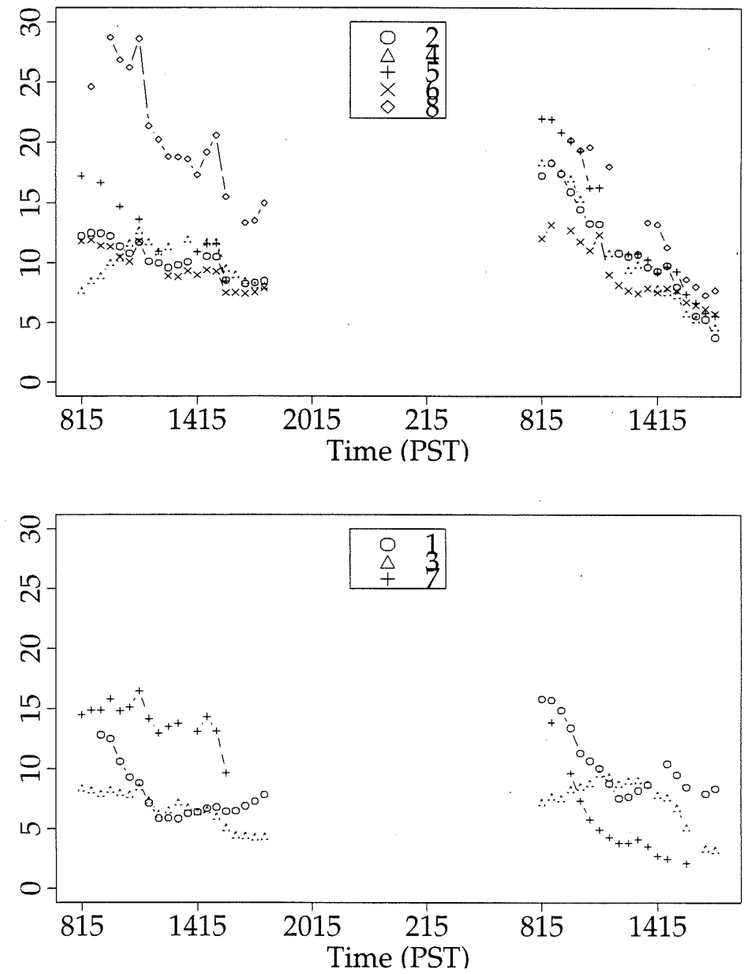

FIG 3-4. Temporal evolution of cloud optical depth along the drizzle trajectories. The upper panel shows the precipitating trajectories; the lower panel shows the non-precipitating trajectories. Although precipitation and cloud optical depth are both thought to increase with cloud thickness, cloud optical depth is a poor predictor of the presence or absence of precipitation in this data set.

The derived cloud parameters along the perturbed trajectories are, in general, quite similar to those along the nominal trajectories, indicating little sensitivity of the results to uncertainties in the wind fields. Several unsurprising differences are of note. Both case 4 and case 7 run aground earlier along the perturbed trajectories, as might be expected. Case 4 is briefly obscured by high clouds during the nighttime hours, while case 6 shows a more dramatic reduction in cloud fraction on day 2. The discussion in the next section, however, applies equally well to the perturbed and the nominal trajectories.

3.1.7 DISCUSSION

In summary, the observations of the evolution of cloud fraction on one-to-two day time scales in the FIRE region presented here do not support the hypothesis that boundary layer cloud fraction is sensitive to precipitation. The direct removal of liquid water by precipitation appears to be unimportant: on the first day of evolution, cloud fraction decreases from unity in only two cases, only one of which is precipitating. This implies that water removed from the boundary layer by precipitation is replenished by fluxes of vapor from the surface. Indeed, aircraft have observed this replacement in several case studies during FIRE (Paluch and Lenschow, 1991; Austin et al., 1994b). Neither does stabilization of the subcloud layer seem to be a key determinant of cloud fraction. On the second day, cloud fraction decreases from 1 to about 0.8 in two examples, both of which were precipitating. On the other hand, two additional precipitating cases (in addition to the two nonprecipitating cases) showed no sign of breakup.

Of the eight drizzle trajectories, three (cases 1, 5, and 6, including one nonprecipitating example) show some decrease in cloud fraction along the trajectory. I noted in §3.1.4 that these three trajectories are alike in that they experience a slower rise in sea surface temperature than the other examples in the study. Boundary layers experiencing rapid changes in SST have higher surface fluxes of heat and moisture (Schubert et al., 1979b), since the lag between the layer values and the surface value is larger. Is it possible that the rate of change of SST is the primary determinant of cloud fraction?

3.2 *Assessing the Role of Sea Surface Temperature Changes*

3.2.1 EXPERIMENTAL DESIGN

To evaluate the suggestion made in §3.1.7 that the time rate of change of sea surface temperature plays a dominant role in controlling the evolution cloud fraction, I compare the evolution of cloud fraction along trajectories which experience a rapid rise in SST with the evolution of cloud fraction along trajectories in which SST changes little. I use the same basic experimental design as in §3.1.1. Because an initial condition is not required, however, the starting times and locations for the trajectories may be chosen arbitrarily.

I compute parcel trajectories for 33 hours forward in time from two positions (35 N, 125 W and 35 N, 127.5 W) beginning at 0815 PST for each of the 21 days during FIRE. These locations are far enough apart that the trajectories are independent (in the sense that the images don't overlap) but most 33 hour trajectories begun from these two starting points remain in the observation region.Trajectories beginning further north are more strongly influenced by synoptic events, while trajectories beginning further south tend to leave the region in which data are available.

From the 42 parcel trajectories I choose two small groups: those trajectories along which the sea surface temperature changes by less than 0.5 K day^{-1} (which I refer to as the "slow" trajectories), and those which exhibit a change in SST of greater than 3 K day^{-1} (the "fast" trajectories). The 14 selected trajectories, their starting dates, and the total change in SST along each trajectory are listed in Table 3-2. Because the observations have already been stratified on the basis of their environmental histories, I forego any discussion of the environmental evolution of individual examples.

3.2.2 CLOUD EVOLUTION

I evaluate cloud fraction along each trajectory using the techniques described in §3.1.5. Figure 3-5 shows the minimum cloud fraction reported by any of the three methods on the first (upper panel) and second (lower panel) days of evolution as a function of the sea surface temperature change experienced along the trajectory. No relationship exists between minimum cloud fraction and rate of change of SST during the first afternoon, but during the second day of evolution seven of the nine "slow" trajectories exhibit cloud fractions less than

TABLE 3-2: Initial Conditions and SST Change for the SST Trajectories

	Rapidly Increasing SST		Slowly Increasing SST	
Start Location	Start Date	Δ SST	Start Date	Δ SST
35 N, 127.5 W	July 5	6.08	June 30	-2.22
	July 6	4.93	July 1	-1.62
	July 4	4.89	July 18	-0.89
	July 7	4.85	July 2	0.09
	July 16	4.13	July 14	0.45
35 N, 125 W	July 5	4.32	July 19	0.85
			June 29	0.34
			July 2	0.36

0.6, while four of the six "fast" trajectories show cloud fractions in excess of than 0.85. This is consistent with climatological observations of the Lagrangian nature of stratocumulus evolution: Klein et al. (1994) noted that anomalies in cloud fraction were best correlated with SST anomalies one day upstream.

Two exceptions appear in each group. Among the "fast" trajectories, the examples beginning on July 4 and 7 both exhibit relatively low minimum cloud fraction (about 0.6) during the second day. Inspection of the image series for July 4 shows that the cloud field along this trajectory consists of open cells (Agee, 1987), a regular geometric arrangement of thin cloud bands surrounding regions of clear air. This cloud type is rare in the FIRE region, being more commonly observed where convection is driven primarily by surface heating (Agee, 1984). Although the cloud fraction along the trajectory beginning on July 7 does not change from day 1 to day 2, the cloud type undergoes a dramatic change, from thin, patchy clouds to a solid clouds layer with an entirely clear region intruding into the cloud deck. The existing clouds thicken quite a bit: average morning (815-1215 PST) optical depth on day 1 is 6.6, which increases to 9.8 on day 2. The cause of the clear region is unclear, but the thickening of the cloud is consistent with the high cloud fraction and optically thick clouds exhibited by the rest of the cases in this group.

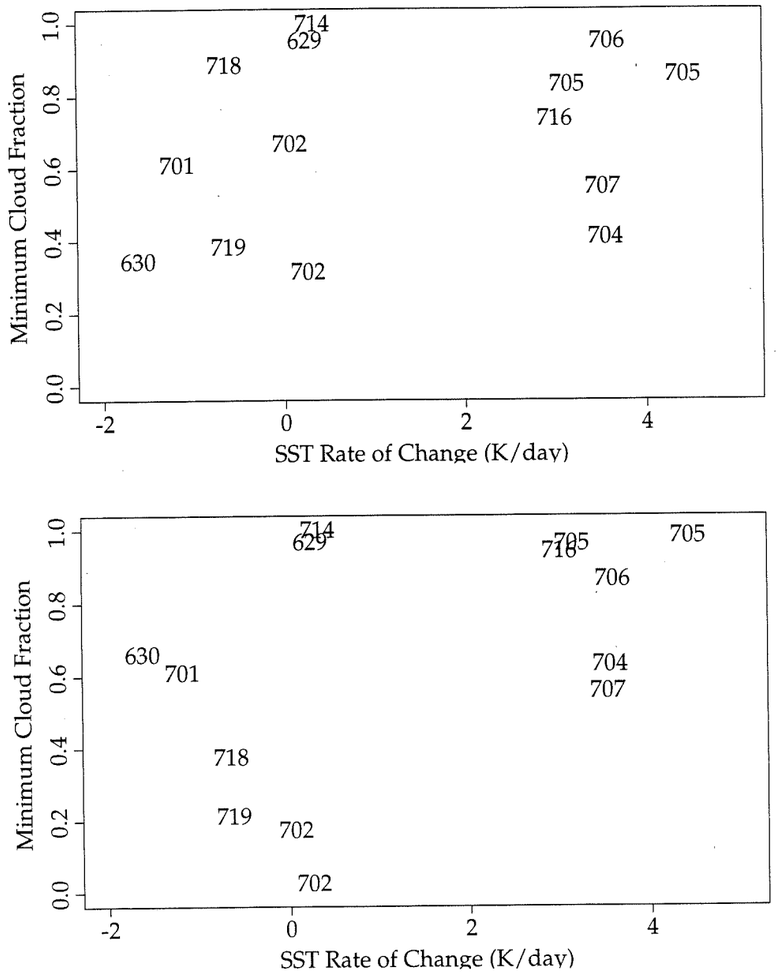

FIG 3-5. Minimum cloud fraction compared to the rate of change in sea surface temperature. The upper panel shows the minimum cloud fraction as observed during the first 24 hours of evolution (including the first day, when cloud fractions are lowest); the lower panel shows the results for the last 9 hours, including the second day. Numbers indicate the starting month and day of the trajectory.

Although the trajectories beginning on June 29 and July 14 experienced small changes in SST, cloud fraction remained high along both trajectories for the duration of the 33 hour observational period. Since daytime reductions in cloud fraction are the results of solar absorption, it may be possible for clouds to survive throughout a day under circumstances in which they would normally break up if they are quite thick at sunrise. Figure 3-6 shows the minimum cloud fraction observed on the first and second days of evolution as a function of average morning cloud optical depth on the each day. The two trajectories along which cloud fraction remains high (June 29 and July 14) are indeed the two trajectories with the highest morning cloud optical depth on both day 1 and day 2, although a more comprehensive relationship between morning optical depth and minimum cloud fraction does not seem warranted.

3.3 *What do the Observations Suggest?*

Several tentative conclusions can be drawn from the observations presented in §3.1 and §3.2. First, the observations do not support the hypothesis that precipitation plays a significant role in controlling boundary layer cloud fraction in the FIRE region on one-to-two day time scales. It seems likely instead that the effects of precipitation are masked by the much more important role of solar insolation in determining cloud fraction. Secondly, the rate of change of sea surface temperature appears to be a fairly good predictor of the evolution of cloud fraction, especially on the second day of evolution. If cloud optical depth is high (greater than about 10) early in the day, however, cloud fraction can remain high even if SST is not increasing rapidly.

The observations raise several important questions. Most fundamentally, why does cloud fraction diminish along trajectories with slowly changing sea surface temperature? Although it is clear that surface fluxes of heat and moisture in the boundary layer decrease as the rate of change of SST decreases, the exact mechanisms by which this reduction in surface flux leads to a decrease in cloud fraction have not been elucidated. In the next chapter, I use a detailed numerical model of the marine boundary layer to address this question.

The observations in §3.2 also suggest that clouds that are quite thick at the beginning of the day (with optical depth greater than 10–15) maintain a high cloud fraction even under cir-

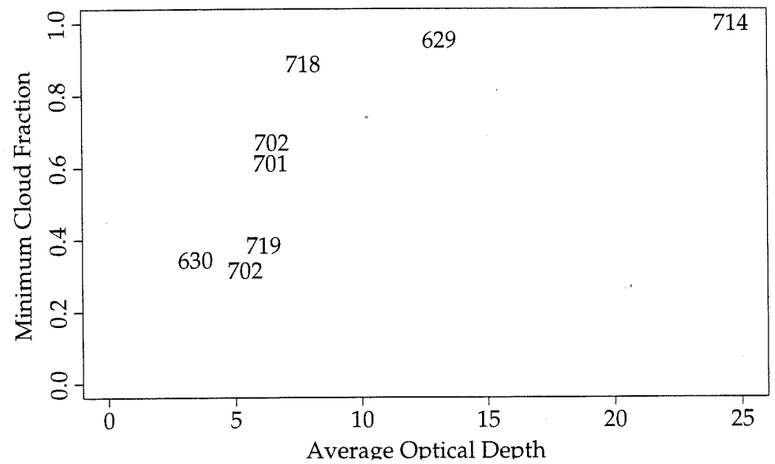

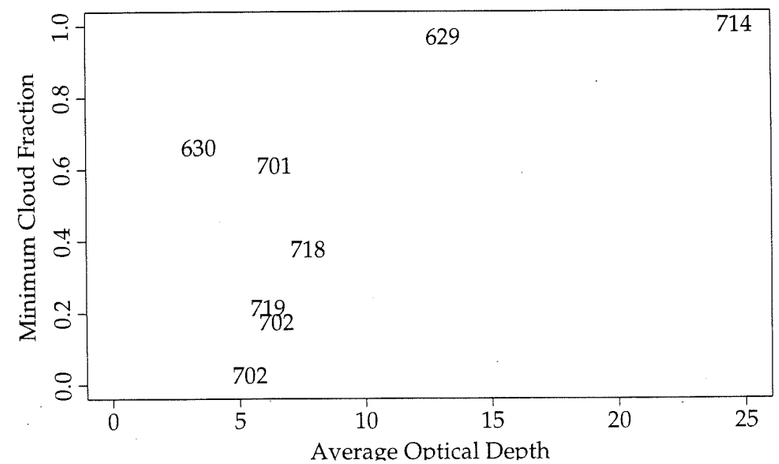

FIG 3-6. Minimum cloud fraction as a function of average morning optical depth on day 1. The upper panel shows the minimum cloud fraction during the first 24 hours of evolution; the lower panel shows the results for the second 9 hours (including the second day). Only the "slow" trajectories are shown.

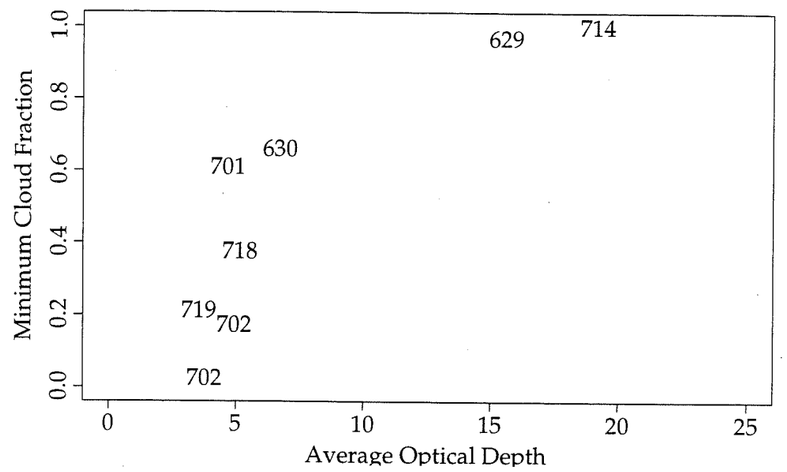

FIG 3-6, CONTINUED. Minimum cloud fraction as a function of average morning optical depth on day 2.

cumstances in which cloud fraction would otherwise decrease. The question then arises: what causes clouds to become thicker in the first place? The model presented in Chapter 5 suggests that high values of droplet number concentration should be associated with thicker clouds. In the absence of in situ observations, however, this possibility can not be tested.

4 Simulations of Stratocumulus Evolution

The observations described in Chapter 3 suggest three key physical points: that stratocumulus are likely to dissipate only during the daytime; that precipitation alone is not likely to be sufficient to cause cloud breakup; and that the rate of change of sea surface temperature is a major determinant of daytime clearing. In this chapter I use a detailed numerical model of marine stratocumulus to test these suggestions, and try to discern why they might hold.

Mathematical models of marine stratocumulus fall into three broad categories of increasing complexity. Bulk models, including mixed layer (Lilly, 1968; Schubert et al., 1979a) and mean gradient models (Albrecht et al., 1979; Albrecht, 1984), make assumptions about the thermodynamic structure of the boundary layer and characterize the layer in terms of some small number of parameters, then diagnose the temporal evolution of cloud properties based on budget equations for the parameters. One dimensional turbulence closure models (Bougeault, 1985; Chen and Cotton, 1987; Bretherton, 1994) are formulated by expanding each quantity in the equations of motion and thermodynamics in terms of its mean value and some perturbation. The models are closed by parameterizing the moments above some chosen order. These one dimensional models can develop arbitrary structure in the vertical dimension, but assume horizontal homogeneity. Large eddy simulations (e.g. Moeng et al., 1992) explicitly represent motion in two or three dimensions. The equations of motion and conservation of energy and water are discretized in space and time, and transports on the subgrid scale are parameterized. The equations are then solved on a grid. Turbulence closure models extended to two or three dimensions may be thought of as large eddy simulations with elaborate subgrid scale parameterizations.

An accurate model of the effects of precipitation on cloud fraction must faithfully reproduce two key phenomena caused by the evaporation of precipitation: the inhibition of mixing due to relative cooling of the subcloud layer, and the promotion of cumulus convection in the lowest part of the boundary layer. The first requirement generally rules out the use of bulk models, while the second argues against the use of one dimensional turbulence closure models, which cannot represent the different properties of saturated updrafts and unsaturated downdrafts in a single column. Investigation of this question therefore requires the use of a large eddy simulation. Fortunately, one is available to me.

4.1 *Model Description:* HUSCI

HUSCI (Huge and Unmanageable Stratocumulus Integrator) is a large eddy simulation developed at the University of Washington by Chris Bretherton, Matt Wyant, Hugh Rand, and David Stevens. The model solves the anelastic equations of motion and conservation equations for three thermodynamic quantities (the liquid water potential temperature θ_l (K), the total water mixing ratio q_t (kg-water/kg-air), and the rainwater mixing ratio q_r) on a rectangular grid. Longwave and shortwave radiative fluxes are computed using two stream models which incorporate variable emissivity for the longwave radiation and three absorbing and scattering spectral bands in the shortwave (Bretherton, 1994). Cloud microphysics is treated by partitioning the liquid water content into separate cloud and rain water categories. Water moves from the former category to the latter through the parameterized processes of autoconversion and accretion. The model may be run with a two or three dimensional domain, and can simulate the Lagrangian evolution of the boundary layer by allowing the imposed external environmental conditions (large scale velocity, sea surface temperature, subsidence, and upper air sounding) to change with time. A detailed description of the model will be found in the Ph.D. dissertations of Matt Wyant and Hugh Rand.

All of the simulations described here, as well as the modifications to the model and the analysis tools described below, were performed by Matt Wyant. I owe Matt an enormous debt for his generous collaboration both in performing the bulk of this work and for many fruitful and enlightening discussion about the results. In the remainder of this chapter I use the first person plural to indicate the cooperative nature of this work.

4.1.1 MODIFICATIONS TO HUSCI

HUSCI was modified in two ways for these simulations. One change concerns the autoconversion parameterization, which determines the rate at which small cloud droplets collide with each other to produce embryonic raindrops in each grid volume at each timestep. For the runs reported here, the autoconversion rate was computed using a slightly modified version of the parameterization of Baker (1993):

$$\dot{q}_r(\text{auto}) = k_r C_1 N r^4 W(r) q_c \qquad (4\text{-}1)$$

where r is the characteristic droplet radius in the volume, q_c the cloud liquid water mixing ratio, and the constants $k_r = 0.55\,\pi \times 1.2 \times 10^{-8}$ m^{-1} s^{-1} and $C_1 = 0.1$ are taken from Baker (1993). The radius r is computed by assuming that q_c is divided into N identical droplets per unit volume, which implies that $\dot{q}_r(\text{auto}) \propto N^{-1/3} q_c^{7/3}$. The weighting function $W(r)$ was specified by Baker as the Heaviside step function $H(r\text{-}10\ \mu\text{m})$; in order to eliminate abrupt jumps in the autoconversion rate we specify instead $W(r) = (r/10\ \mu\text{m})^3$ for $r < 10\ \mu$m and $W(r) = 1$ for $r > 10\ \mu$m. This parameterization agrees well with explicit calculations of autoconversion made by numerically solving the stochastic collection equation (Austin et al., 1994b), although it predicts relatively small autoconversion rates compared to other parameterizations (for example, Chen and Cotton, 1987).

The temporal evolution of cloud fraction provides a key piece of information for the studies in Chapter 3, but it is not exactly clear how this parameter ought to be evaluated from the model output. A quantity termed *area cloud fraction* may be computed by counting up the number of columns containing any liquid water and dividing this number by the total number of columns in the model domain. The cloud fraction algorithm described in §2.2.1 and used in the observational studies, however, is based on a reflectance measurement made at the top of the atmosphere, which will not be the same as the area cloud fraction if some columns contain very small amounts of liquid water. In order to simulate the satellite observations, a *satellite cloud fraction* is derived by computing the optical depth of each column using (1-3) and (1-4), then computing the reflectance of each column using the two-stream approximation (Meador and Weaver, 1980) expression for albedo (5-11). The satellite cloud fraction is then defined as the number of columns whose albedo exceeds 0.12 (optical depth 1.8) divided by the total number of columns. Differences between the two measures of cloud fraction indicate the presence of very thin clouds.

4.2 *Experimental Design*

We test each of the three hypotheses in turn by considering the temporal evolution of model predicted quantities in three pairs of runs. The model does not accurately represent all of the processes causing precipitation and so predicts unrealistically low rain rates; we examine the sensitivity of the model results to this error in a fourth pair of runs. In all runs the model is configured as a two dimensional simulation set in a Lagrangian frame of refer-

ence in which the sea surface temperature increases with time. The model domain spans 3.5 km in the horizontal and 2.2 km in the vertical with a grid size of 50 × 25 m. The radiative parameters are set to correspond to latitude 40 N on July 1, which yields a diurnally averaged solar zenith angle of 69° ($\mu_0 = 0.36$).

To examine the relative importance of solar radiation and precipitation in promoting daytime clearing, we consider two sets of runs. In one pair (the "D" runs) the solar radiation varies with time of day; in the other (the "C" runs) the solar radiation is constant at the average solar zenith angle. To assess the role of microphysics in controlling cloud evolution, both the C and D runs are performed twice, once with droplet concentrations of 50 cm^{-3}, and once with droplet concentrations of 400 cm^{-3}. In all four of these runs the sea surface temperature begins at 285 K and increases by 1.5 K day^{-1}, and cloud evolution is computed for eight days. In all cases the model is initialized with a mixed layer sounding with $\theta_l = 285$ K, $q_t = 7.2$ g kg^{-1}, and the inversion height $z_i = 600$ m. The jumps in θ_l and q_t at the inversion are initially set to 10.5 K and -3.2 g kg; θ_l increases above the initial inversion height at a lapse rate of 1.68 K km^{-1}, while q_t remains constant with height at 4 g km^{-1}. The vertical profiles of θ_l and q_t in the free troposphere do not vary with time. Large scale divergence is fixed at $D = 3 \times 10^{-6}$ s^{-1}.

Models of precipitation formation in stratocumulus clouds linking turbulence and microphysical processes (Nicholls, 1987; Baker, 1993; Austin et al., 1994b) indicate that the recirculation by turbulent mixing of a small number of relatively large drops is responsible for a substantial fraction of the precipitation falling from cloud base. HUSCI lacks an explicit representation of this process, and so predicts rain rates lower by a factor of roughly five than a model using the same autoconversion parameterization but incorporating a treatment of very small scale turbulent mixing (Baker, 1993). We examine the sensitivity to this underestimation by arbitrarily increasing the constant C_1 in the autoconversion parameterization to 0.5 and rerunning the C50 and D50 simulations. These runs, denoted "E" to indicate enhanced autoconversion, produce realistic rain rates at the expense of requiring excessive autoconversion.

To examine the importance of the rate of change of sea surface temperature in controlling cloud fraction we consider two runs which differ primarily in the rate of change of sea surface temperature increase. Run "FAST" begins with the same initial sounding as the mixed layer sounding discussed above and sea surface temperature of 285 K, which increases at 3 K day^{-1}. Run "SLOW" begins with a sea surface temperature of 291 K, which increases at 0.5 K day^{-1}. This run is initialized by taking the state of run C50 at the point in its evolution where SST = 291 K. For both runs the droplet concentration is 50 cm^{-3} and the solar radiation varies diurnally. Integration is carried out for four days. The model runs are summarized in Table 4-1.

TABLE 4-1: HUSCI Large Eddy Simulation Parameters

Run	Droplet Number (cm^{-3})	SST at Start (K)	Rate of Change of SST (K day^{-1})	Diurnal Cycle Solar Radiation	Autoconversion Constant C_1
C50	50	285	1.5	No	0.1
C400	400	285	1.5	No	0.1
D50	50	285	1.5	Yes	0.1
D400	400	285	1.5	Yes	0.1
C50E	50	285	1.5	No	0.5
D50E	50	285	1.5	Yes	0.5
SLOW	50	291	0.5	Yes	0.1
FAST	50	285	3.0	Yes	0.1

4.3 *Model Results: Microphysics and Solar Absorption*

4.3.1 DIURNALLY AVERAGED RADIATION

Figure 4-1 shows the temporal evolution of horizontally averaged vertical structure in q_c and the square of the perturbation vertical velocity $\overline{w'^2}$ during model run C50 (N = 50 cm^{-3}; diurnally averaged radiation). (In these plots time runs along the horizontal axis, height along the vertical axis, and darker shades of gray indicate larger values of the represented quantity.) The boundary layer is initialized as a well mixed layer 600 m deep.During the

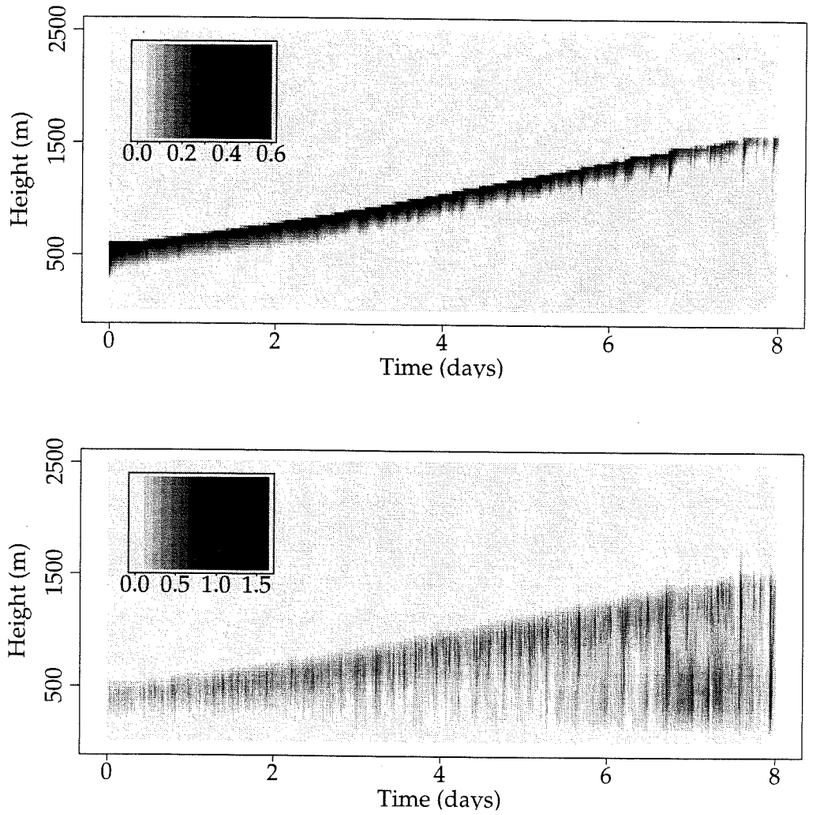

FIG 4-1. Vertical structure during HUSCI model run C50 (diurnally averaged radiation, droplet concentration 50 cm^{-3}). The upper panel shows horizontally averaged cloud liquid water q_c, the lower panel the square of the perturbation vertical velocity $\overline{w'^2}$, which indicates the degree of vertical mixing and the amount of turbulence. These density plots show time running along the lower axis and height along the vertical axis; darker shades indicate higher values. Quantities are reported every 15 minutes. Intermittent bursts of cumulus convection are responsible for the brief mixing episodes and momentarily lowered cloud base beginning after five days of evolution.

first 6 hours of evolution the model adjusts to the imposed external conditions. The boundary layer deepens with time as entrainment exceeds subsidence. Episodes of cumulus convection are evident in both q_c (as increases in cloud liquid water and a lowering of cloud base) and $\overline{w'^2}$ (as strong vertical motion reaching nearly to the surface). The stratiform layer thins and the cumulus convection becomes more intense during the last three days of the run.

Figure 4-2 shows the temporal evolution of two measures of decoupling: the absolute value of the difference between the average values of q_t in the surface layer (75 m above the ocean surface) and the cloud layer (75 m below the horizontally averaged inversion height) and the same quantity for θ_l. The layer remains nearly well-mixed for the first two and a half days of evolution, then shows increasing amounts of decoupling for the rest of the run. Short bursts of cumulus convection, visible in Figure 4-1, appear here as brief decreases in the decoupling measures.

Figure 4-3 shows domain-averaged precipitation rate and cloud fraction derived from run C50, averaged in time to 1 hour intervals. The cloud layer is not particularly thick (about

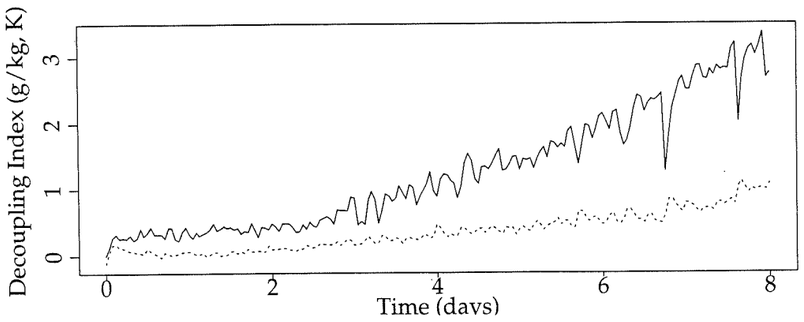

FIG 4-2. Temporal evolution of two measures of decoupling during run C50. The solid line shows the domain-averaged absolute value of the difference in q_t between the surface and cloud layers; the dashed line shows the difference in θ_l. Decoupling is negligible for the first 60 hours of evolution, then increases quickly. Rapid, short term decreases in the decoupling measures indicate cumulus convection.

200-250 m) and does not produce much precipitation: average subcloud precipitation rates (the dashed line) are about 0.1 mm day^{-1}, with cumulus convection producing brief episodes as large as three times this value. (The precipitation rates below the cumulus clouds themselves are, of course, much higher, but the are masked by the areal averaging in the figure.) Very little of this already small amount of precipitation reaches the surface (solid line). As might have been guessed from Figure 4-1, area cloud fraction remains near unity until the final day of the simulation, when it drops to about 0.75. After the fifth day of evolution, however, the cloud layer is thin enough that the satellite cloud fraction drops well below unity.

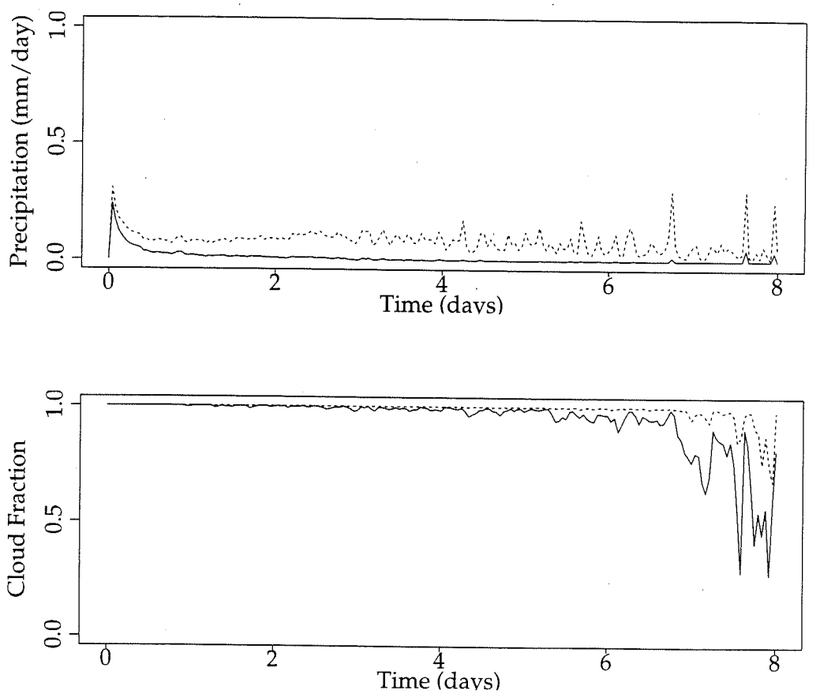

FIG 4-3. Domain averaged precipitation rate and cloud fraction during run C50. The upper panel shows the precipitation flux at the surface (solid line) and at cloud base (dashed line), the lower panel the reflectance threshold based satellite cloud fraction (solid line) and the cloud area fraction (dashed line). The moderately thick cloud produces, on average, very small amounts of precipitation, almost none of which reaches the ground. The clouds become thin enough for the satellite cloud fraction to decrease after six and a half days of evolution, but cloud area fraction remains near one until the last hours of the simulation.

Figure 4-4 shows the precipitation, cloud fraction, and decoupling histories derived from model run C400, which is identical to C50 except that the droplet concentration is increased to 400 cm^{-3}. Since the thin clouds in run C50 do not precipitate significantly, there is almost no surface flux of precipitation, and the increase in droplet concentration between run C50 and C400 has little effect on this already small flux, even though the subcloud drizzle flux is reduced by a factor of about 4 in run C400 relative to run C50. It is not surprising, therefore, that the temporal evolution of cloud fraction and decoupling are almost identical in the two runs.

Figure 4-5 shows the temporal evolution of the decoupling measures, precipitation fluxes, and cloud fraction in model run C50E (enhanced autoconversion). Precipitation fluxes are three to five times larger than in run C50, and are now in better agreement with both observations of rain rate in the FIRE region (Austin et al., 1994b) and with models treating the growth of raindrops in a turbulent environment (Baker, 1993). The degree of decoupling is not substantially affected by the increased rainfall. Intermittent cumulus convection causes large, rapid variations in the precipitation fluxes, and there is substantial evaporation in the subcloud layer. The clouds are somewhat thinner than in run C50, as is clear from the slightly earlier and larger decrease in satellite cloud fraction. In general, however, cloud fraction remains high throughout the run.

Figure 4-6 compares the domain averaged cloud thickness and the maximum cloud liquid water content in runs C50, C400 and C50E. Some of the short-term variations in h are indicative of cumulus convection of varying strength; some of the variation is also due to the model discretization of cloud thickness. In Chapter 5 I present a simple model linking cloud thickness, precipitation, and droplet number concentration in the marine boundary layer. That model, which employs a different precipitation parameterization, predicts a strong sensitivity of cloud thickness to N. The cloud thickness predicted by HUSC1 exhibit very

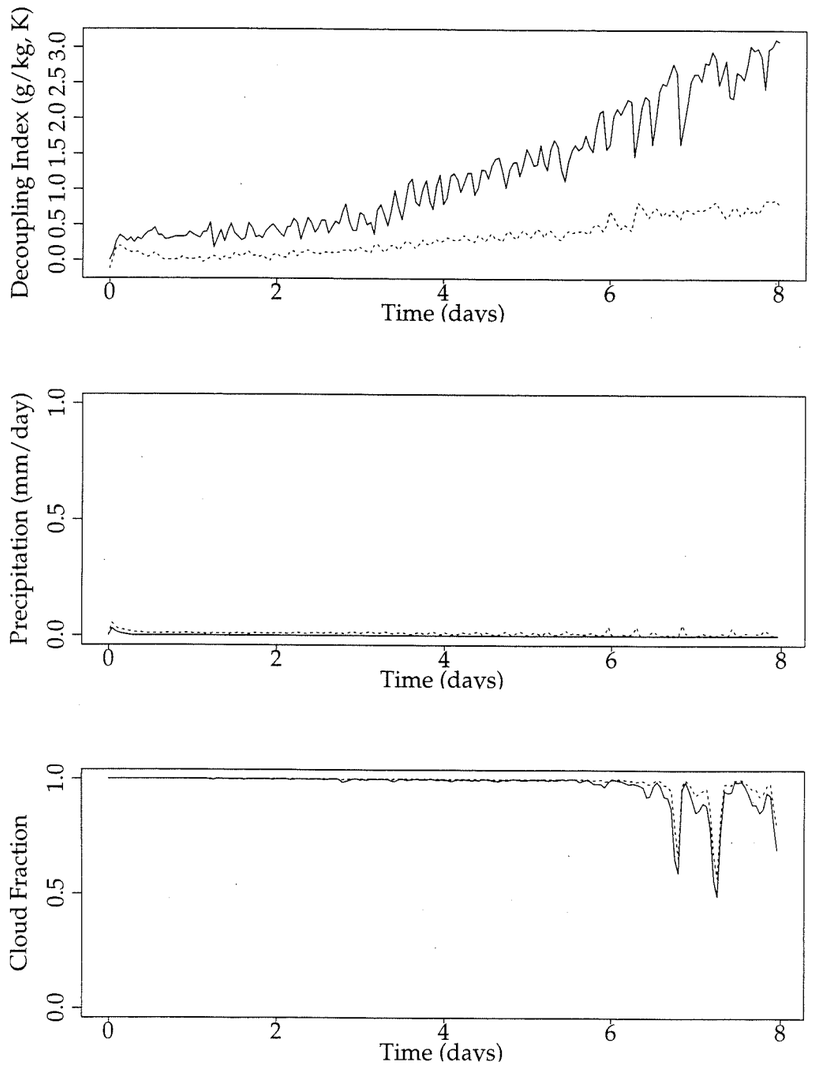

FIG 4-4. Domain averaged decoupling history, precipitation rate and cloud fraction for run C400 (droplet concentration 400 cm^{-3}). Precipitation fluxes are quite small in run C50, so that the increased droplet concentration here has little effect on cloud fraction.

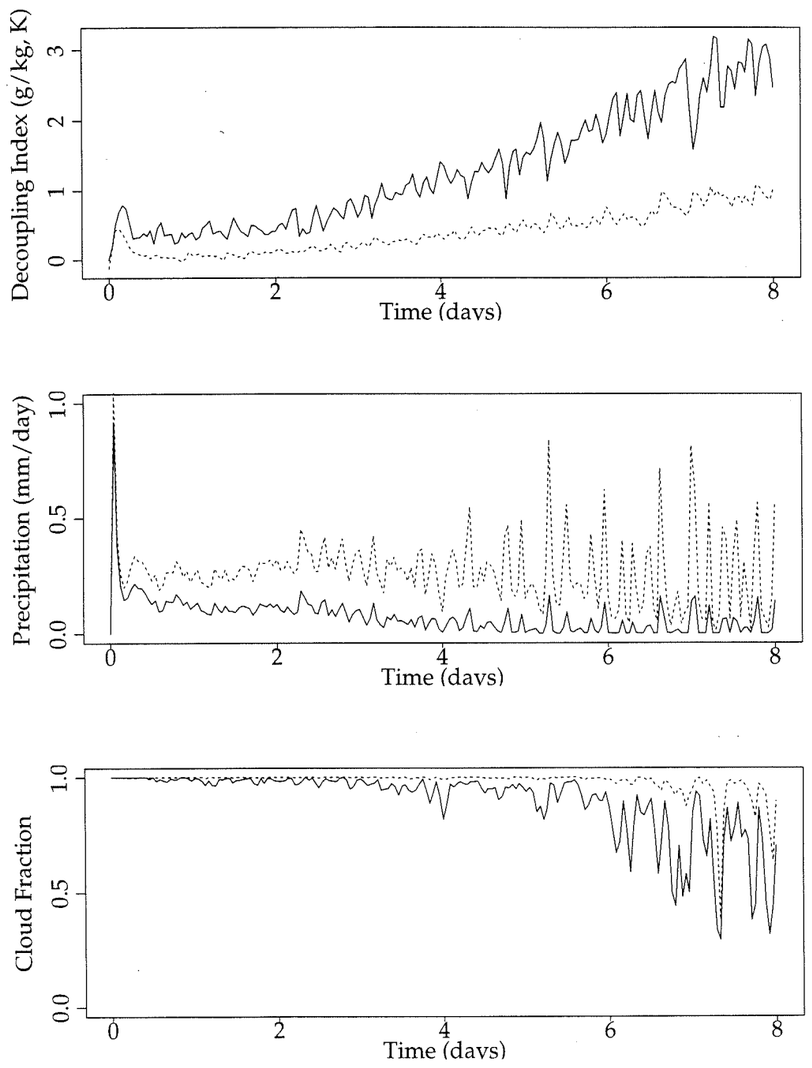

FIG 4-5. Decoupling history, precipitation rate and cloud fraction for run C50E (enhanced autoconversion). Precipitation fluxes are in better agreement with observations and models, but cloud fraction remains high throughout the run.

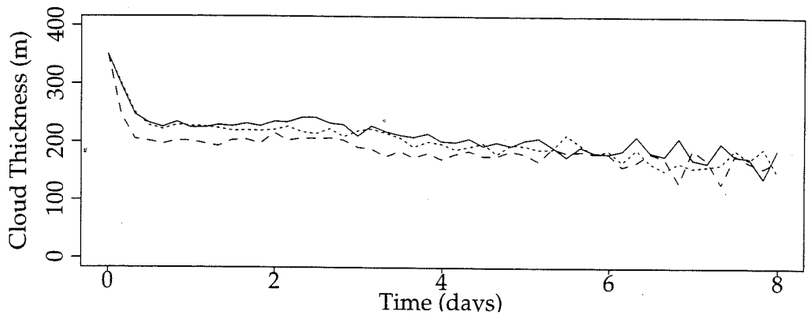

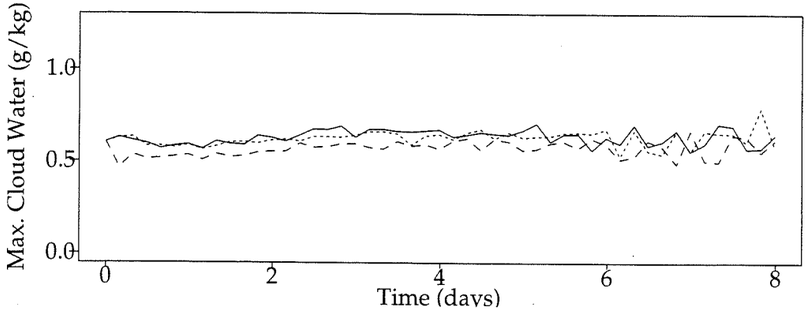

FIG 4-6. Comparison of domain averaged cloud thickness and maximum cloud liquid water content in runs C50, C400, and C50E. The results from C50 are shown with solid lines; C400 with a short dashed line, and C50E with a long dash.

little sensitivity to droplet number concentration because the precipitation rates computed are low regardless of N. When precipitation rates are higher (as in run C50E) both maximum cloud liquid water contents and cloud thicknesses predicted by HUSCI do indeed decrease.

4.3.2 DIURNAL CYCLE OF RADIATION

Figure 4-7 shows the temporal evolution of vertical structure during model run D50 (diurnal cycle of solar radiation, droplet concentration 50 cm^{-3}). Significant amounts of cloud water remain throughout the first three days of evolution, but on each of the following days

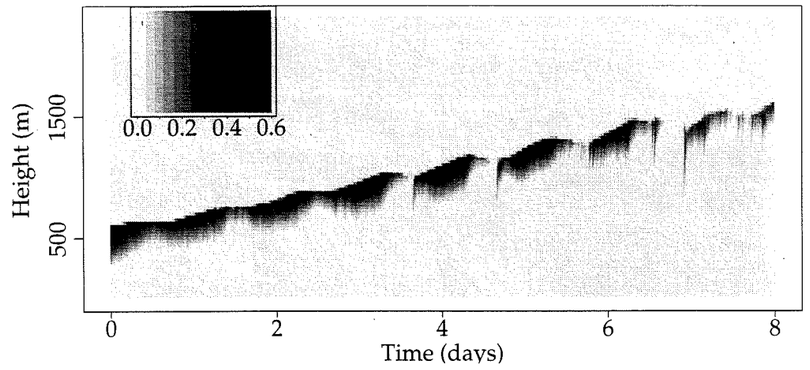

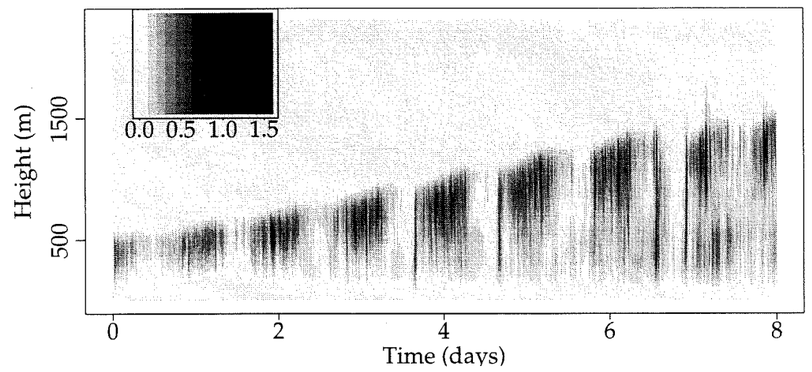

FIG 4-7. Vertical structure during model run D50 (diurnal cycle of solar radiation, droplet concentration 50 cm^{-3}). The upper panel shows q_c, the lower $\overline{w'^2}$. The cloud layer thins and, after the third day, vanishes entirely as absorbed solar radiation evaporates the cloud water. Clouds reform in the evening following bursts of cumulus convection which transport moisture from the ocean surface to the upper part of the boundary layer. In the absence of significant amounts of liquid water cloud top radiative cooling is reduced and turbulence levels decrease throughout the boundary layer, causing subsidence to exceed entrainment and the boundary layer depth to temporarily decrease.

daytime clearing is almost complete. On these days, clouds reform in the late afternoon following intense bursts of cumulus convection which transport moisture from the ocean surface to the top of the mixed layer. The absence of cloud water (and hence of cloud top radiative cooling) during the day in the latter part of the simulation dramatically lowers the turbulent kinetic energy levels, which in turn reduces the entrainment rate and hence the inversion height. The decrease in turbulence levels also allows for significant moisture stratification and conditional instability to develop in the boundary layer, which enhances the afternoon cumulus convection. This is evident in Figure 4-8, which shows that decoupling increases during daylight hours as the increased absorption of solar radiation partially offsets the radiative cooling driving turbulent mixing. Decoupling is especially pronounced after the third day of evolution. The reformation of cloud during evening hours enhances mixing, although moderate amounts of nocturnal decoupling persist after the third night of the simulation.

Figure 4-9 shows 1 hour averages of precipitation rate and cloud fraction derived from run D50. The diurnal cycle is clearly visible. Nighttime cloud thicknesses are higher than in run C50, and the thicker clouds produce more precipitation, some of which reaches the surface.

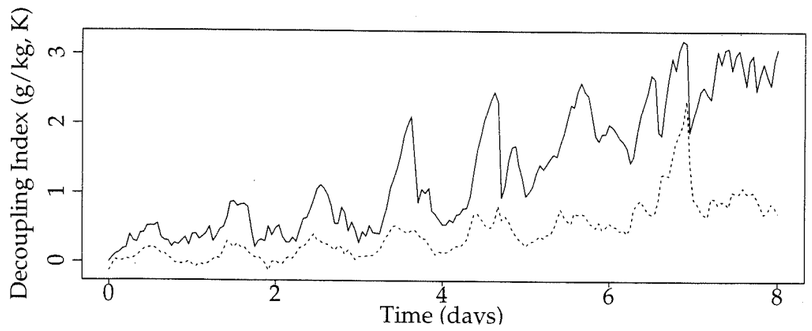

FIG 4-8. Decoupling history for run D50. Absorption of solar radiation moderately increases the degree of decoupling during daylight hours during the first three days of evolution. During the next five days, the absence of significant cloud top radiative cooling during the day allows for significant amounts of decoupling.

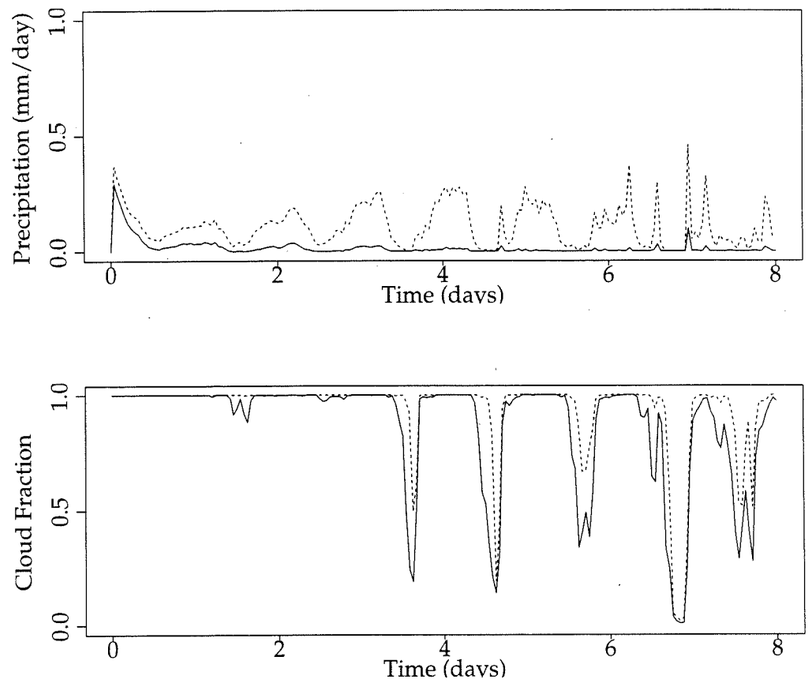

FIG 4-9. Domain averaged precipitation rate and cloud fraction for run D50 (diurnal cycle of radiation, droplet concentration 50 cm^{-3}). Cloud thickness and hence precipitation rate is greater at night than during run C50.

The clouds thin dramatically during the day, however. Even during the first three days of evolution, when the area cloud fraction remains near unity, a significant portion of the model domain is covered by very thin clouds, as the satellite cloud fraction estimate shows. On the last five days of evolution, the cloud disappears completely during the afternoon. In general, the boundary layer is somewhat more well mixed during nighttime hours and significantly more decoupled during daytime hours in run D50 than at the same point in run C50.

The evolution of the decoupling measures, precipitation rates, and cloud fraction for runs D400 and D50E (not shown) tell the same story about the role of precipitation in diurnally varying boundary layers as did runs C400 and C50E in relation to C50. The general characteristics (a strong diurnal cycle in cloud thickness, a gradual deepening of the boundary layer, the reformation of cloud in the evening following cumulus convection) of all three runs are the same. The temporal evolution of cloud fraction during run D400 are nearly indistinguishable from D50, although nighttime precipitation rates differ. Clouds are generally thinner during run D50E than in D50, and cloud fraction is slightly decreased.

4.4 *Discussion: Microphysics and Solar Radiation*

Based on the observations in Chapter 3, I postulated two things with regard to the control of cloud fraction in marine stratocumulus: that the absorption of solar radiation was required to reduce cloud fraction, and that cloud microphysics and drizzle acted at most to slightly modify this control. The simulations described in §4.3 confirm this view. In the presence of moderate amounts of solar radiation (the C runs) cloud fraction remained high as the sea surface temperature increased from 285 to 297 K over the course of 8 days. When the diurnal cycle of solar radiation is included, however (the D runs), the clouds thin enough during daylight hours to significantly reduce cloud fraction even over relatively cold water, and the cloud layer disappears entirely for the last five days of the simulation (once the SST has exceeded 291 K). I conclude, therefore, that solar absorption in excess of the diurnal average in July at 40° N is required to reduce cloud fraction from unity for environments typical of the FIRE region.

The droplet number concentration, and hence the amount of precipitation, do not significantly affect the evolution of cloud fraction in either the C or D runs. Even in the low droplet concentration runs, the amount of water reaching the surface is, on average, very small. When autoconversion is increased (the E runs) and rain rates become more realistic the cloud layer becomes thinner but does not tend to break up any more completely. In the diurnally averaged radiation runs, the amount of precipitation evaporating in the subcloud layer is also small. Thicker nighttime clouds in the diurnal cycle simulations produce larger amounts of precipitation and evaporation in the subcloud layer, but the evaporation is compensated for by the increased net radiative cooling.

Of note is the fact that cloud fraction remains high even in the face of some amount of decoupling, especially in the C runs. The persistence of cloud despite considerable stratification in both total water mixing ratio and potential temperature suggests that cumulus convection may be very efficient at transporting moisture from the sea surface to the upper part of the boundary layer.

Having assessed the observational results about the relative importance of solar absorption and microphysics in controlling cloud fraction in the marine boundary layer, we now turn to the role of the rate of change of sea surface temperature.

4.5 *Model Results: The Rate of Change Of Sea Surface Temperature*

Time-height cross sections of q_c and $\overline{w'^2}$ during run FAST are shown in Figure 4-10. The boundary layer is 600 m deep and the beginning of the run and deepens rapidly. Though the cloud thins during the daytime hours, substantial amounts of cloud water persist throughout the diurnal cycle for the first three days, becoming small only when the sea surface temperature exceeds about 296 K. Subcloud turbulence levels are somewhat reduced when the sun is up, but convection is vigorous through the entire depth of the boundary layer for the duration of the run.

The decoupling history, precipitation rate, and cloud fraction during run FAST are shown in Figure 4-11. The boundary layer remains nearly well-mixed for the first three days of evolution, and becomes only modestly decoupled on the fourth day. Precipitation rates are low after the model adjusts to its initial conditions. The clouds become thin enough for satellite cloud fraction to decrease to about 0.75 during the second and third days of the simulation, and significant clearing occurs at the highest sea surface temperatures. In general, however, cloud fraction is high during the course of the simulation.

Figure 4-12 shows the temporal evolution of vertical structure during model run SLOW. The run shares several characteristics in common with run D50. Daytime clearing due to solar absorption is complete during three of the four days of the simulation, although some cloud water remains throughout the third day. Clouds reform in the evening hours following bursts of cumulus convection. Turbulence levels decrease after sunrise and the turbulence

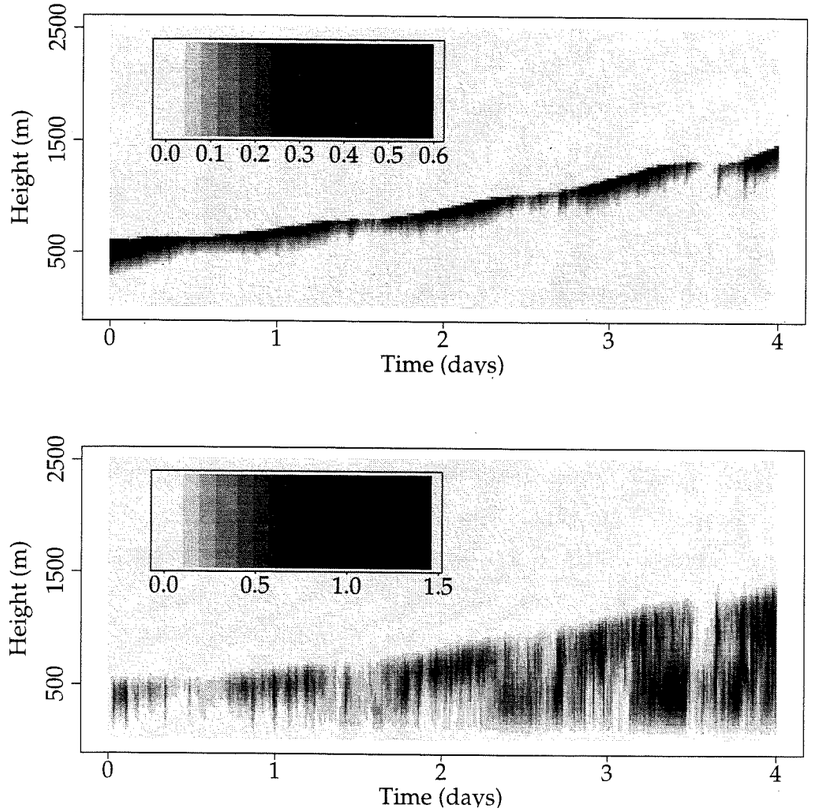

FIG 4-10. Vertical structure of q_c and $\overline{w'^2}$ during run FAST. Although a diurnal cycle in cloud liquid water is evident, substantial amounts of cloud water remain during daylight hours. Turbulence levels are high at all levels throughout the run.

becomes confined to the upper, cloudy, part of the boundary layer after sunrise. The boundary layer does not deepen significantly during the course of the simulation.

Figure 4-13 shows the temporal evolution of the decoupling measures, precipitation rate, and cloud fraction during run SLOW. As in run D50, the layer is less well mixed during daylight hours. The degree of decoupling is greater in run SLOW than at the equivalent sea sur-

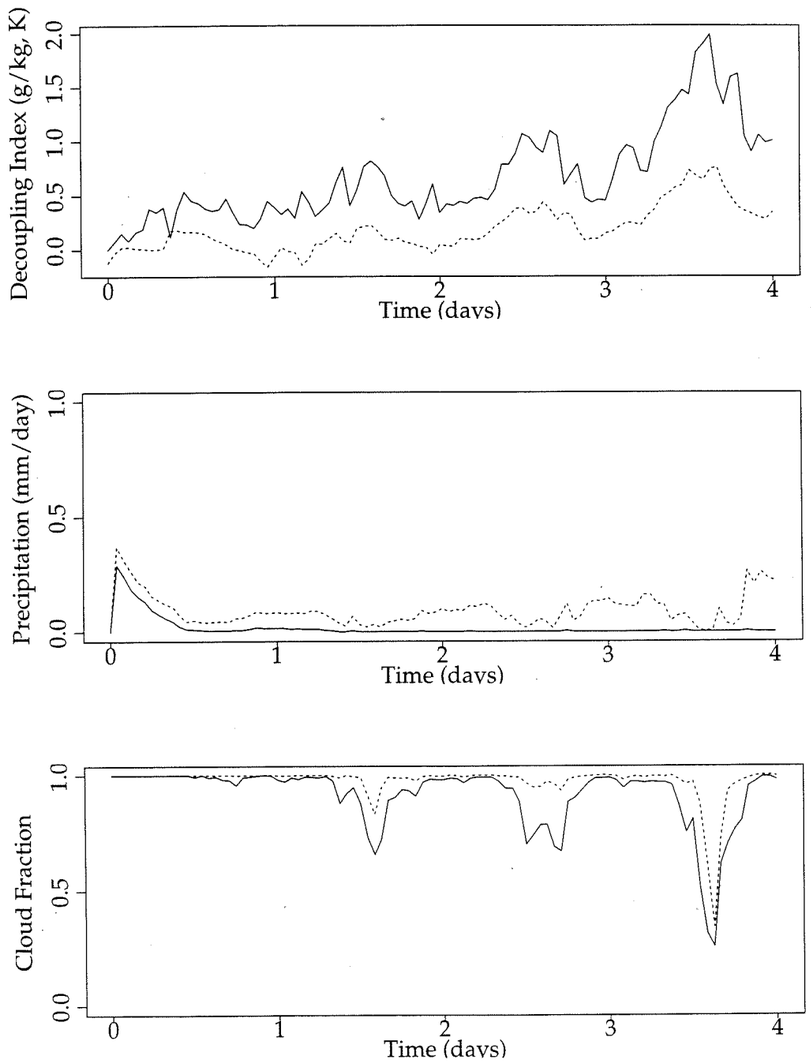

FIG 4-11. Decoupling, precipitation, and cloud fraction during run FAST. The layer remains nearly well-mixed and cloud fraction remains high through most of the simulation.

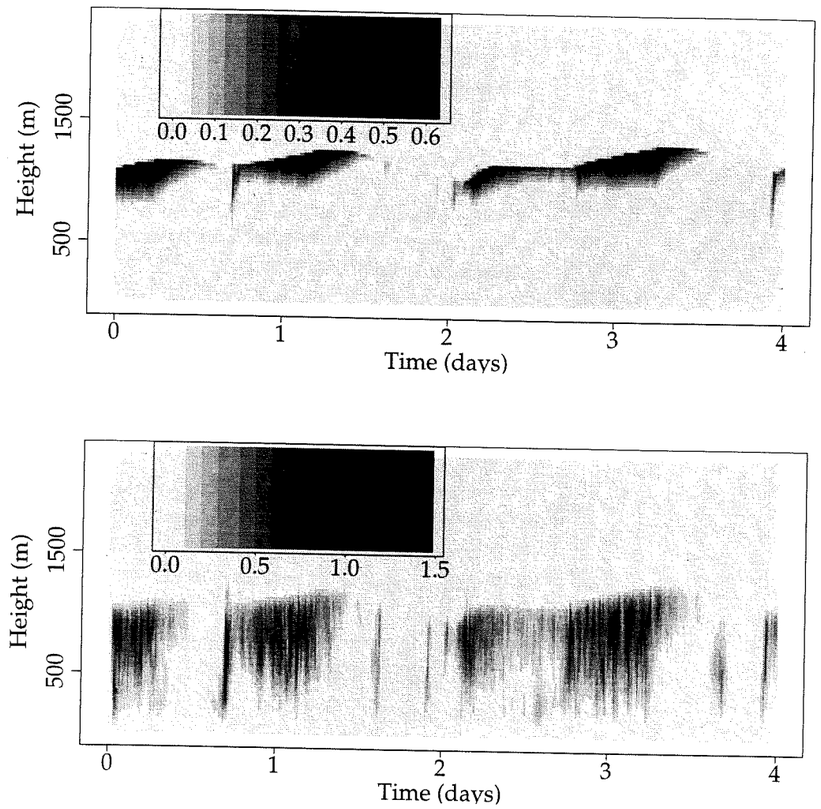

FIG 4-12. Temporal evolution of vertical structure during model run SLOW. Daytime clearing is nearly complete during most days, although some cloud water remains through the third day of the simulation. Turbulence levels are quite low, and the boundary layer does not deepen significantly with time.

face temperature in run D50, however: the stratification of θ_l, for example, exceeds 2 K during run SLOW as compared to about 0.5 K during the fourth day of D50. Both measures of cloud fraction fall near zero during the course of the four days of the simulation, and the clouds thin enough for satellite cloud fraction to drop to about 0.75 on the day in which clouds persist.

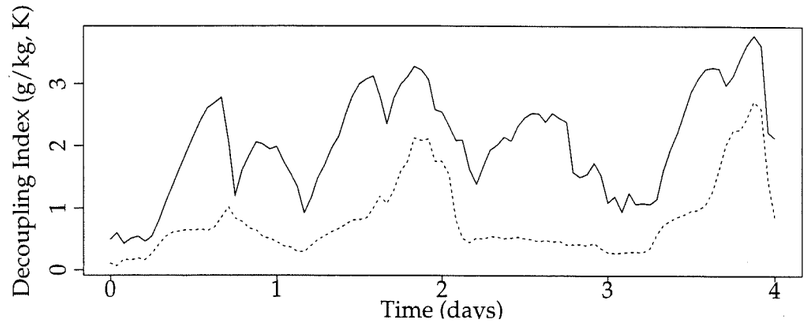

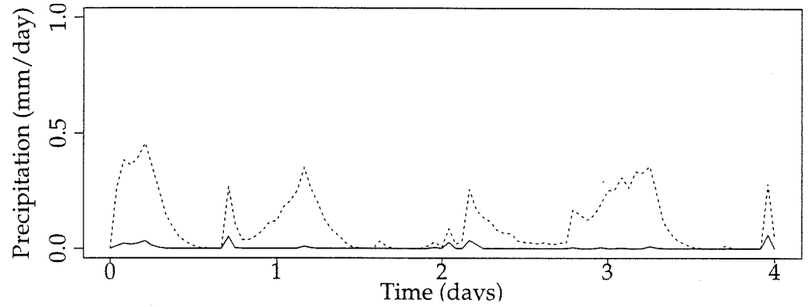

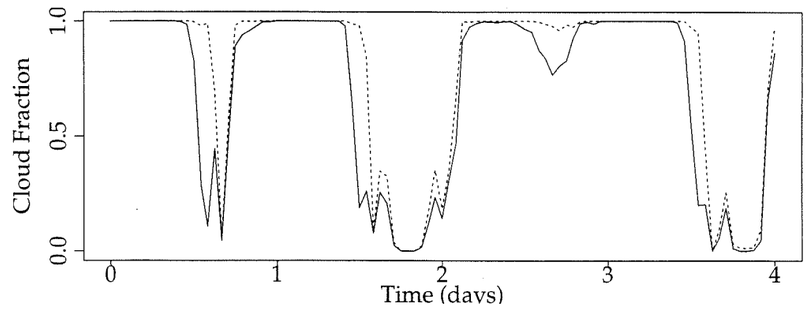

FIG 4-13. Decoupling measures, precipitation rate, and cloud fraction during run SLOW.

4.6 *Discussion*

The observations presented in §3.2 indicate that, in general, trajectories along which sea surface temperature is rapidly increasing show high fractional cloudiness, while the cloud fraction in boundary layers travelling over small changes in SST tends to be lower. This behavior is reproduced in model runs SLOW and FAST. During run SLOW decoupling is pronounced even at night, which leads to rapid dissipation of clouds during the daylight hours on most days. The boundary layer remains nearly well-mixed throughout the four days of run FAST, however, allowing cloud fraction to remain high throughout the entire diurnal cycle until the sea surface temperature becomes quite warm. The boundary layer remains well-mixed in run FAST due to the large surface fluxes of heat and moisture at the surface, which provide a significant source of buoyancy and turbulent kinetic energy. These fluxes are much smaller in run SLOW. Although deeper boundary layers are more likely to become decoupled, run FAST remains nearly well-mixed even on the third day, when the boundary layer depth is roughly the same as in run SLOW.

Both the short-term observations in §3.2 and an analysis on climatological time scales (Klein et al., 1994) show that the rate of change of sea surface temperature affects cloud fraction after about a day. This is not a conspicuous feature of these simulations, since both run SLOW and FAST show more or less the same behavior for the entire four days of simulation time. The rate of change of SST appears to be a fairly good predictor of cloud fraction in a Lagrangian framework, however, and might be useful in developing schemes for predicting cloudiness in large scale models.

5 A Simple Model Linking Cloud Albedo and Droplet Number Concentration

The observations described in Chapter 3 and the large eddy simulations in Chapter 4 do not support the hypothesis that precipitation plays a major role in controlling cloud fraction in the marine cloud-topped boundary layer. Net albedo, however, is the product of cloud fraction and cloud albedo, and cloud microphysical processes can influence the albedo of existing clouds by affecting either cloud droplet size or cloud thickness.

In this chapter I explore the sensitivity of boundary layer cloud thickness and albedo to droplet number concentration using a simple model which links these quantities through the processes of precipitation and solar absorption. This represents a fundamentally different approach than I have taken in previous chapters. The steady state mixed-layer model is unrealistically simple in two respects: it is one-dimensional, ignoring horizontal inhomogeneity in cloud properties and, more importantly, it neglects both the diurnal cycle of solar insolation and the Lagrangian evolution on which I have focussed so far. The advantage of this simplicity, however, is that the model is analytically solvable, and the results are intriguing. The gist of this work was described in Pincus and Baker (1994).

The connection between mean cloud thickness h (m) and droplet number concentration N (cm^{-3}) in simple models can be qualitatively understood by considering the processes controlling marine stratocumulus evolution described in §1.1 and shown in Figure 1-3. Cloud base height varies relatively little over the subtropical ocean, so that h is determined primarily by the inversion height, which is established by a balance between entrainment and downward-directed large scale subsidence. Entrainment is driven by the turbulence generated by cloud top radiative cooling, and the entrainment rate may be diminished by heating of the boundary layer via the absorption of solar radiation or through the evaporation of precipitation. For constant subsidence, therefore, h increases with longwave cooling and decreases in the presence of radiative heating and precipitation. Both solar absorption and precipitation, moreover, increase with the characteristic cloud droplet size r, which increases with h and decreases with N. For a particular value of N, consequently, the equilibrium value of h is determined by a balance between cloud top radiative cooling and the heating due to entrainment, precipitation, and solar absorption.

5.1 *Developing the Model*

I use a steady state mixed layer model of the marine boundary layer to investigate the dependence of cloud thickness and albedo on droplet number concentration. Though somewhat physically unrealistic, this type of model has the advantage of extreme simplicity, which allows for easy numerical (or, in some cases, analytical) solution.

Mixed-layer models were first used to describe the cloud-topped marine boundary layer by Lilly (1968), and have since been used to investigate the steady-state behavior (Schubert et al., 1979a) and the Lagrangian evolution (Schubert et al., 1979b; Pincus et al., 1990) of marine stratocumulus, the sensitivity of bulk cloud properties to radiation (Fravalo et al., 1981), the circumstances fostering decoupling (Wyant and Bretherton, 1992), as well as the interpretation of aircraft measurements (Nicholls, 1984).

In a mixed-layer model, the entire boundary layer between the surface and the capping inversion is considered to be a thoroughly mixed, horizontally uniform slab. The state of the layer is represented in terms of variables describing the energy and moisture content and the boundary layer depth. The energy and moisture variables are chosen such that they are conserved during evaporation and condensation, but they may be modified by transfers of heat and moisture from the surface and across cloud top, as well as by precipitation and radiative heating and cooling. The rate of change with time of the variables is determined by considering budget equations describing these processes. Since the model assumes that the boundary layer is well-mixed, the results are most applicable to shallow boundary layers with high fractional cloudiness.

5.1.1 BASIC MIXED LAYER EQUATIONS

I formulate the model in terms of the total water mixing ratio $q = q_v + q_l$ (kg-water/kg-air), the liquid water static energy $s = c_p T + gz + Lq_l$ (J/kg-air), and the boundary layer depth z_i (m). The equations describing a mixed layer in steady state are (see, for example, Schubert et al., 1979a, although they use a different thermodynamic variable):

$$q_m = \frac{w_0 q_0 + w_e q_+ - P(0)}{w_0 + w_e}$$

$$s_m = \frac{w_0 s_0 + w_e s_+ + LP(0) + \frac{SW - LW}{\rho_a}}{w_0 + w_e} \qquad (5\text{-}1)$$

$$w_e = Dz_i$$

In these expressions, w_0 is the surface transfer velocity (m/s), w_e the cloud-top entrainment velocity, $P(0)$ the precipitation rate at the surface (kg-water/kg-air m/s), D the large scale divergence (s^{-1}), LW and SW the diurnally averaged absorbed shortwave and net emitted longwave cooling radiative fluxes (W m^{-2}), and the subscripts 0, m, and + denote values of q and s at the ocean surface, in the mixed layer, and above the inversion, respectively. Cloud thickness h can be computed as the difference between cloud top and cloud base heights:

$$h = z_i - z_c \qquad (5\text{-}2)$$

Cloud base height z_c, in turn, is diagnosed from (Schubert et al., 1979a)

$$z_c = \frac{q_0 - q_m}{-\beta_d} \qquad (5\text{-}3)$$

where β_d (kg-water kg-air^{-1} m^{-1}) is the lapse rate of saturation mixing ratio during dry (unsaturated) adiabatic ascent.

5.1.2 ENTRAINMENT CLOSURE

Solution of the mixed layer equations requires an entrainment closure which determines the mass flux across cloud top. A variety of closure schemes have been suggested. Schubert et al. (1979a) proposed that entrainment be diagnosed as the weighted mixture of two limits due to Lilly (1968): the minimum entrainment assumption, in which the buoyancy flux at cloud base is assumed to vanish, and the maximum entrainment assumption, which supposes that the net production of buoyancy in the layer vanishes. Nicholls (1984), in a variation on

this theme, suggested that the entrainment velocity was some fraction of the turbulent velocity scale in the layer, which is itself proportional to the layer-integrated buoyancy flux.

I close the model by assuming that buoyancy flux vanishes at cloud base (the "minimum entrainment assumption"). Since, in equilibrium, buoyancy flux is constant throughout the subcloud layer, the minimum entrainment assumption also predicts no buoyancy flux at the surface, which implies that the air-sea virtual temperature difference vanishes. The mixed layer static energy s_m can therefore be approximated $s_m \approx s_0$, and the energy equation in (5-1) rearranged to read:

$$w_e (s_0 - s_+) = LP(0) + \frac{SW - LW}{\rho_a} \tag{5-4}$$

5.1.3 PRECIPITATION PARAMETERIZATION

In stratocumulus clouds, precipitation primarily takes the form of drizzle (Albrecht, 1989), which is primarily initiated autoconversion, the collision of small cloud droplets with each other. A survey of previously published parameterizations of autoconversion (Chen and Cotton, 1987; Baker, 1993) and precipitation in stratocumulus clouds (Turton and Nicholls, 1987) show that all may be expressed in the general form:

$$P(z_c) = P_0 r^n h^m \tag{5-5}$$

where $P(z_c)$ (kg-water/kg-air m/s) is the precipitation flux falling through cloud base, r is a characteristic droplet radius, and the constant of proportionality P_0 has dimensions (kg-water/kg-air meters^{1-m-n} s^{-1}). Since cloud thickness and cloud top liquid water content are linearly related in a mixed layer model, (5-5) may also be expressed in terms of cloud water content. The previously published schemes noted above may differ in detail from this exact form by dictating a critical radius below which autoconversion ceases (Chen and Cotton, 1987; Baker, 1993) or by assuming that the dependence on droplet radius reaches some limiting value for droplets bigger than a certain size (Turton and Nicholls, 1987).

Drizzle drops evaporate as they fall through the unsaturated air between cloud base and the surface at a constant rate Γ_p (kg-water kg-air^{-1} m s^{-1} m^{-1}), so that the precipitation flux at the surface is

$$P(0) = P(z_c) - \Gamma_p z_c \tag{5-6}$$

The precipitation parameterization (5-5) and (5-6) requires knowledge of h and the characteristic cloud droplet radius r, which may in turn be diagnosed from h and N using the same assumptions made in §2.2.4: that cloud liquid water content increases linearly with height, and that the water is divided into N equally-sized drops per unit volume (or, alternatively, that all moments of the droplet size distribution are identical). The volume mean radius is then determined by:

$$\begin{aligned} r &= \left(\frac{3}{4\pi} \frac{\rho_a}{\rho_l} \frac{\beta_m h}{N} \right)^{1/3} \\ &= C_1 \left(\frac{h}{N} \right)^{1/3} \end{aligned} \tag{5-7}$$

5.1.4 RADIATION PARAMETERIZATION

The shortwave parameterization of Slingo (1989) predicts broadband solar absorption given knowledge of cloud liquid water path and the effective radius. Figure 5-1 shows the absorption predicted as a function of cloud thickness and droplet number concentration for an average value of solar zenith angle $\mu_0 = 0.354$. The solid lines from top to bottom indicate absorption at droplet concentrations of 25, 100, and 500 cm^{-3}; the dashed lines show linear least squares fits with 0 intercept to each computation. The slopes of the best fit lines vary from 3.78×10^{-4} for $N = 25$ cm^{-3} to 2.93×10^{-4} for $N = 500$ cm^{-3}. At a typical value of $N = 100$ cm^{-3} the slope of the best fit line $C_2 = 3.0 \times 10^{-4}$, which may be used to parameterize solar absorption as:

$$SW = C_S \overline{\mu_0} Tr C_2 h \tag{5-8}$$

where Tr is the transmissivity of the atmosphere overlying the boundary layer and C_S the solar constant at the top of the atmosphere. Relative to Slingo's parameterization, (5-8) slightly underestimates solar absorption at low droplet concentrations and overestimates absorption at high concentrations; I discuss the impact of this error in §5.4.

The longwave cooling rate LW depends on the difference between the downwelling longwave radiation at cloud top and the radiation emitted by the cloud, which radiates as a black

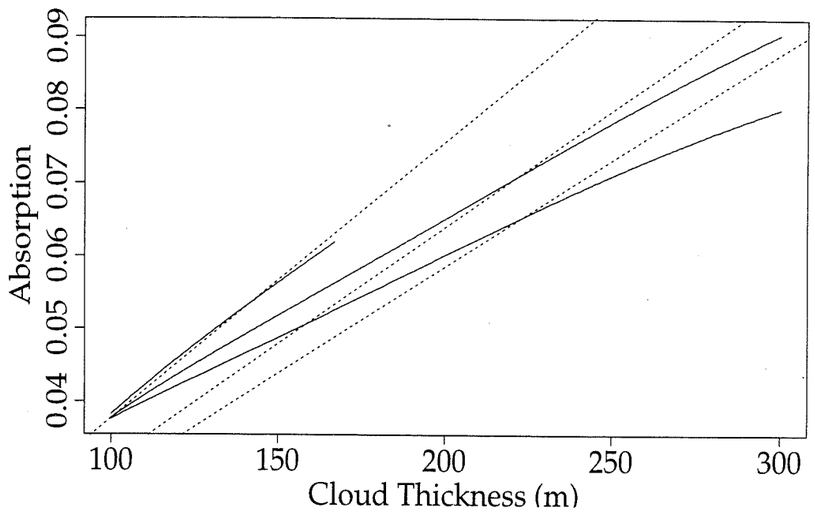

FIG 5-1. Solar absorption as a function of cloud thickness and droplet number concentration. Solid lines from top to bottom indicate absorption at concentrations of 25, 100, and 500 cm^{-3}, dashed lines show linear least squares fits with 0 intercept. The parameterization is due to Slingo (1989).

body. The downwelling radiation depends in turn on the profile of water mixing ratio and temperature in the atmosphere above the cloud, which is essentially uncoupled from the boundary layer. Since variations in outgoing longwave radiation due to variations in cloud top temperature are small (which may be confirmed by a look ahead to Figure 5-2), I fix the longwave cooling rate LW.

5.1.5 PARAMETERIZED EQUATIONS

Substitution of the entrainment closure and the drizzle and radiation parameterizations into the model equations yields:

$$q_m = \frac{w_0 q_0 + Dz_i q_+ - P_0 C_1^n r_0^{-n} N^{\frac{-n}{3}} h^{\frac{n}{3}+m} - \Gamma_p z_c}{w_0 + Dz_i}$$

$$z_i = \frac{LP_0 C_1^n r_0^{-n} N^{\frac{-n}{3}} h^{\frac{n}{3}+m} - L\Gamma_p z_c}{D(s_0 - s_+)} + \frac{C_s \overline{\mu}_0 TrC_2 h - LW}{D(s_0 - s_+)\rho_a} \qquad (5\text{-}9)$$

$$h = z_i - \frac{(q_0 - q_m)}{\beta_d}$$

After substituting for z_c using (5-3) in the water equation and (5-2) in the cloud top height equation, (5-9) can be solved algebraically for the cloud thickness h. The number of solutions is determined by the values of n and m. Numerical values of h can be determined once the values of the various external parameters have been specified.

5.2 *Solutions to the Model*

The model solutions depend strongly on the choice of values for the physical parameters. To explore the sensitivity of the model to variations in N alone, I choose nominal parameter values representative of marine stratocumulus in the FIRE region (Bretherton, 1994), which are listed in Table 5-1. The lapse rates β_m and β_d are set to -2×10^{-6} and -5×10^{-6} kg-water kg-air^{-1} m^{-1} respectively. The exponents m and n and constants r_0 and P_0 in the precipitation parameterization are chosen to match the parameterization of Turton and Nicholls (1987). Given these values of m and n there are four solutions to the algebraic equations for h; the physically relevant solutions are those for which h, q, and z_i are all positive.

Figure 5-2 shows cloud thickness h and cloud top height z_i as a function of droplet number concentration N in the range 10–1000 under the conditions in Table 5-1. Most of the variation in cloud thickness is due to changes in cloud top height, although cloud base height does vary about 60 m across the same range. Cloud top height increases with droplet concentration because droplet size and therefore precipitation decreases as number concentration increases. Since precipitation at the surface adds latent heat to the cloud layer, entrainment of warm, dry air is suppressed as precipitation increases. If changes in droplet concentration did not affect the water and energy budgets through the production of precipitation (i.e. if

TABLE 5-1: Mixed Layer Model Parameter Values

large scale divergence	D	5×10^{-6} s^{-1}
drizzle evaporation rate	Γ_p	8.6×10^{-9} kg kg^{-1} m s^{-1} m^{-1}
surface mixing ratio	q_0	11.8 g kg^{-1}
surface liquid static energy	s_0	2.91×10^5 J kg^{-1}
tropospheric mixing ratio	q_+	4 g kg^{-1}
tropospheric static energy	s_+	3.00×10^5 J kg^{-1}
surface transfer velocity	w_0	.017
solar constant	S_C	1370 W m^{-2}
average solar zenith angle cosine	$\overline{\mu_0}$	0.354
atmospheric transmissivity	Tr	0.8
absorption coefficient	C_2	3.20×10^{-4} W m^{-2} m^{-1}
nominal droplet size	r_0	10 μm
precipitation constant	P_0	3×10^{-11} kg kg^{-1} m^{-1} μm^{-3} s^{-1}
precipitation exponents	m, n	1, 3

no precipitation terms appeared in (5-9)), h and z_i would not vary from values of 648 m and 418 m, respectively. Although both h and z_i depend on the environmental conditions including the large scale divergence D, the jump in liquid water static energy ($s_+ - s_0$) and the net longwave cooling LW, the trends in h and z_i shown in Figure 5-2 are robust for realistic variations in environmental conditions.

Figure 5-3 shows the droplet radius (μm) diagnosed from (5-7) and surface precipitation flux (mm day^{-1}) as determined from (5-6) as functions of droplet concentration. In the original parameterization of Turton and Nicholls (1987), precipitation rate did not depend on droplet radius once the radius exceeded 10 μm. Equation (5-5), therefore, gives more drizzle falling through cloud base than does the original parameterization for large r. At the lowest droplet concentrations the difference is about a factor of 4, but the predicted

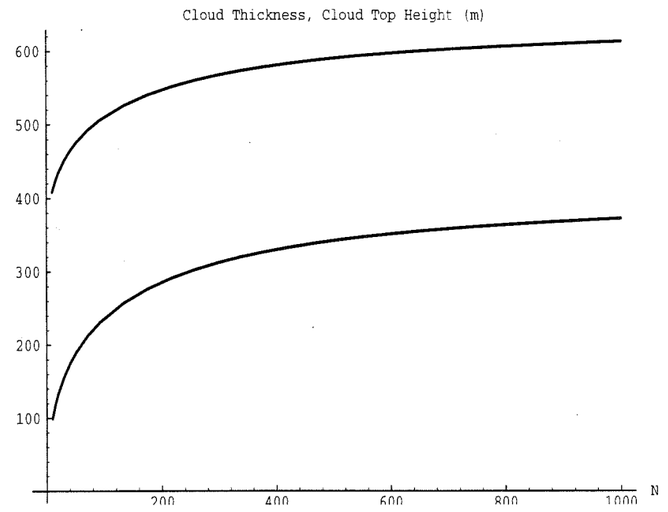

FIG 5-2. Cloud thickness and cloud top height as a function of droplet number concentration. Cloud top height increases with droplet concentration because droplet size and thus precipitation decreases as number concentration increases, allowing for more entrainment. Cloud base height varies about 60 m over the range of droplet concentrations shown. If precipitation were not included in the model, h and z_i would be fixed at 420 and 650 m.

precipitation fluxes are within the range of those observed in the FIRE region by Austin et al. (1994b).

The optical properties of the layer can be computed from the model solutions for cloud thickness using the microphysical assumptions made in §5.1.3. Visible wavelength cloud optical depth τ can be determined as a function of h and N by solving (2-5):

$$\tau = \frac{1}{2}\left(\frac{9\pi}{2}\right)^{1/2}\left(\frac{\beta_m \rho_a}{\rho_l}\right)^{2/3} N^{1/3}\, h^{5/3} \qquad (5\text{-}10)$$

Cloud albedo A can be ascertained from τ using the two stream approximation (Meador and Weaver, 1980):

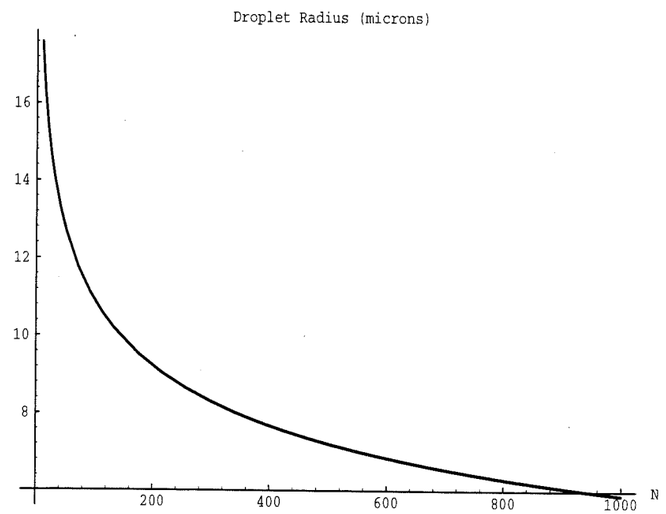

FIG 5-3. Cloud microphysical properties as a function of droplet number concentration. Droplet mean radius (μm, upper panel) is computed at cloud top; precipitation flux (mm/day, lower panel) is computed at the surface.

$$A = \frac{(1-g)\,\tau}{2 + (1-g)\,\tau} \tag{5-11}$$

where g is the asymmetry factor (assumed constant at $g = 0.86$), and the cloud is assumed to overly a non-reflecting surface.

Figure 5-4 shows cloud optical depth as determined from (5-10) and cloud albedo in percent as determined from (5-11). Were droplet radius held fixed as cloud thickness varied cloud optical depth would vary as h^2. Both the increase in precipitation with r and the inclusion of r in the computation of optical depth (5-10), however, cause optical depth to vary more gently with h in this model. Nonetheless, cloud albedo does increase rapidly with droplet number concentration when the latter quantity is small.

5.3 *Sensitivity to Changes in Droplet Concentration*

The sensitivity of model predicted cloud thickness to changes in droplet number concentration (expressed as the derivative $\frac{dh}{dN}$) is of interest both for computing the albedo sensitivity and because it indicates in which regimes changes in droplet number concentration are likely to have a significant effect on cloud thermodynamic properties. I compute this sensitivity by substituting the expressions for z_i and q_m into the expression for h in (5-9), yielding an expression with h on both the right and left hand sides, then taking the derivative of both sides with respect to N and solving for $\frac{dh}{dN}$.

Figure 5-5 shows the sensitivity of cloud thickness to changes in droplet number concentration (m^4) as a function of droplet concentration. As might have been surmised from Figure 5-2, this sensitivity is greatest when the concentration is smallest, since small changes in number concentration have the largest impact on droplet radius (and hence precipitation) in this regime. At extremely low droplet concentrations (10 cm^{-3}), the addition of a single droplet per cubic centimeter can increase equilibrium cloud thickness by 4 meters.

In §1.2.2 I introduced the concept of cloud albedo susceptibility, the differential sensitivity of cloud albedo to droplet number concentration. Susceptibility as traditionally defined (see (1-5)) is computed assuming that cloud liquid water remains fixed as droplet concentrations vary:

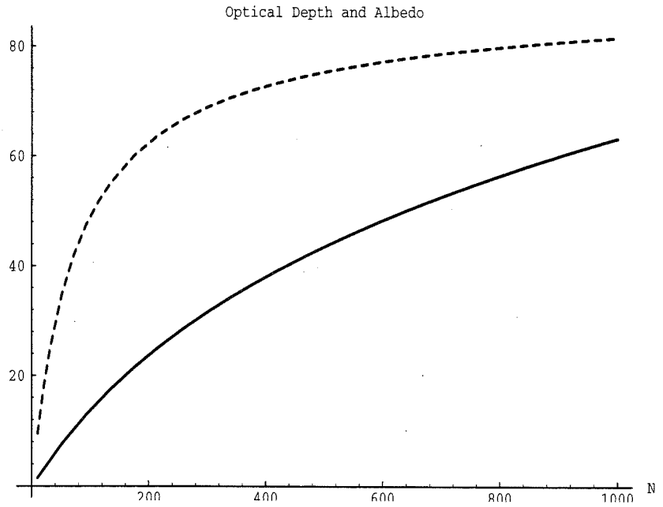

FIG 5-4. Cloud optical properties as a function of droplet number concentration. The solid line shows visible wavelength optical depth; the dashed line albedo in percent.

$$S_0 \equiv \left.\frac{\partial A}{\partial N}\right|_{q_l} = \left.\frac{dA}{d\tau}\frac{\partial \tau}{\partial N}\right|_{q_l} \tag{5-12}$$

This assumption can now be relaxed using the model results. The sensitivity of optical depth to changes in droplet number concentration can by computed by taking the derivative of (5-10) with respect to N:

$$\frac{d\tau}{dN} = \left.\frac{\partial \tau}{\partial N}\right|_{q_l} + \frac{\partial \tau}{\partial h}\frac{dh}{dN} = \frac{\tau}{3N}\left[1 + \frac{5N}{h}\frac{\partial h}{\partial N}\right] = \frac{\tau}{3N}[1+\delta] \tag{5-13}$$

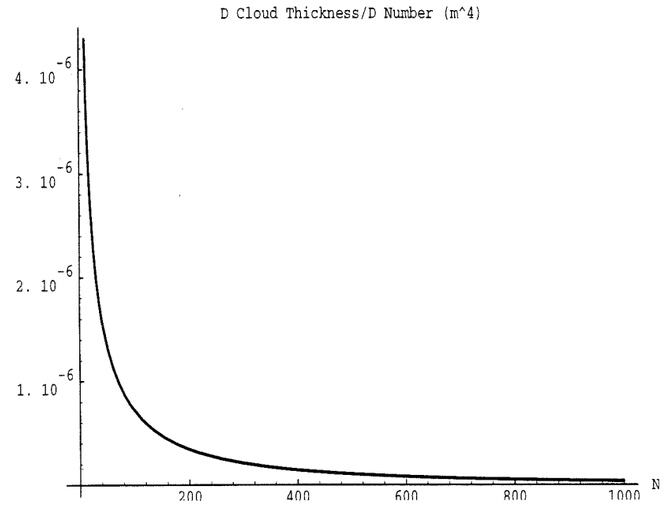

FIG 5-5. Sensitivity of cloud thickness to changes in droplet number concentration. At very low concentrations, the addition of 1 droplet cm^{-3} can increase cloud thickness by 4 m.

Albedo susceptibility S is then computed by taking the derivative of (5-11) with respect to τ and combining it with (5-13) to yield

$$S = \frac{dA}{dN} = \frac{dA}{d\tau}\frac{d\tau}{dN} = \frac{2(1-g)}{[\tau(1-g)-2]^2} \times \frac{\tau}{3N}[1+\delta] = S_0\,[1+\delta] \tag{5-14}$$

The factor δ in (5-14) represents the contribution to S due to changes in cloud thickness induced by changes in N, as compared to the factor 1 due to changes in droplet radius alone. Figure 5-6 shows δ as a function of droplet concentration. As Figure 5-6 shows, changes in cloud thickness in this model play a significant role in modulating cloud albedo at all droplet concentrations and cloud optical depths. At low droplet concentrations, changes in cloud

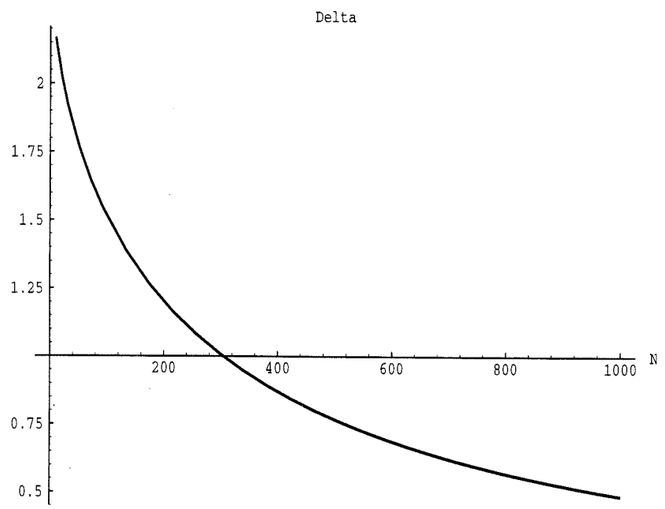

FIG 5-6. The relative contribution of cloud thickness changes to albedo susceptibility.

thickness with droplet number are roughly twice as important in determining the sensitivity of albedo as are changes in droplet size with droplet number.

5.4 *Discussion: Microphysics and Cloud Albedo*

The results of this model imply that cloud droplet number concentrations can strongly modulate boundary layer cloud thickness and cloud albedo through the processes of precipitation. The effect is largest when number concentrations are lowest, but changes in cloud thickness significantly increase cloud albedo susceptibility at all number concentrations. The results suggest that, even in the absence of changes in cloud fraction, precipitation processes can play an important role in determining stratocumulus cloud albedo through the modulation of cloud thickness.

The model may also explain the differences between the two types of ship tracks noted in §1.2.4. If particles emitted by passing ships increase droplet concentrations in regions where the ambient concentration is low, cloud thickness and cloud albedo will be strongly modified as the amount of precipitation is dramatically reduced. If, on the other hand, droplet concentrations are already high, the addition of even large numbers of additional droplets will have little effect on cloud albedo, as Figure 5-4 shows.

The many assumptions made and parameterizations used to develop the model are, of course, sources of uncertainty. The error introduced by ignoring the dependence of solar absorption on droplet size in (5-8) causes a slight underestimate of $\frac{dh}{dN}$, since enhanced absorption at lower droplet concentrations (thinner clouds but larger droplet radii) acts to thin the cloud even more. As Platnick and Twomey (1994) point out, formal evaluation of the derivative $\frac{dA}{dN}$ also includes a term representing the change in asymmetry factor g with changes in N and r. For the range of droplet radii shown in Figure 5-3, however, g shows no appreciable variation. Finally, the precipitation parameterization used for this model predicts significantly higher drizzle rates than does the autoconversion scheme selected for the HUSCI runs (§4.1.1), pointing out the uncertain state of our understanding of precipitation formation in stratiform clouds.

More significant are several key processes not included in the model at all. Mixed layer models represent an extremely idealized view of marine boundary layer dynamics, and truly well-mixed boundary layers were observed only occasionally during FIRE (Paluch and Lenschow, 1991). In particular, a mixed layer model is not able to represent the cooling of the subcloud layer due to evaporation of precipitation, which may decrease cloud thickness by inhibiting vertical mixing. The steady state solutions ignore both the Lagrangian nature of stratocumulus evolution I have focussed on to this point and the diurnal cycle of solar radiation, which strongly modifies cloud thickness. The results in this chapter should therefore be viewed as suggestive rather than conclusive. Given the magnitude of the effect computed here, however, more systematic investigation with a vertically resolved model seems worthwhile.

6 Summary and Conclusions

At the beginning of this dissertation I described the importance of marine boundary layer clouds in determining the Earth's radiation budget, and set out to investigate the degree to which microphysical processes control cloud fraction and cloud albedo in the subtropical marine boundary layer. I noted that marine boundary layer clouds in particular are difficult to observe because they evolve over long time periods in a constantly changing environment. I described a new technique for observing this Lagrangian evolution using a combination of operational weather analyses and satellite imagery, which I then applied to assess the relative importance of precipitation, solar insolation, and the rate of change of sea surface temperature in controlling cloud fraction. Finally, I used a simple model linking droplet number concentration and precipitation to explore the role of microphysics in controlling cloud albedo.

6.1 *Results and Prospects: The Lagrangian Observational Technique*

The Lagrangian nature of marine stratocumulus evolution poses a difficult problem for observational investigations in the cloud-topped marine boundary layer. The observational technique developed in Chapter 2 can provide a valuable alternative to arduous and expensive in situ measurements. It is pleasing in being one of the first attempts to use remote sensing in process (as opposed to descriptive or diagnostic) studies of clouds. Although its use in the subtropical summertime marine boundary layer is particularly unambiguous, it might well be extended to any geophysical situation in which horizontal advection plays an important role in determining the long term evolution of the system.

An anecdotal caution about the method is in order. Chapter 3 described two sets of trajectories observed with the Lagrangian technique. I have attempted to use the technique in a variety of other contexts, including investigations of stratocumulus breakup (Pincus et al., 1992), formation, and the temporal evolution of mesoscale structure. None of these studies are reported in this dissertation because none produced entirely convincing results. Some problems arose from the geographically limited satellite images available. For example, my original research plan was to use the Lagrangian technique to observe stratocumulus breakup and the stratocumulus to trade cumulus transition in the northeast Pacific. This

quickly proved unfeasible since the satellite images I obtained did not include regions where breakup is common; the same issue arose in studies of stratiform cloud formation. Other difficulties seem to be inherent in the technique. A systematic appraisal of the temporal evolution of mesoscale structure, for instance, will require an image processing tool which can robustly characterize the cloud size and shape of the mesoscale structure of the cloud layers. Such a tool have so far proved beyond my abilities to construct, although I anticipate pursuing this problem further. More generally, it is important to note that the amount of information available from satellite visible and infrared imagery alone is quite limited. The Lagrangian observational technique is most successful when combined with other sources of information such as in situ measurements (as in Chapter 3 or Bretherton and Pincus, 1994) or, conceivably, remote sensing measurements of quantities such as liquid water path or cloud effective radius. Coincident multispectral observations such as will be available from the EOS platforms may open new avenues for exploration.

One promising direction for future work lies in exploring the links between aerosol and droplet concentrations and cloud lifetime. The control of cloud albedo and cloud fraction by microphysical processes is one of several arenas in which clouds interact with atmospheric aerosols, which affect cloud properties by acting as cloud condensation nuclei on which droplets form. Another possible relationship arises through the effect of droplet number concentrations on cloud lifetime (Penner et al., 1993). It is conceivable, for example, that increases in aerosol and hence droplet concentrations may suppress precipitation and increase the temporal (independent of the spatial) extent of cloud layers. Observational studies of these interactions must necessarily rely on Lagrangian observations, and the technique developed in this dissertation seems a natural one to use.

The technique may also be useful in conjunction with in situ Lagrangian measurements made as part of extended field projects. Bretherton and Pincus (1994), for example, used satellite observations of cloud fraction and cloud optical depth made following parcel trajectories to put aircraft measurements made along those trajectories into a larger scale context. In situ Lagrangian measurements are to be repeated during the upcoming ACE experiments.

6.2 *Results and Prospects: Models of the Cloud-topped Marine Boundary Layer*

The models presented in Chapter 4 and Chapter 5 represent two extremes in the range of simplicity and abstraction. In particular, the simple model used in Chapter 5 clearly neglects two important pieces of physics: the possible development of vertical thermodynamic structure in marine boundary layers which do not remain well-mixed, and the Lagrangian component of stratocumulus evolution with which the first four chapters of this dissertation are concerned. The advantage to this simplification is that it made the model analytically solvable. The results are provocative and suggest that further investigation is warranted, but such work ought to be performed with a more sophisticated model.

A complicated model, however, is no guarantee of accuracy. The detailed simulations made with the HUSCI large eddy simulation and reported in Chapter 4, for example, produce unrealistically small rain rates in spite of an accurate autoconversion parameterization. These low precipitation fluxes can be traced to representation of rainwater production in the model, which does not represent the recirculation of a very small number of large drops known to be responsible for much of the precipitation flux in marine stratocumulus clouds. The conclusions regarding microphysical control of cloud fraction drawn in that chapter are not sensitive to the exact precipitation parameterization, as the runs performed with enhanced autoconversion showed. The sensitivity of albedo to droplet concentration computed from the simple model in Chapter 5, however, arises from the strong dependance of precipitation rate on cloud thickness and cloud liquid water path, which HUSCI does not exhibit. To resolve this discrepancy, and to allow a model like HUSCI to be used to study albedo sensitivity, a better understanding of precipitation formation processes in stratocumulus clouds and better explicit representation or parameterization of these processes in hydrodynamic models will be required.

6.3 *Microphysical Control of Marine Stratocumulus Radiative Properties*

Based on evidence from Lagrangian observations and detailed numerical simulations, it appears that the temporal evolution of cloud fraction in the FIRE region is dominated by the diurnal cycle of solar insolation. Neither the observations nor the simulations support the hypothesis that precipitation plays an important role in the regulation of fractional cloud-

niess in the marine boundary layer. Cloud fraction may remain high throughout the course of the diurnal cycle under at least two circumstances: if the parcel is subject to rapidly increasing sea surface temperatures, leading to high surface buoyancy fluxes which keep the cloud layer and surface layer well-coupled, or if the clouds become quite thick (optical depth greater than about 10) during the nighttime hours, which allows the cloud to become thin without breaking up. It is important to note, however, these results were derived in a region in which fractional cloudiness in the boundary layer is quite high, and it may well be that precipitation plays a role in modifying cloud fraction during the stratocumulus to trade cumulus transition (Bretherton, 1992).

Although precipitation does not strongly affect cloud fraction, a simple model linking precipitation, droplet concentration, and cloud thickness suggests that microphysics and precipitation may well be a key determinant of cloud albedo. Precipitation may greatly enhance the albedo susceptibility of cloud layers by modifying cloud thickness and liquid water path as droplet concentrations change. I have neglected both the diurnal variation of solar insolation and the possible development of decoupling, which should act to decrease cloud thickness, rain rate, and hence albedo for low droplet concentrations and thick clouds. Even within the context of the simple mixed layer model used in Chapter 5 the numerical value of this enhancement depends on the choice of precipitation parameterization and, to a lesser degree, the environmental conditions, but the computed magnitude of the effect is of the same order as the well-known effect of droplet number on cloud droplet size. This implies, unfortunately, that consideration of droplet number concentrations and more accurate representations of precipitation in marine boundary layer clouds will be required for predictions of oceanic cloud albedo in general circulation models.

Bibliography

Ackerman, A. S., O. B. Toon, and P. V. Hobbs, 1994: Reassessing the dependence of cloud condensation nucleus concentration on formation rate. *Nature*, **367**, 445–447.

Agee, E. M., 1984: Observations from space and thermal convection: A historical perspective. *Bull. Amer. Meteor. Soc.*, **65**, 938–949.

Agee, E. M., 1987: Mesoscale cellular convection over the oceans. *Dyn. Atmos. Oceans*, **10**, 317–341.

Albrecht, B., D. A. Randall, and S. Nicholls, 1988: Observations of marine stratocumulus during FIRE. *Bull. Amer. Meteor. Soc.*, **69**, 618–626.

Albrecht, B. A., 1984: A model study of downstream variations of the thermodynamic structure of the trade winds. *Tellus*, **36A**, 187–202.

Albrecht, B. A., 1989: Aerosols, cloud microphysics, and fractional cloudiness. *Science*, **245**, 1227–1230.

Albrecht, B. A., 1993: Effects of precipitation on the thermodynamic structure of the trade wind boundary layer. *J. Geophys. Res.*, **98**, 7327–7337.

Albrecht, B. A., A. K. Betts, W. H. Schubert, and S. K. Cox, 1979: A model of the thermodynamic structure of the trade-wind boundary layer. Part II: Applications. *J. Atmos. Sci.*, **36**, 90–98.

Albrecht, B. A., C. S. Bretherton, D. Johnson, W. H. Schubert, and A. S. Frisch, 1994: The Atlantic stratoucumulus transition experiment—ASTEX. *Bull. Amer. Meteor. Soc.*, submitted.

Austin, P., S. T. Siems, and Y. Wang, 1994a: Constraints on droplet growth in radiatively cooled stratocumulus clouds. *J. Atmos. Sci.*, submitted.

Austin, P., Y. Wang, R. Pincus, and V. Kujala, 1994b: Precipitation in stratocumulus clouds: observational and modelling results. *J. Atmos. Sci.*, to appear.

Baker, M. B., 1993: Variability in concentrations of cloud condensation nuclei in the marine cloud-topped boundary layer. *Tellus*, **45B**, 458–472.

Barkstrom, B. R., 1984: The earth radiation budget experiment (ERBE). *Bull. Amer. Meteor. Soc.*, **65**, 1170–1185.

Betts, A. K., 1990: Diurnal variation of California coastal stratocumulus from two days of boundary layer soundings. *Tellus*, **42A**, 302–304.

Betts, A. K., and R. Boers, 1990: A cloudiness transition in a marine boundary layer. *J. Atmos. Sci.*, **47**, 1480–1497.

Betts, A. K., P. Minnis, W. Ridgway, and D. F. Young, 1992: Integration of satellite and surface data using a radiative-convective oceanic boundary-layer model. *J. Appl. Met.*, **31**, 340–350.

Boers, R., and R. M. Mitchell, 1994: Absorption feedback in stratocumulus clouds: influence on cloud top albedo. *Tellus*, **46A**, 229–241.

Bougeault, P., 1985: The diurnal cycle of the marine stratocumulus layer: a higher-order model study. *J. Atmos. Sci.*, **42**, 2826–2843.

Brest, C. L., and W. B. Rossow, 1992: Radiometric calibration and monitoring of NOAA AVHRR data for ISCCP. *Int. J. Remote Sens.*, **13**, 235–273.

Bretherton, C. S., 1992: A conceptual model of the stratocumulus-trade-cumulus transition in the subtropical oceans. *Proceedings, 11th International Conference on Clouds and Precipitation,* Montreal, Canada, 374–377.

Bretherton, C. S., 1994: A turbulence closure model of marine stratocumulus clouds. Part I. The diurnal cycle of marine stratocumulus during FIRE 1987. *J. Atmos. Sci.*, to be revised.

Bretherton, C. S., and R. Pincus, 1994: Cloudiness and marine boundary layer dynamics in the ASTEX Lagrangian experiments. Part I: Synoptic setting and vertical structure. *J. Atmos. Sci.*, accepted.

Brost, R. A., D. L. Lenschow, and J. C. Wyngaard, 1982: Marine stratocumulus layers. Part I. Mean conditions. *J. Atmos. Sci.*, **39**,

Cahalan, R. F., W. Ridgeway, W. J. Wiscombe, T. L. Bell, and W. B. Snider, 1994: The albedo of fractal stratocumulus clouds. *J. Atmos. Sci.*, **51**, 2434–2455.

Cess, R. D., G. L. Potter, J. P. Blanchet, G. J. Boer, S. J. Ghan, J. T. Kiehl, T. H. Le, X. Z. Li, X. Z. Liang, J. F. B. Mitchell, J. J. Morcrette, D. A. Randall, M. R. Riches, E. Roeckner, U. Schlese, A. Slingo, K. E. Taylor, W. M. Washington, R. T. Wetherald, and I. Yagai, 1989: Interpretation of cloud-climate feedback as produced by 14 atmospheric general circulation models. *Science*, **245**, 513–516.

Cess, R. D., G. L. Potter, J. P. Blanchet, G. J. Boer, G. A. D. Del, M. Deque, V. Dymnikov, V. Galin, W. L. Gates, S. J. Ghan, J. T. Kiehl, A. A. Lacis, T. H. Le, Z. X. Li, X. Z. Liang, B. J. McAvaney, V. P. Meleshko, J. F. B. Mitchell, J. J. Morcrette, D. A. Randall, L. Rikus, E. Roeckner, J. F. Royer, U. Schlese, D. A. Sheinin, A. Slingo, A. P. Sokolov, K. E. Taylor, W. M. Washington, R. T. Wetherald, I. Yagai, and M. H. Zhange, 1990: Intercomparison and interpretation of climate feedback processes in 19 atmospheric general circulation models. *J. Geophys. Res.*, **95**, 16001–16015.

Charlson, R. J., J. E. Lovelock, M. O. Andreae, and S. G. Warren, 1987: Oceanic phytoplankton, atmospheric sulpher, cloud albedo and climate. *Nature*, **326**, 655–661.

Charlson, R. J., S. E. Schwartz, J. M. Hales, R. D. Cess, J. A. Coakley, Jr, J. E. Hansen, and D. J. Hofmann, 1992: Climate forcing by anthropogenic aerosols. *Science*, **255**, 423–430.

Chen, C., and W. R. Cotton, 1987: The physics of the marine stratocumulus-capped mixed layer. *J. Atmos. Sci.*, **44**, 2951–2977.

Coakley, J. A., Jr., R. L. Bernstein, and P. A. Durkee, 1987: Effect of ship-stack effluents on cloud reflectivity. *Science*, **237**, 1020–1022.

Coakley, J. A., Jr., and F. P. Bretherton, 1982: Cloud cover from high-resolution scanner data: detecting and allowing for partially filled fields of view. *J. Geophys. Res.*, **87**, 4917–4932.

Conover, J. H., 1966: Anomolous cloud lines. *J. Atmos. Sci.*, **23**, 778–785.

Davies, R., 1984: Reflected solar radiance measurements from broken cloud scenes and the interpretation of scanner measurements. *J. Geophys. Res.*, **89**, 1259–1266.

Dean, K. R., and G. G. Campbell, 1988. *CSU SPC format specification for FIRE AAA data collection.* Available from CIRA/CSU, Fort Collins, CO 80523.

Deardorff, J. W., 1980: Cloud top entrainment instability. *J. Atmos. Sci.*, **37**, 131–147.

Desormeaux, Y., W. B. Rossow, C. L. Brest, and C. G. Garrett, 1993: Normalization and calibration of geostationary satellite radiances for the International Satellite Cloud Climatology Project. *J. Atmos. Ocean. Tech.*, **10**, 304–325.

Diermendjian, D., 1969: *Electromagnetic Scattering on Spherical Polydispersions*. American Elsevier, New York, 290 pp.

DiMego, G. J., 1988: The National Meteorological Center regional analysis system. *Mon. Wea. Rev.*, **116**, 977–1000.

Fravalo, C., Y. Fouquart, and R. Rosset, 1981: The sensitivity of a model of low stratiform clouds to radiation. *J. Atmos. Sci.*, **38**, 1049–1062.

Hale, G. M., and M. R. Querry, 1973: Optical constants of water in the 200-nm to 200-µm wavelength region. *Appl. Opt.*, **12**, 555–563.

Han, Q., W. B. Rossow, and A. A. Lacis, 1994: Near-global survey of effective droplet radii in liquid water clouds using ISCCP data. *J. Climate*, **7**, 465–497.

Hansen, J. E., and L. D. Travis, 1974: Light scattering in planetary atmospheres. *Space Sci. Rev.*, **16**, 527–610.

Hartmann, D. L., 1993: Radiative Effects of Cloud on Earth's Climate. In *Aerosol-Cloud-Climate Interactions*. P. V. Hobbs (Ed.), Academic Press, 233.

Hignett, P., 1991: Observations of diurnal variation in a cloud-capped marine boundary layer. *J. Atmos. Sci.*, **48**, 1474–1482.

Kahl, J. D., and P. J. Samson, 1986: Uncertainty in trajectory calculations due to low resolution meteorological data. *J. Climate Appl. Meteor.*, **25**, 1816–1831.

King, M. D., 1987: Determination of the scaled optical thickness of clouds from reflected solar radiation measurements. *J. Atmos. Sci.*, **44**, 1734–1751.

Klein, S. A., and D. L. Hartmann, 1993: The seasonal cycle of low stratiform clouds. *J. Climate*, **6**, 1587–1606.

Klein, S. A., D. L. Hartmann, and J. R. Norris, 1994: On the relationships among low cloud structure, sea surface temperature, and atmospheric circulation in the summertime northeast Pacific. *J. Climate*, accepted.

Kloesel, K. A., 1992: Marine stratocumulus cloud clearing episodes observed during FIRE. *Mon. Wea. Rev.*, **120**, 565–578.

Kloesel, K. A., B. A. Albrecht, and D. P. Wylie, 1988: *FIRE marine stratocumulus observations—summary of operations and synoptic conditions*. FIRE Technical Report 1, The Pennsylvania State University, Department of Meteorology, University Park, PA.

Kneizys, F. X., E. P. Shettle, L. W. Abreu, J. H. Chetwynd Jr., G. P. Anderson, W. O. Gallery, J. E. A. Selby, and S. A. Clough, 1988: *User's Guide to LOWTRAN 7*. AFGL-TR-88-0177, Air Force Geophysics Laboratory, Hanscom Air Force Base, MA.

Kobayashi, T., 1988: Parameterization of reflectivity for broken cloud fields. *J. Atmos. Sci.*, **45**, 3034–3045.

Kobayashi, T., 1989: Radiative properties of finite cloud fields over a reflecting surface. *J. Atmos. Sci.*, **46**, 2208–2214.

Kobayashi, T., 1993: Effects due to cloud geometry on biases in the albedo derived from radiance measurements. *J. Climate*, **6**, 120–128.

Korolev, A. V., and I. P. Mazin, 1993: Zones of increased and decreased droplet concentration in stratiform clouds. *J. Appl. Met.*, **32**, 760–773.

Kriebel, K. T., R. W. Saunders, and G. Gesell, 1989: Optical properties of clouds derived from fully cloudy AVHRR pixels. *Contrib. Atmos. Phys.*, **62**, 165–171.

Kuo, H.-C., and W. H. Schubert, 1988: Stability of cloud-topped boundary layers. *Quart. J. Roy. Met. Soc.*, **114**, 887–916.

Lilly, D. K., 1968: Models of cloud-topped boundary layers under a strong inversion. *Quart. J. Roy. Met. Soc.*, **94**, 292–309.

McClain, E. P., W. G. Pichel, and C. C. Walton, 1985: Comparative performance of AVHRR multichannel sea surface temperatures. *J. Geophys. Res.*, **90**, 11587–11601.

McKee, T. B., and S. K. Cox, 1974: Scattering of visible radiation by finite clouds. *J. Atmos. Sci.*, **31**, 1885–1892.

Meador, W. E., and W. R. Weaver, 1980: Two-stream approximations to radiative transfer in planetary atmospheres: a unified description of exisiting methods and a new improvement. *J. Atmos. Sci.*, **37**, 630–643.

Minnis, P., and E. F. Harrison, 1984: Diurnal variability of regional cloud and clear-sky radiative parameters. Part I: Analysis method. *J. Climate Appl. Meteor.*, **23**, 993–1011.

Minnis, P., P. W. Heck, D. F. Young, C. W. Fairall, and J. B. Snider, 1992: Stratocumulus cloud properties derived from simultaneous satellite and island-based measurements during FIRE. *J. Appl. Met.*, **31**, 317–339.

Moeng, C. H., S. Shen, and D. A. Randall, 1992: Physical processes within the nocturnal stratus-topped boundary layer. *J. Atmos. Sci.*, **49**, 2384–2401.

Nakajima, T., and M. D. King, 1990: Determination of the optical thickness and effective particle radius of clouds from reflected solar radiation measurements. I. Theory. *J. Atmos. Sci.*, **47**, 1878–1893.

Nakajima, T., M. D. King, J. D. Spinhirne, and L. F. Radke, 1991: Determination of the optical thickness and effective particle radius of clouds from reflected solar radiation measurements. II. Marine stratocumulus observations. *J. Atmos. Sci.*, **48**, 728–750.

Nicholls, S., 1984: The dynamics of stratocumulus: aircraft observations and comparisons with a mixed layer model. *Quart. J. Roy. Met. Soc.*, **110**, 783–820.

Nicholls, S., 1987: A model of drizzle growth in warm, turbulent, stratiform clouds. *Quart. J. Roy. Met. Soc.*, **113**, 1141–1170.

Nicholls, S., and J. Leighton, 1986: An observational study of the structure of stratiform cloud sheets: Part I. Structure. *Quart. J. Roy. Met. Soc.*, **112**, 431–460.

Paltridge, G. W., and C. M. R. Platt, 1976: *Radiative Processes in Meteorology and Climatology*. Elsevier Scientific Pub. Co., Amsterdam, 318 pp.

Paluch, I. R., and D. H. Lenschow, 1991: Stratiform cloud formation in the marine boundary layer. *J. Atmos. Sci.*, **48**, 2141–2158.

Penner, J. E., R. J. Charlson, J. M. Hales, N. Laulainen, R. Leifer, T. Novakov, J. Ogren, L. F. Radke, S. E. Schwartz, and L. Travis, 1993: *Quantifying and minimizing uncertainty of climate forcing by anthropogenic aerosols*. DOE/NBB-0092T UC-402, U. S. Department of Energy.

Petty, G., W., 1994: Physical retrievals of over-ocean rain rate from multichannel microwave imagery. Part I: Theoretical characteristics of normalized polarization and scattering indices. *Met. and Atmos. Phys.*, in press.

Pincus, R., and M. B. Baker, 1994: Effect of precipitation on the albedo of clouds in the marine boundary layer. *Nature*, **372**, 205–252.

Pincus, R., M. B. Baker, and C. S. Bretherton, 1990: Lagrangian studies of marine stratocumulus evolution. *Proceedings, 1990 Conference on Cloud Physics,* Amer. Meteor Soc., San Francisco, CA, J8–J14.

Pincus, R. M., M. B. Baker, and C. S. Bretherton, 1992: Lagrangian observations of marine stratocumulus evolution and breakup. *Proceedings, 11th International Conference on Clouds and Precipitation,* Montreal, Canada.

Pincus, R., M. Szczodrak, J. Gu, and P. Austin, 1994: Uncertainty in cloud optical depth estimates made from satellite radiance measurements. *J. Climate*, to be revised.

Platnick, S., and S. Twomey, 1994: Determining the susceptibility of cloud albedo to changes in droplet concentrations with the Advanced Very High Resolution Radiometer. *J. Appl. Met.*, **33**, 334–347.

Press, W. H., B. P. Flannery, S. A. Teukolsky, and W. T. Vetterling, 1986: *Numerical Recipes: The Art of Scientific Computing*. First Edition, Cambridge University Press, Cambridge, 818 pp.

Radke, L. F., J. A. Coakley Jr, and M. D. King, 1989: Direct and remote sensing observations of the effects of ships on clouds. *Science*, **246**, 1146–1149.

Randall, D. A., 1980: Conditional instability of the first kind upside down. *J. Atmos. Sci.*, **37**, 125–130.

Roach, W. T., 1976: On the effect of radiative exchange on the growth by condensation of a cloud or fog droplet. *Quart. J. Roy. Met. Soc.*, **102**, 361–372.

Rogers, D. P., and D. Koracin, 1992: Radiative transfer and turbulence in the cloud-topped marine atmospheric boundary layer. *J. Atmos. Sci.*, **49**, 1473–1486.

Rossow, W. B., 1989: Measuring cloud properties from space: a review. *J. Climate*, **2**, 201–213.

Rossow, W. B., and R. A. Schiffer, 1991: ISCCP cloud data products. *Bull. Amer. Meteor. Soc.*, **72**, 2–20.

Rossow, W. B., L. C. Garder, and A. A. Lacis, 1989: Global, seasonal cloud variations from satellite radiance measurements. I. Sensitivity of analysis. *J. Climate*, **2**, 419–458.

Rossow, W. B., L. C. Garder, P. J. Lu, and A. W. Walker, 1991: *International Satellite Cloud Climatology Project (ISCCP) Documentation of Cloud Data*. WMO/TD No. 266 (Revised), World Meteorological Organization, Geneva.

Rossow, W. B., Y. Desormeaux, C. L. Brest, and A. W. Walker, 1992: *International Satellite Cloud Climatology Project (ISCCP) Radiance Calibration Report*. WMO/TD No. 520, World Climate Research Program, Geneva.

Rossow, W. B., F. Mosher, E. Kinsella, A. Arking, M. Desbois, E. Harrision, P. Minnis, E. Ruprecht, G. Seze, C. Simmer, and E. Smith, 1985: ISCCP cloud algorithm intercomparison. *J. Climate Appl. Meteor.*, **24**, 877–903.

Rozendaal, M. A., C. B. Leovy, and S. A. Klein, 1994: An observational study of diurnal variations of marine stratiform cloud. *J. Climate*, to be revised.

Saunders, R. W., and D. P. Edwards, 1989: Atmospheric transmittances for the AVHRR channels. *Appl. Opt.*, **28**, 4154–4160.

Schubert, W. H., J. S. Wakefield, E. J. Steiner, and S. K. Cox, 1979a: Marine stratocumulus convection. Part I: Governing equations and horizontally homogeneous solutions. *J. Atmos. Sci.*, **36**, 1286–1307.

Schubert, W. H., J. S. Wakefield, E. J. Steiner, and S. K. Cox, 1979b: Marine stratocumulus convection. Part II: Horizontally inhomogeneous solutions. *J. Atmos. Sci.*, **36**, 1309–1324.

Schubert, W. E., P. E. Ciesielski, T. B. McKee, J. D. Kleist, S. K. Cox, C. M. Johnson-Pasqua, and W. L. Smith Jr, 1987: *Analysis of boundary layer sounding data from the FIRE marine stratocumulus project*. Atmopsheric Sciences Paper No. 419, Colorado State University, Fort Collins, CO.

Siems, S. T., and C. S. Bretherton, 1992: A numerical investigation of cloud-top entrainment instability and related experiments. *Quart. J. Roy. Met. Soc.*, **118**, 787–818.

Siems, S. T., D. H. Lenschow, and C. S. Bretherton, 1993: A numerical study of the interaction between stratocumulus and the air overlying it. *J. Atmos. Sci.*, **50**, 3663–3676.

Siems, S. T., C. S. Bretherton, M. B. Baker, S. Shy, and R. E. Breidenthal, 1990: Buoyancy reversal and cloud-top entrainment instability. *Quart. J. Roy. Met. Soc.*, **116**, 705–739.

Slingo, A., 1989: A GCM parameterization for the shortwave radiative properties of water clouds. *J. Atmos. Sci.*, **46**, 1419–1427.

Stamnes, K., S.-C. Tsay, W. J. Wiscombe, and K. Jayaweera, 1988: A numerically stable algorithm for discrete-ordinate-method radiative transfer in multiple scattering and emitting layers. *Appl. Opt.*, **27**, 2502–2512.

Stephens, G. L., 1978: Radiation profiles in extended water clouds. II: Parameterization schemes. *J. Atmos. Sci.*, **35**, 2123–2132.

Suttles, J. T., R. N. Green, P. Minnis, G. L. Smith, W. F. Staylor, B. A. Wielicki, I. J. Walker, D. F. Young, V. R. Taylor, and L. L. Stowe, 1988: *Angular radiation models for the earth-atmosphere system. Vol I: Shortwave radiation*. NASA Ref. Publ. RP-1184, Washington, DC.

Taylor, J. P., and A. McHaffie, 1994: Measurements of cloud susceptibility. *J. Atmos. Sci.*, **51**, 1298–1306.

Taylor, V. R., and L. L. Stowe, 1984: Reflectance characteristics of uniform earth and cloud surfaces derived from NIMBUS 7 ERB. *J. Geophys. Res.*, **89**, 4987–4996.

Tsay, S.-C., K. Stamnes, and K. Jayaweera, 1989: Radiative energy budget in the cloudy and hazy Arctic. *J. Atmos. Sci.*, **46**, 1002–1018.

Turton, J. D., and S. Nicholls, 1987: A study of the diurnal variation of stratocumulus using a multiple mixed layer model. *Quart. J. Roy. Met. Soc.*, **113**, 969–1009.

Twomey, S., 1977a: *Atmospheric aerosols*. Elsevier, Amsterdam, 302 pp.

Twomey, S., 1977b: The influence of pollution on the shortwave albedo of clouds. *J. Atmos. Sci.*, **34**, 1149–1152.

Twomey, S., 1991: Aerosols, clouds, and radiation. *Atmos. Env.*, **25A**, 2435–2442.

Twomey, S., and J. Warner, 1967: Comparison of measurements of cloud droplets and cloud nuclei. *J. Atmos. Sci.*, **24**, 702–703.

van de Hulst, H. C., 1957: *Light scattering by small particles*. John Wiley & Sons, New York, 470 pp.

Wang, S., B. A. Albrecht, and P. Minnis, 1993: A regional simulation of marine boundary-layer clouds. *J. Atmos. Sci.*, **50**, 4022–4040.

Warren, S. G., C. J. Hahn, J. London, R. M. Chervin, and R. L. Jenne, 1986: *Global Distribution of Total Cloud Cover and Cloud Type Amounts Over Land*. NCAR Technical Note NCAR/TN-317+STR, National Center for Atmospheric Research, Boulder, CO.

Warren, S. G., C. J. Hahn, J. London, R. M. Chervin, and R. L. Jenne, 1988: *Global Distribution of Total Cloud Cover and Cloud Type Amounts Over Ocean*. NCAR Technical Note NCAR/TN-317+STR, National Center for Atmospheric Research, Boulder, CO.

Weaver, C. J., and R. Pearson Jr., 1990: Entrainment instability and vertical motion as causes of stratocumulus breakup. *Quart. J. Roy. Met. Soc.*, **116**, 1359–1388.

Wetzel, M. A., and T. H. Vonder Haar, 1991: Theoretical development and sensitivity tests of a stratus cloud droplet size retrieval method for AVHRR-K/L/M. *Remote Sens. Environ.*, **36**, 105–119.

Wielicki, B. A., and L. Parker, 1992: On the determination of cloud cover from satellite sensors: the effect of sensor spatial resolution. *J. Geophys. Res.*, **97**, 12799–12823.

Wiscombe, W. J., 1979: *Mie Scattering Calculations—Advances in Technique and Fast Vector Speed Computer Codes*. NCAR Tech Note TN-140+Str, National Center for Atmospheric Research, Boulder, Colorado.

Wiscombe, W. J., 1980: Improved Mie scattering algorithms. *Appl. Opt.*, **19**, 1505–1509.

Woodruff, S. D., R. J. Slutz, R. L. Jenne, and P. M. Steurer, 1986: A comprehensive ocean-atmopshere data set. *Bull. Amer. Meteor. Soc.*, **68**, 1239–1250.

Wyant, M. C., and C. S. Bretherton, 1992: The dynamics of decoupling in a cloud-topped boundary layer. *Proceedings, 11th International Conference on Clouds and Precipitation,* Montreal, Canada, 417–420.

Appendix A: Cloud Optical Depth Retrieval

In this appendix I describe in greater detail the procedures underlying the optical depth retrieval algorithm outlined in §2.2.2. Optical depth is retrieved by comparing angularly resolved predictions of top-of-the-atmosphere visible wavelength radiance with observations of radiance made by satellite instruments. Accordingly, I describe here the several steps required in making the radiance predictions, the techniques for determining the viewing and illumination geometry for each pixel, and the simple scheme used to compare the predictions and observations. I implemented this retrieval scheme in collaboration with Malgorzata Szczodrak, Jiujing Gu, and Philip Austin of the University of British Columbia.

A.1 *Radiative Transfer Calculations*

The predictions of top-of-the-atmosphere radiance are made in two steps. First, single scattering parameters (the scattering phase function $P(\Theta)$ describing the angular distribution of scattered radiation, its Legendre polynomial expansion, and the single scattering albedo, which indicates the likelihood that a photon will be absorbed during a single encounter) are computed for the various atmospheric constituents. Secondly, a model atmosphere is constructed in which the amount and vertical distribution of scatterers and absorbers is specified. An angularly resolved radiative transfer model is then used to predict the radiance at the top of the model atmosphere.

A.1.1 SINGLE SCATTERING CALCULATIONS

Radiative processes in the cloudy atmosphere include scattering by cloud droplets and molecules (Rayleigh scattering), scattering and absorption by aerosols, and absorption by gasses. In the case of Rayleigh scattering, the scattering phase function can be computed directly and the single scattering albedo is one. For gaseous absorption the single scattering albedo is zero and the phase function irrelevant. Therefore, phase functions and single scattering albedos are required only for atmospheric aerosols and cloud droplets.

Single scattering parameters for droplets and aerosols (assumed spherical) may be computed using Mie theory (van de Hulst, 1957), which describes the disposition of a plane parallel electromagnetic wave impinging on a dielectric sphere. The scattering is characterized by

the size parameter $x = 2\pi r/\lambda$, where r is the droplet or aerosol radius and λ the wavelength of the radiation. Given the size parameter and the complex index of refraction of the sphere, Mie theory provides the extinction and scattering efficiencies Q_{ext} and Q_{sca} and the scattering phase function $P(\Theta)$. From these quantities one may derive the single scattering albedo

$$\tilde{\omega} = \frac{Q_{sca}}{Q_{ext}} \qquad \text{(A-1)}$$

and the moments P_l of the Legendre polynomial expansion of $P(\Theta)$.

The single scattering parameters for individual particles vary rapidly with size parameter x. Since collections of aerosols and cloud droplets typically show some amount of variability in size, the parameters used in the radiative transfer model must be integrated over a representative size distribution n(r). The scattering parameters for the collection are determined by the parameters ar each radius weighted by the fraction of particles at each radius, but since bigger particles intercept and scatter more light, the parameters must also be weighted by the cross-sectional area of each particle. In particular:

$$\tilde{\omega} = \frac{\int_0^\infty r^2 n(r) Q_{sca}\, dr}{\int_0^\infty r^2 n(r) Q_{ext}\, dr}$$

$$P(\Theta) = \frac{\int_0^\infty r^2 n(r)\,(S_1^2 + S_2^2)\, dr}{\int_0^\infty r^2 n(r) Q_{ext}\, dr}$$

$$P_l = \int_0^\infty n(r) P_l\, dr \qquad \text{(A-2)}$$

Hansen and Travis (1974) showed that the Mie properties of a collection of droplets depend primarily on the surface-area-weighted or effective radius of the distribution, which is defined in (1-2). The exact distribution used in the integration, therefore, is not particularly important.

The single scattering properties of the aerosols and cloud droplets used in the model atmosphere are determined from Mie theory using the subroutine of Wiscombe (1979, 1980). The cloud droplet number distribution is assumed to follow the Gamma distribution of Hansen and Travis (1974):

$$n(r) = K r^{(1-3b)/b} e^{-r/(ab)}$$

$$K = \frac{N\,(ab)^{(2b-1)}}{\Gamma([1-2b]/b)} \qquad \text{(A-3)}$$

where a is the effective radius and b the effective variance. The index of refraction for water at $\lambda = 0.65$ μm is taken from measurements by (Hale and Querry, 1973). The distribution constants are chosen as a = 10 μm, b = 0.05. Since only the relative magnitudes of the Legendre coefficients are required, the number concentration N is set to 1. The aerosols are modelled using the Haze-1 number concentration (Diermendjian, 1969):

$$n(r) = 4.9757 \times 10^{-6} r^2 e^{-15.118\sqrt{r}} \qquad \text{(A-4)}$$

using the index of refraction from Paltridge and Platt (1976), in which I assume a relative humidity of 70%. The limits of integration (zero and infinity) in (A-2) are replaced with limits r_{min} and r_{max} such that the cross-section $r^2 n(r)$ falls to 10^{-4} times its maximum value. Numerical values are given in Table A-1.

A.1.2 MULTIPLE SCATTERING CALCULATIONS

I use the discrete ordinates method (Stamnes et al., 1988) to compute the top-of-the-atmosphere radiance as seen be a satellite as a function of viewing and illumination geometry and

Table A-1: Single Scattering Integration Parameters

	Droplets	Aerosols
r_{min} (μm)	2.4	0.005
r_{max} (μm)	22.65	3.1625
index of refraction	$1.331 + 1.64 \times 10^{-6}\, i$	$1.4375 + 0.00698\, i$

cloud optical depth. The discrete ordinates method is a generalization of the two-stream method in which the single scattering phase function $P(\Theta)$ is expanded in a series of M Legendre polynomials, and the radiance expanded as a product of Legendre polynomials and Fourier series. The radiative transfer equation then splits up into M+1 independent equations which can be solved using standard linear algebra techniques (Hansen and Travis, 1974).

The ISCCP sensor calibrations for polar orbiting (Brest and Rossow, 1992) and geostationary (Desormeaux et al., 1993) sensors use as their reference instrument the Advanced Very High Resolution Radiometer (AVHRR) sensor aboard NOAA-7. Therefore, the radiative transfer model is used to predict the TOA radiance seen by this sensor. The radiative transfer model results may be used without modification to interpret radiance measurements from any satellite in the ISCCP program.

I construct a model atmosphere represented as three plane parallel, horizontally homogeneous layers overlying an ocean surface, with cloud occupying the middle layer. The ocean surface reflects isotropically at all wavelengths with an albedo dependent on solar zenith angle (Minnis et al., 1992):

$$\alpha = \frac{2.8}{\mu_0^{1.7} + 0.065} + 15\,(\mu_0 - 0.1)\,(\mu_0 - 0.5)\,(\mu_0 - 1) \qquad \text{(A-5)}$$

The upper and lower layers of the atmosphere contain aerosols, absorbing gases and molecules which cause Rayleigh scattering. The middle layer contains these constituents in addition to the cloud droplets.

The spectral response of the standard AVHRR instrument spans the spectral range 0.50 – 0.80 μm. The transmittance of each atmospheric layer in this range in the absence of clouds is computed using LOWTRAN-7 (Kneizys et al., 1988), assuming a standard mid-latitude summer atmosphere and the Navy standard marine aerosol model. LOWTRAN separately calculates the transmittance due to each radiatively active constituent in the atmosphere at 5 cm^{-1} intervals. In the spectral region in which the AVHRR sensor is sensitive, the only significantly absorbing gas is ozone (Saunders and Edwards, 1989). The LOWTRAN results are therefore averaged into 8 bands across which ozone transmittance is smooth, and the atmospheric transmittance for each constituent is inverted to find the ozone gaseous absorption, aerosol, and Rayleigh scattering optical depth in each spectral band and each layer of the model atmosphere.

The optical properties of each atmospheric layer in each spectral band can be determined by summing over the contributions from each constituent (Tsay et al., 1989):

$$\tau = \sum_i \tau_i$$

$$\omega_0 = \frac{\sum_i \omega_i \tau_i}{\tau}$$

$$P(\Theta) = \frac{\sum_i \omega_i \tau_i P_i(\Theta)}{\sum_i \omega_i \tau_i}$$

$$P_l = \frac{\sum_i \omega_i \tau_i P_{l,i}}{\sum_i \omega_i \tau_i} \qquad \text{(A-6)}$$

where τ_i, ω_i, P_i and $P_{l,i}$ are optical depth, single scattering albedo, scattering phase function and l^{th} Legendre moments of the i^{th} atmospheric constituent. I use the program of Stamnes et al. (1988) to compute the TOA radiance $L_i(\mu_0, \mu, \phi, \tau)$ in each spectral band at the top of the model atmosphere. Radiance is a function of solar zenith angle μ_0, satellite zenith angle μ, the azimuthal separation between the satellite and the sun ϕ, and cloud optical depth τ, and computations are made at 48 values of ϕ, 24 values of μ, and 20 values of μ_0, evenly spaced in the ranges {0, 180°}, {0, 1}, and {0, 1} respectively, and for τ = {1, 2, 4, 6, 8, 10, 12, 14, 16, 18, 20, 24, 28, 32, 36, 40, 48, 56, 64, 80, 96, 112, 128}. The total TOA scaled radiance L^* used by the calibration algorithms is obtained by summing over each of the j spectral intervals, weighting by the incident solar radiance $S_0(\lambda)$ and the instrument response $I(\lambda)$ (Rossow et al., 1992), and dividing by the instrument-weighted solar constant:

$$L^*(\mu_0, \mu, \phi, \tau) = \frac{\pi}{E_0} \sum_j S_0(j) I(j) L_j(\mu_0, \mu, \phi, \tau) \qquad \text{(A-7)}$$

In practice, the results of the computations described by (A-7) are stored in a four-dimensional look-up table.

A.2 *Viewing and Illumination Geometry*

In order to compare the predictions of TOA radiance with a satellite observation for a single pixel, the values of the viewing and illumination angles μ_0, μ, and ϕ must be computed. The sub-satellite latitude and longitude θ_{sat} and ϕ_{sat} must, in general, be computed from orbital parameters, but geostationary satellites remain at fixed longitudes over the equator. Sub-solar latitude and longitude on Julian day d at fractional hour h can be found from:

$$\theta_{sun} = 0.409 \cos\left(\frac{2\pi d}{365.25}\right)$$

$$\phi_{sun} = \frac{\pi h}{12} \qquad \text{(A-8)}$$

Trigonometric relations on the surface of a sphere then determine the zenith angle Θ_{sun} and the azimuth Φ_{sun} between the sub-solar point and the pixel latitude and longitude θ and ϕ:

$$\cos\Theta_{sun} = \sin\theta_{sun}\sin\theta + \cos\theta_{sun}\cos\theta\cos\phi_{sun} - \phi$$

$$\cos\Phi_{sun} = \frac{\sin\theta_{sun} - \sin\theta\cos\Theta_{sun}}{\sin\Theta_{sun}\cos\theta} \qquad \text{(A-9)}$$

so that the cosine of the solar zenith angle can be calculated from

$$\tan\mu_0 = \frac{\sin\Theta_{sun}}{\cos\Theta_{sun}} \qquad \text{(A-10)}$$

A similar set of relations holds for the cosine of the satellite zenith angle. The relative azimuth between the sun and the satellite is the difference of the azimuths:

$$\phi = \left|\Phi_{sun} - \Phi_{sat}\right| \qquad \text{(A-11)}$$

A.3 *Table Look Up*

In practice, cloud optical depth is retrieved only after the satellite images have been calibrated and each pixel identified as clear or cloudy. Satellite brightness levels for each pixel are converted to a scaled radiance value L_{obs} using the ISCCP calibration algorithms (Desormeaux et al., 1993). Each pixel in the image is classified as clear or cloudy using the reflectance threshold described in §2.2.1. For each cloudy pixel I compute the viewing and illumination geometry from the time of the image and the pixel's ground position using the equations in §A.2. Once the angles are known, the radiance predictions in (A-7) depend only on the cloud optical depth. I use a root-finding algorithm based on the routine ZBRENT of Press et al. (1986) to solve the equation $L_{obs} = L^*(\mu_0, \mu, \phi; \tau)$ by varying τ. Values of L^* at arbitrary values of optical depth and viewing and illumination geometry are obtained by linearly interpolating along the look-up tables.

Biography

Robert Pincus was born on 26 February 1962 in San Francisco, California. His favorite color combination is steel blue and maroon, and his favorite winter vegetable is Brussel Sprouts, although it might also be kale.

The best thing that ever happened to him is meeting Cristina Herdman. They were married on 13 April 1991, and live in Seattle, Washington, with their cat Loki.